Multiple-Reflection Time-of-Flight Mass Spectrometer (MR-ToF MS) enhanced in-gas-jet Laser Spectroscopy of the Heavy Actinides

Dissertation

zur Erlangung des Grades
"Doktor der Naturwissenschaften"
im Promotionsfach Chemie

am Fachbereich Chemie, Pharmazie,
Geographie und Geowissenschaften
der Johannes Gutenberg-Universität Mainz

Danny Münzberg
geboren in Münster

Mainz, October 14, 2025

1. Gutachter: [redacted]
2. Gutachter: [redacted]

Tag der mündlichen Prüfung: 01.12.2025

Die vorliegende Arbeit wurde in der Zeit vom März 2021 bis Oktober 2025 im Helmholtz-Institut Mainz unter der Anleitung von [redacted] angefertigt.

Ich versichere, dass ich diese Arbeit eigenständig verfasst und keine anderen als die angegebenen Hilfsmittel (Literatur, Apparaturen, Materialien) verwendet sowie Zitate kenntlich gemacht habe.

Ort, Datum	Danny Münzberg

"The inner machinations of my mind are an enigma"
-Patrick Star

Abstract

Laser spectroscopy is a versatile tool to study the atomic structure and properties of exotic nuclei with high efficiency and sensitivity. Electronic states of atoms can be excited via illumination with monochromatic, resonant laser light. In this work, the identification of excited atoms is done by either observation of their fluorescence emitted when relaxing back to an energetically lower state (light induced fluorescence, **LIF**), or by ionization of the atom via multi-step excitation (resonant ionization spectroscopy, **RIS**). This thesis presents some recent developments and applications of the JetRIS setup, a setup designed for laser spectroscopy in a gas jet. Within the context of this work, laser spectroscopy was utilized to characterize its spectral resolution, an atomic transition of ^{254}No, multiple resonances of $^{\mathrm{nat}}$Sm, hyperfine components and isotope shifts and to test multiple technical developments necessary for studying on-line produced nuclides with the JetRIS setup.
A crucial part of the JetRIS setup is the nozzle and the corresponding gas jet formation. Here, the performance in terms of spectral linewidth was characterized utilizing LIF via laser excitation of Dy I using a $4f^{10}6s^2 \rightarrow 4f^{10}6s6p$ transition at $\lambda = 404.5\,\mathrm{nm}$. The spatially resolved fluorescence in dependence of the laser excitation frequency was recorded and a maximum average resolution of $\Delta\nu = 212(30)\,\mathrm{MHz}$ was obtained. JetRIS was then used in on-line experiments at the GSI facility in Darmstadt, utilizing two-step RIS and α-decay based detection measuring the $^1\mathrm{S}_0 \rightarrow {}^1\mathrm{P}_1$ transition of ^{254}No. The centroid of the transition was determined with $\nu = 29\,961.480(12)\,\mathrm{cm}^{-1}$ while a resolution of $\Delta\nu = 770(300)\,\mathrm{MHz}$ was achieved.
The last part of the thesis is dedicated towards RIS of samarium using ToF based detection utilizing and characterizing a Multiple-Reflection Time-of-Flight Mass Spectrometer (MR-ToF MS). Here six different First Excitation Step (FES) transitions were characterized, determining their mass and field shifts, as well as the hyperfine parameter $\mathcal{A}$ for the isotopes ^{147}Sm and ^{149}Sm. For five FES transitions, two Auto-Ionizing (AI) transitions were identified each, while for the remaining FES transition, only one AI transition was found. Utilizing the isotope ^{154}Sm, the mass resolving power R, the relative efficiency ϵ and the capability of in-trap-deflection of the MR-ToF MS was characterized. The MR-ToF MS will be integrated into the JetRIS setup, to enhance its detection capabilities for future on-line studies using a linear Paul trap as a radiofrequency (RF) cooler buncher. The cooler buncher and merging of both setups are planned for future work.

Zusammenfassung

Die Laserspektroskopie ist ein vielseitiges Werkzeug, um die atomare Struktur und Eigenschaften exotischer Kerne mit hoher Effizienz und Empfindlichkeit zu untersuchen. Elektronische Zustände von Atomen können durch Bestrahlung mit monochromatischem, resonantem Laserlicht angeregt werden. In dieser Arbeit erfolgt die Identifizierung angeregter Atome entweder durch Beobachtung ihrer Fluoreszenz, die beim Zurückfallen in einen energetisch niedrigeren Zustand emittiert wird (lichtinduzierte Fluoreszenz, **LIF**), oder durch Ionisierung des Atoms mittels mehrstufiger Anregung (resonante Ionisationsspektroskopie, **RIS**). Diese Arbeit stellt einige Neuerungen und Anwendungen des JetRIS vor, eines Versuchsaufbaus, welcher für die Laserspektroskopie in einem Gasstrahl entwickelt wurde. Im Rahmen dieser Arbeit wurde die Laserspektroskopie genutzt, um seine spektrale Auflösung, einen atomaren Übergang von ^{254}No, mehrere Resonanzen von $^{\mathrm{nat}}$Sm, Hyperfeinkomponenten und Isotopieverschiebungen zu charakterisieren und mehrere technische Entwicklungen zu testen, die für die Untersuchung von beschleunigerproduzierten Nukliden mit dem JetRIS-Aufbau erforderlich sind. Ein wesentlicher Bestandteil des JetRIS ist die Düse und die entsprechende Gasstrahlbildung. Hier wurde die Leistung in Bezug auf die spektrale Linienbreite unter Verwendung von LIF durch Laseranregung von Dy I eines $4f^{10}6s^2 \rightarrow 4f^{10}6s6p$ Übergangs bei $\lambda = 404.5\,\mathrm{nm}$ charakterisiert. Die räumlich aufgelöste Fluoreszenz wurde in Abhängigkeit der Laseranregungsfrequenz aufgezeichnet und eine maximale durchschnittliche Auflösung von $\Delta\nu = 212(30)\,\mathrm{MHz}$ erzielt. Anschließend wurde JetRIS in Beschleunigerexperimenten an der GSI in Darmstadt eingesetzt, um zweistufige RIS in Kombination mit α Zerfall Detektion verwendet wurde, um den Übergang von $^1\mathrm{S}_0 \rightarrow {}^1\mathrm{P}_1$ in ^{254}No zu messen. Der Schwerpunkt des Übergangs wurde mit $\nu = 29\,961.480(12)\,\mathrm{cm}^{-1}$ bestimmt, während eine Auflösung von $\Delta\nu = 770(300)\,\mathrm{MHz}$ erreicht wurde.
Der letzte Teil der Arbeit widmet sich der RIS von Samarium unter Verwendung einer ToF basierten Detektion unter Einsatz und Charakterisierung eines Mehrfachreflexionsflugzeitmassenspektrometers (MR-ToF MS). Hier wurden sechs verschiedene erste Anregunsschritte (FES) charakterisiert und ihre Masse- und Feldverschiebungen sowie der Hyperfeinparameter $\mathcal{A}$ für die Isotope ^{147}Sm und ^{149}Sm bestimmt. Bei fünf FES wurden jeweils zwei Autoionisationsübergänge (AI) identifiziert, während bei dem verbleibenden FES nur ein AI gefunden wurde. Mit Hilfe des Isotops ^{154}Sm wurden das

Massenauflösungsvermögen R, die relative Effizienz ϵ und die Fähigkeit zur in-trap-Ablenkung des MR-ToF-MS charakterisiert. Das MR-ToF MS wird in den JetRIS-Aufbau integriert, um dessen Detektionsfähigkeiten für zukünftige Experimente unter Verwendung einer linearen Paulfalle als Radiofrequenz (RF) cooler buncher zu verbessern. Der cooler buncher und die Kombinierung beider Aufbauten sind Teile zukünftiger Arbeiten.

List of included articles

This cumulative dissertation is based on three different publications [1, 2, 3]. These articles were chosen to represent the core aspects of this work. The author has made significant contribution to each of these articles, which are pointed out in detail in an introduction before each article shown in this thesis. A complete list of all publications of the author can be found in the Appendix.
Publication [1] describes the characterization of supersonic gas jets formed by de-Laval type nozzles in the JetRIS setup utilizing LIF in dysprosium. Publication [2] describes on-line two-step RIS measurements of ^{254}No using the JetRIS setup at the GSI facility.
Publication [3] shows ToF-assisted two-step RIS of $^{\text{nat}}$Sm for laser ionization scheme development and determination of the isotope shifts, as well as the hyperfine parameter $\mathcal{A}$ for the $I \neq 0$ isotopes. It furthermore shows a characterization of the mass resolving power and relative efficiency of the MR-ToF which shall be an addition to JetRIS.

References

[1] Danny Münzberg et al. "Resolution Characterizations of JetRIS in Mainz Using ^{164}Dy". In: *Atoms* 10.2 (2022), p. 57. DOI: 10.3390/atoms10020057.

[2] Jeremy Lantis et al. "In-gas-jet laser spectroscopy of ^{254}No with JetRIS". In: *Physical Review Research* 6.2 (2024). DOI: 10.1103/PhysRevResearch.6.023318.

[3] Danny Münzberg et al. "Multiple-reflection time-of-flight mass spectrometer assisted laser spectroscopy of $^{\text{nat}}$Sm". In: *Nuclear Instruments and Methods in Physics Research Section B: Beam Interactions with Materials and Atoms* 569 (2025), p. 165884. ISSN: 0168583X. DOI: 10.1016/j.nimb.2025.165884.

Contents

1 Introduction

The curious desire for an intricate understanding of fundamental properties and connections is one of the main driving factors of natural sciences. When searching for fundamental understanding, one might look to the smallest of things and study it intensively. One type of object whose behaviour is worth studying in this regard is the atom itself, with its properties determined by the electron shell, and its nucleus. Due to their often times connected behaviour, one can learn a lot by precisely studying the atomic shell and deriving properties of the nucleus from it. Due to relativistic effects, heavy elements ($Z \geq 100$) are hard to describe theoretically. Since they also have no natural abundance, studying their properties is quite a challenging task. In recent years, many experiments were conducted to shine light on these properties. One particularly interesting observable is the nuclear mean-square charge radii to identify nuclear shell gaps, like $N = 40$ [1], N=98 [2], Z= 60 [3] the combination of N=152 at Z=100 [4, 5] (c.f. Fig. 1) and N=162 at Z=110 [6]. Other interesting cases for research on nuclear structure are conducting experiments on nuclear isomers, like the ^{254}No $K^{\pi} = 8^{-}$ nuclear isomer whose structure could not be unambiguously determined via γ-ray spectroscopy [7] and is an interesting case for nuclear theory [8] and the study of nuclear deformation through, e.g. laser spectroscopy [9].
Early descriptions of atomic nuclei were based on the liquid drop model (LDM). Here the nucleus is described as a spherical, incompressible homogenous object comprised of protons and neutrons which are held together by the strong force [10]. Even though this model describes a quantum object via a macroscopic analogon, that of a water droplet, it holds quite well in terms of delivering a qualitative understanding of nuclei and some of their parameters like the binding energy per nucleon. This analogon approach works well due to the short-ranged nature of the strong force. One major limitation of this model is its inability to predict and explain effects that arise due to substructure inside the nucleus. One example of this are the so-called magic numbers. These are specific amounts of protons (2, 8, 20, 28, 50, 82) and/or neutrons (2, 8, 20, 28, 50, 82, 126) which exhibit a particularly high stability [11]. Due to this, the nuclear shell model (NSM) was developed [12, 13]. This model is an analogon to the model for atomic orbitals and describes nucleons in an atomic nucleus via discrete states for each nucleon. The existence of nuclear shell effects is essential for the existence of elements with $Z \geq 104$ [14, 15], for which the LDM predicts a fission barrier so small that they be-

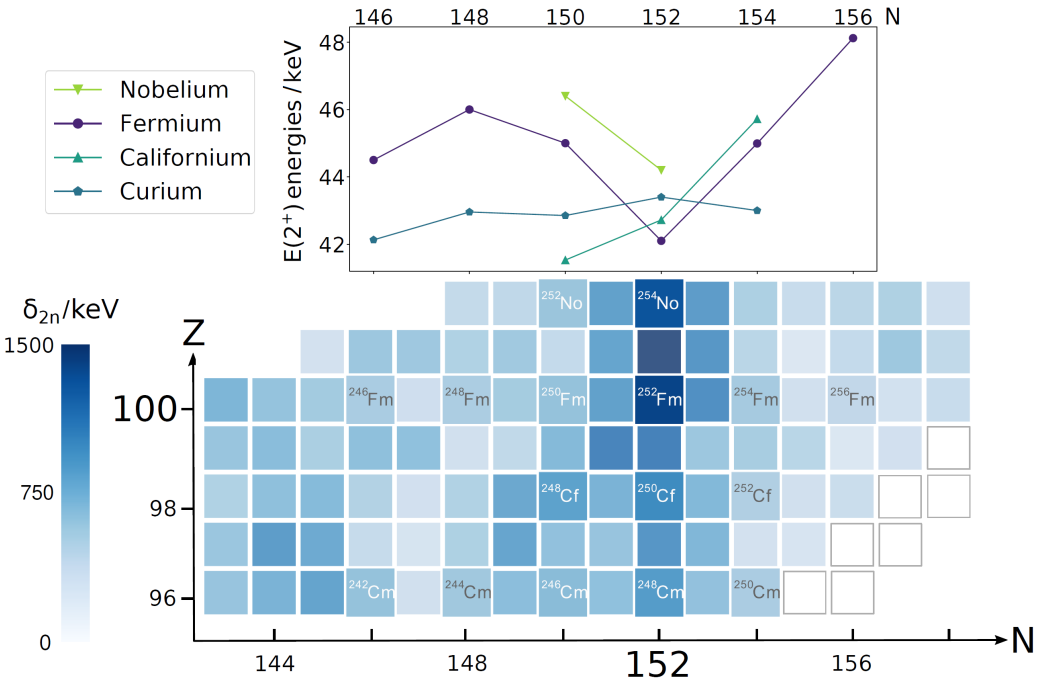

Figure 1: Top: $E(2^+)$ excitation energies for the heavy actinide even-even nuclides showing a deformation maximum in ^{252}Fm. Bottom: Cutout of the nuclear chart for the heavy actinide region around the neutron nuclear shell gap at N=152. The figure was adapted from [5].

come unobservable [16, 17]. At the time of this work, the element with the highest Z that has been experimentally observed is Og with $Z = 118$ [18, 19]. Even though deformation of nuclei must not neccessarily be coupled to shell effects, it is often a consequence of it. Nuclear deformation influences the energy of a nuclear level, leading to large energy gaps between levels which would be different in a spherical nucleus. These gaps qualitatively exhibit the same behaviour as nuclear shell gaps, at the magic numbers, only being smaller in magnitude. They are usually referred to as deformed shell gaps. The influence of deformation on nuclear levels can be described via the Nilsson model [20]. The NSM also explains the existence of nuclear isomeric states [11, 21].

The element plutonium is the heaviest element that is present in nature. With the exception of Neptunium, all elements up to plutonium have at least one naturally occuring isotope [22]. Therefore, neptunium and all ele-

ments with $Z > 94$ must be produced artificially. In principle, elements with a higher Z can be produced via neutron capture reactions and subsequent β^--decays [11]. This principle can be observed in nuclear reactors where elements with a Z higher than the one for the element used as nuclear fuel are produced. These reactors are most commonly used with ^{235}U or ^{238}U with the goal of neutron-induced fission, which subsequently releases more neutrons leading to a self-sustaining chain reaction. However, not all neutron capture reactions lead to induced nuclear fission, enabling the breeding of increasingly heavier elements. The upper limit of this breeding process is determined by the neutron flux available and therefore the reachability of isotopes with an excess of neutrons that primarily decay via a β^--decay. In nuclear reactors this limits the breeding process to the element fermium with $Z = 100$, since this is the first element with no yet known β^--decaying isotope [22]. Elements with $Z > 100$ can, so far, only be produced via multinucleon transfer reactions (MNT) and fusion-evaporation reactions. Both types of reactions need a projectile with high kinetic energy to overcome the Coulomb barrier between both nuclei and are therefore carried out at accelerator facilities, like GSI Darmstadt. Fusion-evaporation reactions are explained in more detail in Sec. 2.4.

One reliable, albeit indirect way, of studying nuclear structure lies in studying the electron shell of an atom via optical spectroscopy. An efficient and precise way of doing optical spectroscopy is utilizing laser light and probing for energy resonances in the absorption of electromagnetic radiation. This can be done, for example, via multi-step excitation, which allows probing transitions into an excited state (ES) ultimately leading to a detachment of the excited electron, ionizing the sample atom. This is called resonance ionization spectroscopy (RIS) [23, 24, 25]. When measuring the same atomic transition in multiple different isotopes of the same element, the occuring isotope shift can be deconstructed into two different components, the mass and the field shift. Since the field shift scales with the nuclear mean-square charge radius $\langle r^2 \rangle$, this property can be determined via laser spectroscopy [26]. The evolution of $\langle r^2 \rangle$ across changing neutron or proton numbers yields information on nuclear structure. In cases were a nuclear shell is being filled, without reaching a fully closed shell, this evolution is linear. In some cases it was found that Kingplots exhibit a kink in their evolution. These kinks in the trend can, e.g., indicate nuclear shell gaps, as well as changes in deformation of a nucleus [27, 28, 29, 30]. Furthermore it is possible to probe the structure of the nucleus via measuring the hyperfine structure (HFS) [31, 32, 9]. From

this interaction between the nuclear spin I and total angular momentum of the electron shell J, the magnetic dipole moment μ_I and spectroscopic electric quadrupole moment Q_s can be determined [33, 34]. The spectroscopic quadrupole moment Q_s is dependent on the intrinsic quadrupole moment Q which reflects nuclear deformation.

Most isotopes of superheavy elements have never been accessible for laser spectroscopy experiments, leaving their atomic and often times nuclear structure to be experimentally largely unknown. While there are approaches to model their atomic structure, the increasing relevance of relativistic effects makes their accurate prediction challenging, or in some cases outright impossible [9]. Through the measuring of observables via laser spectroscopy and other methods, this structure can be investigated leading to a better understanding and modeling of nuclear and atomic behaviour as a whole.

To accurately measure observables relevant for the description of atomic and nuclear behaviour precise measurements with sufficient statistical weight must be conducted. For laser spectroscopy experiments, dealing with very limited quantities of the atoms of interest, high efficiency and spectral resolution are paramount. To achieve this, the in-gas-jet resonance ionization spectroscopy (JetRIS) technique was developed [35]. This technique aims to combine the high efficiency of the filament technique in a buffer gas filled cell, that has been successfully employed in RADRIS [36], with the high spectral resolution of laser spectroscopy in a supersonic gas jet [37] and is described in more detail in sec. 3.2. In this work, the JetRIS was characterized and developed to the point of successfully measuring a $^1\mathrm{S}_0 \rightarrow {}^1\mathrm{P}_1$ ground state transition of ^{254}No with a linewidth of 770 MHz. This involved determining the best conditions for spectral resolution and efficiency in off-line tests for the JetRIS setup. For the spectral resolution different de-Laval type supersonic nozzles were tested under different stagnation pressures and background pressures measuring the light-induced fluorescence (LIF) of ^{164}Dy in the gas jet. Here, optimal conditions were found resulting in a best-case resolution of 212(30) MHz. The details of these measurements can be found in Publication I. To determine the efficiency of the JetRIS setup, a ^{223}Ra recoil ion source was utilized to determine the transport efficiency. This ion source releases the daughter of ^{223}Ra, ^{219}Rn into its surroundings, due to the recoil of the α-decay. Since the activity of this source can be measured, the release rate can be determined to enable measurements of the transport efficiency of the JetRIS setup. After characterization and optimization, the setup was used at the GSI facility in Darmstadt for the aforementioned RIS experiments on

^{254}No. For the production, the accelerator of GSI was utilized to sustain a fusion-evaporation reaction of the type ^{48}Ca + ^{208}Pb $\rightarrow$ ^{254}No + 2n with ^{48}Ca as the projectile [38]. For the separation of the primary beam from the reaction product the Seperator for Heavy Ion reaction Products (SHIP) was used [39, 40]. The details of the results of the efficiency measurements and the spectroscopy on ^{254}No can be found in Publication II.
For future improvements a Multiple Reflection Time-of-Flight Mass Spectrometer (MR-ToF MS) [41] will be added to the JetRIS in order to allow for ToF-based ion detection. The MR-ToF MS used here was conceptualized by M. Schlaich in the context of Darmstadt's MR-ToF collaboration (Da's MR-ToF collaboration) and the design was published in [42]. Within this collaboration the electrodes of the MR-ToF MS were manufactured jointly by all collaborating institutes and distributed. The assembly, comissioning and optimization of this device were done by the author of this work. The final comissioning included tests of the mass resolving power and efficiency of the MR-ToF MS using a self-built laser ion source utilizing two-step RIS on ^{nat}Sm. The comissioning was coupled with laser excitaion scheme development for samarium which included determining the hyperfine parameter $\mathcal{A}$ on Sm isotopes with $I \neq 0$ and determining the mass and field shift from the isotope shift via Kingplot analysis for all measured transitions [26]. The results of these measurements can be found in Publication III.

2 Theoretical background

This section provides a brief overview of background information to guide the reader through the topics covered in this thesis and to provide some necessary background information. In cases where the fundamentals of the theory are already well established in detail in the literature (e.g. textbooks, review articles), this section will be intentionally brief and rather provide references to these sources than rewrite them without added benefit.

2.1 Laser spectroscopy

Laser spectroscopy refers to optical spectroscopy in which the source of the electromagnetic radiation used is a laser [23, 31]. Laser is an acronym for light amplification via stimulated emission of radiation [43, 44, 45]. Its benefits for optical spectroscopy are that lasers produce highly coherent light with a spectral bandwith that, depending on the laser, can range between a few millihertz and multiple gigahertz. There are tunable lasers, in which the wavelength of the emitted light can be varied by 10s or 100s of nanometers and lasers with a static wavelength. The former are usually used for optical spectroscopy, while the latter are used as a reference for the wavelength or for pumping an optical medium of a tunable laser. Laser spectroscopy in general probes atomic structure through resonantly exciting electronic levels. To obtain a signal in a measurement whether, or to which probability the atom has successfully been excited, there are two ways relevant to this thesis which are well established. These are **L**ight-**I**nduced **F**luorescence (LIF)[46, 47] and **R**esonance **I**onization **S**pectroscopy (RIS) [24, 25, 48, 49, 50]. When an atom is in an electronically excited state, it can spontaneously relax to the ground state through the emission of electromagnetic radiation [43, 34]. This radiation is emitted in a random direction, so that the sum of many emissions is a uniform distribution in 4π. The lifetime of excited atomic states ranges from the order of nanoseconds to seconds. In this work we focus on electric dipole transitions, where the lifetime ranges from nanoseconds to microseconds. For RIS, usually multiple excitation steps are necessary. Usually two steps are used, being called the first excitation step (FES) and second excitation step (SES). The first excitation step is always done resonantly from the ground state, or a thermally excited state. The second step, used for ionization, can be done resonantly through Rydberg states or auto ionizing (AI) states, or non-resonantly. Rydberg states are bound, excited electronic states close to,

but below the ionization potential (IP), which can be ionized via collisions or electric fields. AI states result from multi-electron excitations. Here, the total energy is higher than the IP, so that the system can decay to the ionic ground state by transfering its energy onto one, unbound electron. These types of SES have different interaction cross sections σ and therefore different power requirements for saturation. Rydberg states have the highest σ, which is approximately 10 times as large as the σ of AI states and 10000 as large as the σ of non-resonant ionization [51]. Albeit Rydberg states typically have a rather narrow spectral profile, which is for doppler broadened ensembles not ideal. AIs and Rydberg states are not always known for the heaviest elements, especially when searching for first excited levels [19]. An example of an excitation scheme can be found in Fig. 2.

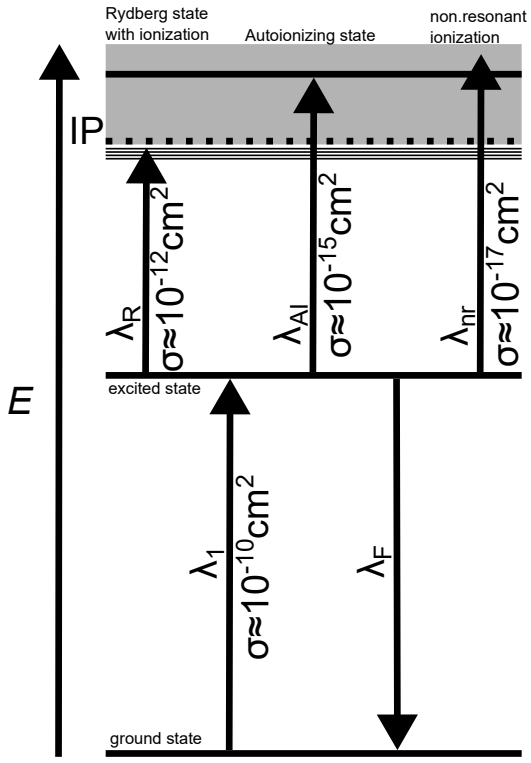

Figure 2: Exemplary level scheme showing the FES through λ_1, fluorescence through λ_F, Rydberg excitation via λ_R, auto ionizing states via λ_AI and non-resonant ionization through λ_nr. Adapted from [51].

2.1.1 Spectral resolution

When atoms are resonantly excited the lines that are measured are not infinitely sharp δ-functions, but show a usually symmetric distribution of signal around a centroid value [23]. The width of this distribution is known as spectral resolution or spectral linewidth and is usually characterized by the value of the **F**ull **W**idth **H**alf **M**aximum (FWHM). This value is influenced by multiple broadening mechanisms and the lowest achievable linewidth is the so called natural linewidth. Due to the Heisenberg uncertainty principle [52] the errors in energy and time are connected to one another and their product has a lower absolute limit. Due to this the lifetime of an excited state influences the minimum achievable spectral linewidth with a shorter lifetime leading to a larger spectral linewidth according to

$$\delta\nu = \frac{1}{2\pi\tau}, \tag{1}$$

with $\delta\nu$ being the spectral linewidth and τ being the lifetime of the excited state [34]. In any experiment the spectral linewidth is determined by a combination of all broadening mechanisms. In the context of this work these are the natural linewidth, pressure broadening, Doppler broadening and saturation broadening and the spectral bandwith of the laser system [23, 31, 34]. Contributions to the overall spectral linewidth of an experiment which stem from the lifetime of the excited state exhibit a Lorentzian shaped profile [23]. The pressure broadening exhibits the same profile. It stems from the collision between atoms. This can lead to a depopulation of an excited electronic state via collisional energy transfer, leading to a decreased effective lifetime of that state. In cases where the collision does not lead to a deexcitation it can still influence the phase relationship between the excited atomic dipole and the laser light, broadening the spectroscopic line. This mechanism is dependent on the pressure. The Doppler broadening contributes via a Gaussian shaped profile and is dependent on the temperature. It stems from the fact that the thermal kinetic energy of an ensemble of particles follows the Boltzmann distribution, instead of being a uniform value for every particle [53, 54]. This energy is also undirected, so that it shows a random distribution in 4π. With these properties an ensemble of particles always has atoms moving perpendicular to an incoming laser beam, meaning they are not Doppler shifted [55] and distributions of velocities and angles that either red- or blueshift a particular particle, leading overall to a broadening of the

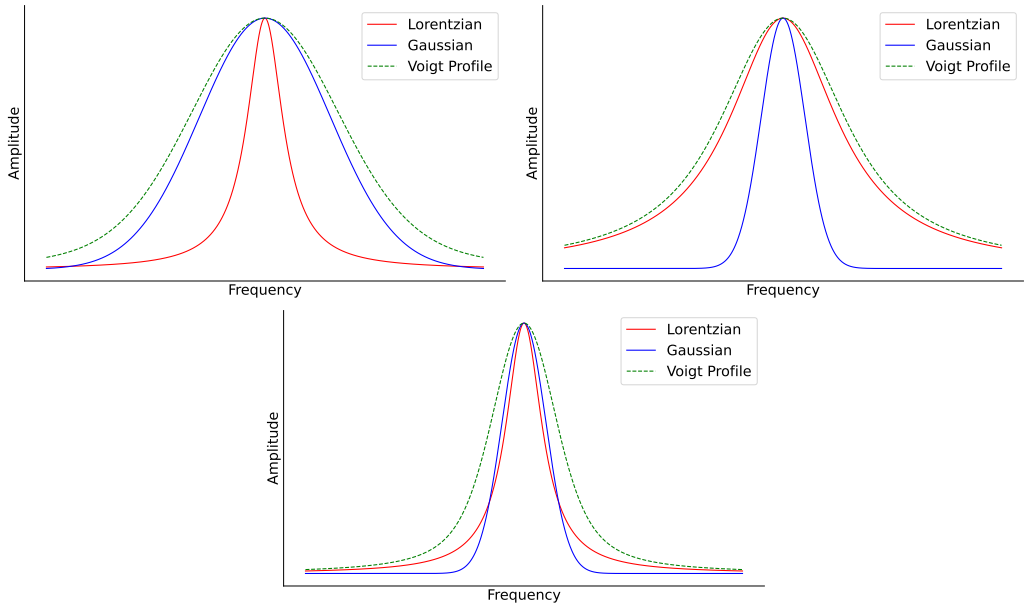

Figure 3: Examples of different Gaussian (σ) and Lorentzian (Γ) contributions to a Voigt profile. The ratios of σ to Γ are 3:1 (top left), 1:3 (top right) and 1:1 (bottom).

resonance. The spectral bandwith of the laser that is used contributes to the measured spectral linewidth with the shape of the bandwith, which is the Boltzmann distribution of velocities in one direction. Spectra that are not dominated by one type of lineshape, but are a combination of Gaussian and Lorentzian shapes can be described by a Voigt profile, which is the mathematical convolution of both [56]. In a Voigt profile the individual contributions of both lineshapes can still be identified and analysed (c.f. Fig. 3). Power broadening contributes with a Lorentzian lineshape. In any experiment there is a finite amount of particles that can be excited. The probability of excitation is dependent on the power and excitation cross section. At some photon density all available particles will be excited at the resonance frequency, with the signal decreasing if the laser is detuned. If the photon density gets increased further the signal can't increase anymore at the resonance frequency, while still increasing at the detuned position leading to a plateau like structure in the center of the transition.

2.1.2 Isotope shift

The resonance energies of the same electronic transitions between two isotopes of the same element are not identical. This behaviour is referred to as isotope shift $\delta\nu^{\mathrm{A,A'}}$ [57, 23, 58]. It is a result of the difference in the center-of-mass motion of the nucleus-electron system for different nuclear masses, as well as different nuclear volumes for different isotopes. The isotope shift is also specific to the electronic transition, since different electronic orbitals have different probabilities for an electron to be inside the nucleus. It can be written as

$$\mu^{\mathrm{A,A'}} \cdot \delta\nu^{\mathrm{A,A'}} = K + F_{\mathrm{s}} \cdot \mu \cdot \delta\langle r^2 \rangle^{\mathrm{A,A'}}, \tag{2}$$

with K being the mass shift, F_{s}, being the field shift, $\delta\langle r^2 \rangle^{\mathrm{A,A'}}$ being the nuclear mean-square charge radius and $\mu^{\mathrm{A,A'}}$ is the reduced mass which is given by

$$\mu^{\mathrm{A,A'}} = \frac{M_{\mathrm{A}} M_{\mathrm{A'}}}{M_{\mathrm{A}} - M_{\mathrm{A'}}}. \tag{3}$$

M_{A} is the mass of the reference isotope. K and F_{s} can be determined via a King plot, where $\mu \cdot \delta\nu^{\mathrm{A,A'}}$ is plotted as a function of $\mu \cdot \delta\langle r^2 \rangle^{\mathrm{A,A'}}$ [59, 58, 26] if the charge radii are known from independent measurements. One expects a linear trend with the y-intercept being equal to K, while the slope is equal to F_{s}. If the nuclear mean square charge radius is not known, one can use a Kingplot as a consistency check for the data, plotting $\mu \cdot \delta\nu^{\mathrm{A,A'}}$ of one transition against the same parameter of another transition from the same isotopes. If the field shift can be determined via spectroscopy or atomic theory calculations it can be used to determine the relative charge radii for isotopes of the same element, as was done in the past for the elements fermium and nobelium [60, 61]. If the data is consistent it needs to exhibit a linear trend. Kingplot analysis was used in Publication III. A schematic representation of the isotope shift can be seen in Fig.4.

2.1.3 Hyperfine structure

Hyperfine structure is a splitting of an atomic level due to a coupling between the nuclear spin I and the total angular momentum J of the electron [63]. A nucleus with a spin of $I \neq 0$ features a nuclear magnetic dipole moment μ_{I}. In that case the magnetic field from the electron shell at the nucleus $B_{\mathrm{e}}(0)$ with $J \neq 0$ leads to an orientation-dependent energy splitting according to

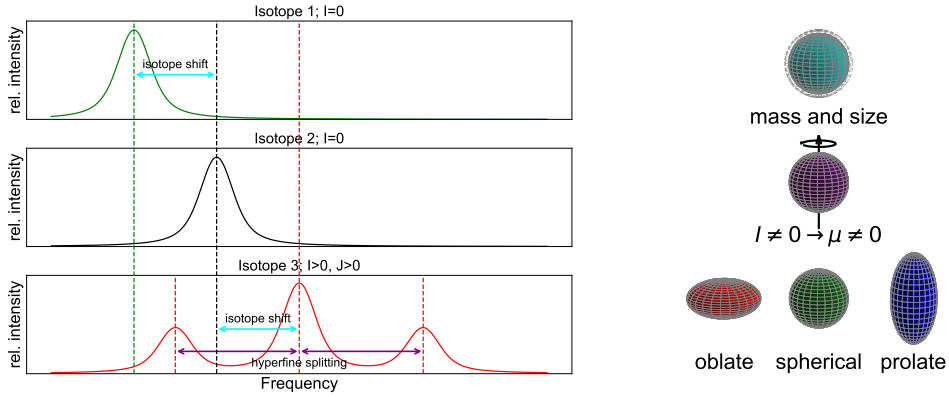

Figure 4: Schematic illustration of the dependency of isotope shift and hyperfine splitting to the physical properties of an atomic nucleus. The transition centroid differs between different isotopes due to the isotope shift (cyan arrow), while the lower plot shows a hyperfine splitting due to a non-zero nuclear sping and total angular momentum of the electrons. Figure adapted from [62].

the Zeeman effect [34]. The magnetic hyperfine energy splitting $\Delta\nu_{\mathrm{mag}}$ can be described by

$$\Delta\nu_{\mathrm{mag}} = \frac{\mathcal{A}}{2} \cdot C \tag{4}$$

with

$$C = F(F+1) - J(J+1) - I(I+1) \tag{5}$$

and

$$\mathcal{A} = \frac{\mu_{\mathrm{I}} \cdot B_{\mathrm{e}}(0)}{h \cdot I \cdot J}. \tag{6}$$

F is the atomic total angular momentum with $F = J + I$.
For non-spherical nuclei the charge distribution leads to an intrinsic nuclear electric quadrupole moment Q, with $Q < 0$ for oblate and $Q > 0$ for prolate deformation. Its interaction with the electric field gradient from the electron shell at the nucleus $\left.\frac{\partial^2 V}{\partial z^2}\right|_{\mathrm{r}=0}$ gives rise to an additional splitting in analogy to the Stark effect [58]. The electric hyperfine energy splitting $\Delta\nu_{\mathrm{el}}$ can be described as

$$\Delta\nu_{\mathrm{el}} = B\frac{\frac{3}{4}C(C+1) - I(I+1)J(J+1)}{2I(2I-1)J(2J-1)}, \tag{7}$$

with

$$\mathcal{B} = \frac{e \cdot Q_{\mathrm{s}}}{h} \frac{\partial^2 V}{\partial z^2}\bigg|_{\mathrm{r}=0}. \tag{8}$$

Q_{s} is the spectroscopic quadrupole moment, which can be linked to the intrinsic quadrupole moment over the nuclear spin I and its projection upon the symmetry axis of the nucleus K via the following equation:

$$Q = \frac{(I+1)(2I+3)}{3K^2 - I(I+1)} \cdot Q_{\mathrm{s}} \tag{9}$$

Hyperfine analysis was done in Publication III.

2.2 In-gas-jet spectroscopy

The power of spectroscopic methods is typically defined by their spectral resolution and their efficiency. To achieve a high spectral resolution the broadening mechanisms explained in sec. 2.1.1 must be adressed. This can be achieved by creating a low-temperature, low-pressure environment, while tuning laser power density to the atomic transition and using a laser with a low bandwidth. To achieve high efficiency the atomic/ionic path must be well defined and sufficient laser power density must be available to saturate the transition. In-gas-jet spectroscopy is a technique that utilizes gas-expansion from a high-pressure region, to a low-pressure region through a de-Laval type nozzle, to achieve a well-collimated, hypersonic gas jet [37, 64]. The pressure difference through the nozzle leads to a conversion of undirected thermal energy to a directed kinetic flow of the gas. This expansion process results in a reduction in relative movement of the gas molecules between each other, i.e. a low temperature, which follows a Maxwell-Boltzmann distribution. The converging-diverging shape of the de-Laval nozzle is important for the formation of a well-colimated gas jet and the nozzle shape has to be adapted for each operation condition [37]. Since the environment inside a hypersonic gas jet is low-temperature and low-density by nature, as well as it having a well-defined geometry it is a technique that is well suited to supplement and improve gas-cell techniques. This method was applied in the JetRIS which was utilized in Publication I and Publication II. A picture of the gas jet from JetRIS can be found in Fig. 5.

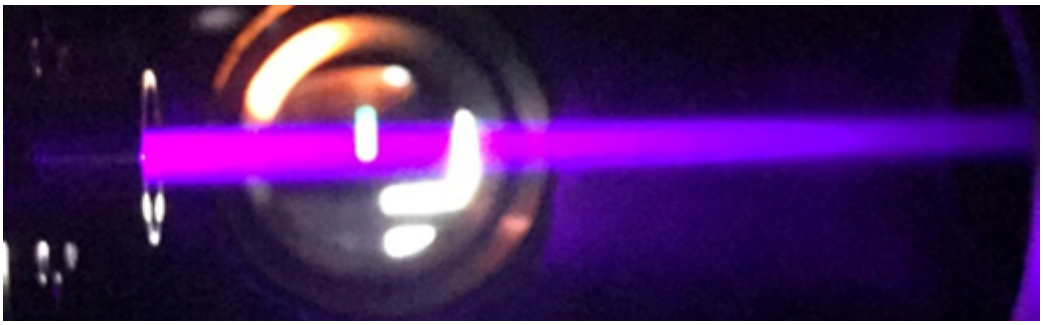

Figure 5: Picture of fluorescence-light of ^{164}Dy in the gas jet of JetRIS at 404.5 nm.

2.3 Mass spectrometry

Mass spectrometry is a general term for techniques that seek to measure the mass of an object, or identify and discriminate an analyte via its mass. If measured precisely enough, mass spectrometry is a powerful tool with a lot of applications for analytical purposes and fundamental physics. It features high sensitivity and can analyze multiple species that are together in the same sample [65]. This work focuses on **T**ime-**o**f-**F**light (ToF) mass spectrometry, which is a subset of mass spectrometry that utilizes the connection between kinetic energy E_{kin} with the velocity v and mass m of an object, given by the following equation:

$$E_{\text{kin}} = \frac{1}{2}mv^2 \tag{10}$$

This technique uses electric fields for ion manipulation, which leads to discrimination of different species due to their mass-to-charge ratio (m/q) according to the following equations [66, 67]:

$$E_{\text{kin}} = qU \tag{11}$$

$$t = \sqrt{\frac{m}{2qU}}d \tag{12}$$

U is the difference in potential between the start- and endpoint of the acceleration, t is the flighttime of the ion and d is the distance travelled. This gives the possibility of measuring charge-state distributions of analytes from ionization methods, but can also result in unwanted interference between species, making unambiguous identification more difficult without sufficient mass resolving power. The mass resolving power R is a quality criterion of mass spectrometry. It is defined as

$$R = \frac{m}{\Delta m} = \frac{t}{2\Delta t} \tag{13}$$

with Δm being the width of the mass peak and Δt the width in time of flight respectively [68]. With this definition two ToF/mass peaks are resolved if they overlap within at most one FWHM or are further apart. An example of this can be seen in Fig. 6 The more similar the masses are, the higher the mass resolving power is needed for clear separation. In applications, cases can range from separation of isotopes which require a few ten to hundred mass resolving power, to isobaric separation which can require $R = 10^5 - 10^6$

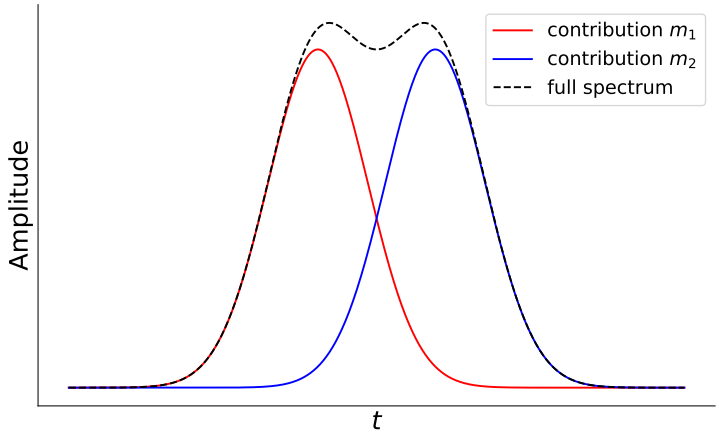

Figure 6: Exemplary ToF-spectrum of two species with different masses m_1 and m_2 with identical abundance separated by one FWHM (black, dashed line) with their individual contributions (red and blue curves).

in mass resolving power and beyond. This is the current limit of what can be reliably achieved in sophisticated ToF devices [69]. For measurements of smaller mass differences, e.g. nuclear isomers, other methods, usually Penning traps, are used. The predicted necessary values of R are only valid in cases where the abundance ratio of the different species is close to one [68].

2.4 Fusion-evaporation reactions

Fusion-evaporation reactions are nuclear reactions that are often used to produce heavier nuclei, even superheavy nuclei, from lighter, more abundant nuclei [11, 70, 71]. Two nuclei are brought into close contact with each other, resulting in nuclear fusion. To get sufficient proximity of the reactands, the Coloumb barrier needs to be overcome. Due to the introduced energy, this compound nucleus is in a highly excited state. Since the Coloumb force scales with the product of both particle charges, asymmetric reactions are often preferred for a higher fusion probability, even though they lead to a higher excitation energy of the compound nucleus [70]. These reactions are done with the lighter reactand being accelerated to the necessary kinetic energy, usually on the order of MeV per nucleon, e.g. at the UNILAC accelerator at GSI, Darmstadt and being used as a projectile on a fixed, thin target made of or containing the heavier reactand. The compound nucleus carries a lot of the momentum that the projectile provided and flies out of the target material. The compound nucleus evaporates nucleons depending on its exitation energy, yielding the reaction product, often referred to as evaporation residue. These products are usually radioactive and neutron deficient, as the ratio of neutrons to protons for maximum stability increases for heavier nuclei [11]. The product nuclei are often times in an excited state, making this technique viable for research on nuclear isomers [22]. Fusion evaporation reactions have been used in Publication II for the production of ^{254}No via a 2n channel. A sketch of this process can be found in Fig. 7.

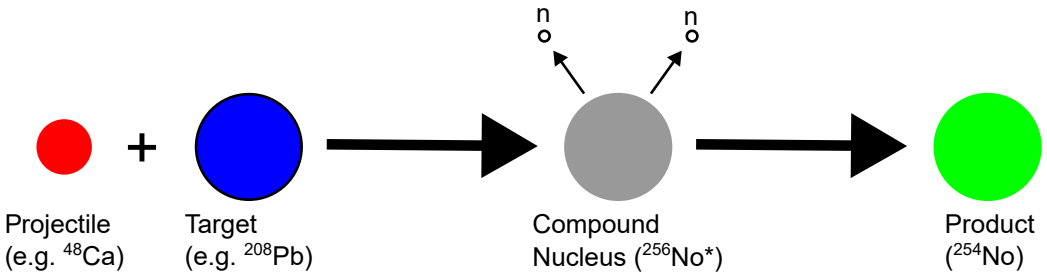

Figure 7: Sketch of the production of ^{254}No via a ^{208}Pb(^{48}Ca,2n) fusion-evaporation reaction.

The reaction of ^{208}Pb(^{48}Ca,2n)^{254}No has been chosen, since it has previously been found to be optimal for the production of ^{254}No, as shown in Fig. 8. In principle, the fusion cross section scales positively with the projectile en-

ergy. This also leads to a higher excitation energy of the nucleus, leading to different yields and ratios of different evaporation channels and nuclear fission. Therefore there is an optimal projectile energy for which the yield of a particular isotope is maximized.

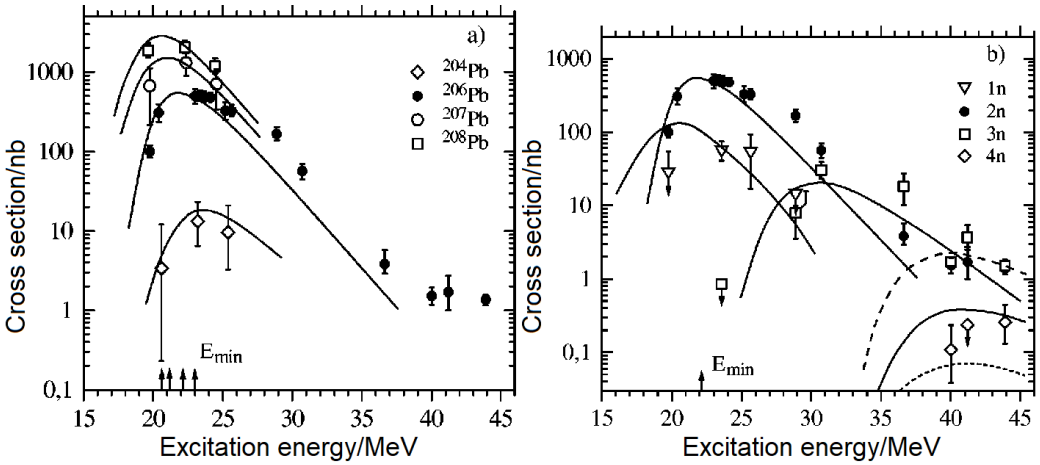

Figure 8: a) Excitation functions of fusion evaporation reactions between different isotopes of Pb targets with a ^{48}Ca projectiles. b) Excitation functions for different evaporation channels of the reaction between ^{206}Pb and ^{48}Ca. Figure adapted from [60].

3 Experimental techniques

3.1 SHIP

The **S**eparator for **H**eavy **I**on reaction **P**roducts (SHIP) is a velocity filter, built for the separation of nuclear reaction products from the primary beam [39]. A schematic overview of this setup is shown in Fig. 9. SHIP was

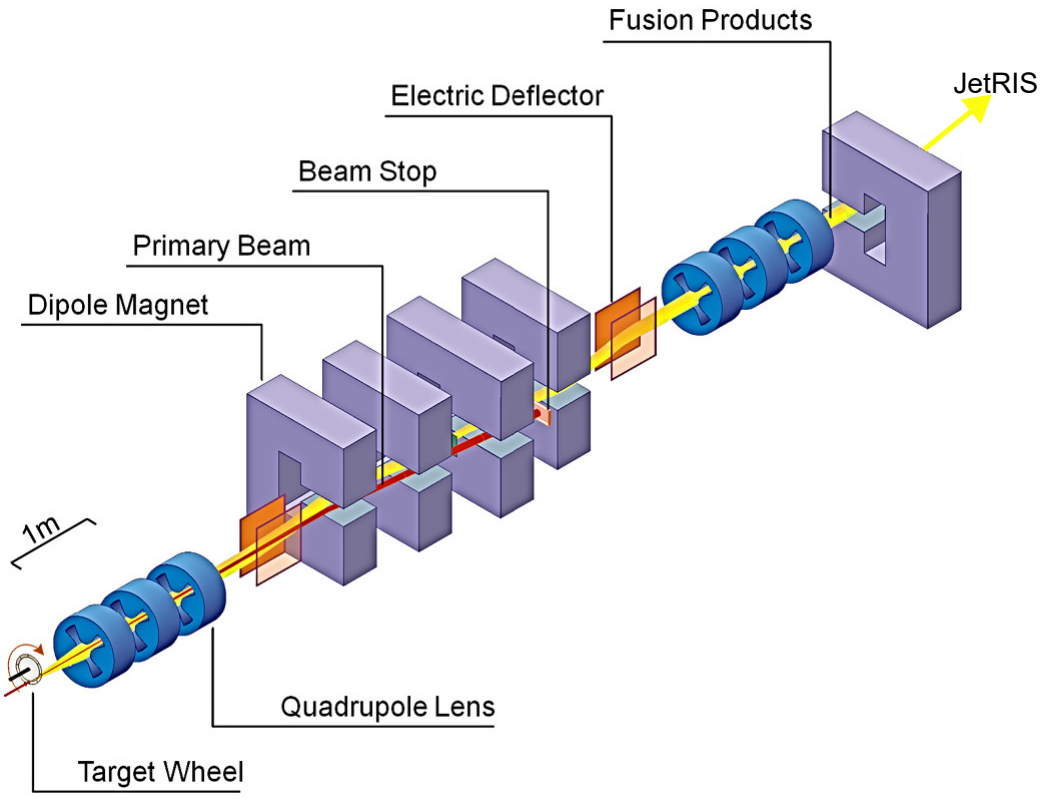

Figure 9: Schematic drawing of SHIP. The primary beam (red) hits the rotating target wheel, producing recoil ions (yellow) from fusion-evaporation reactions. The primary beam is separated from the rest via a superposition of electric and magnetic fields and the reaction products are transported to JetRIS. Figure adapted from [72].

used for the on-line production of ^{254}No through the ^{208}Pb(^{48}Ca, 2n) fusion-evaporation reaction in Publication II. In SHIP, the target consists of a thin foil made out of the target material or, in case of actinide targets the tar-

get material is deposited on a thin Ti backing foil. Eight foils are placed on a wheel that rotates synchronized with the pulsed primary beam. This distributes the accruing heat from the energy loss. Such target foils have a typical areal density of $0.5\,\frac{\mathrm{mg}}{\mathrm{cm}^2}$. For the nobelium production the primary beam consists of $^{48}\mathrm{Ca}^{10+}$, accelerated to a kinetic energy of 4.55 MeV per nucleon with a beam intensity of roughly $5 \cdot 10^{12}\,\frac{\text{particles}}{\mathrm{s}}$ [73]. After the target wheel a quadrupole triplet lens is placed to focus the diverging beam consisting of the primary beam and the reaction products to minimize losses. Behind this lens are multiple static electric and magnetic deflectors which form a velocity filter [74]. The Lorentz force from the magnetic field and the electric force cancel each other for a certain velocity v, depending on the electric field strength E and the magnetic field B according to

$$v = \frac{E}{B}. \tag{14}$$

These values are tuned that the fusion-evaporation product with a kinetic energy of 41 MeV in the case of ^{254}No can pass the filter, while the primary beam is deflected. After the velocity filter, another quadrupole lens refocuses the beam, followed by another dipole magnet, to further deflect scattered primary beam particles. The fusion evaporation reaction products fly further towards a measurement setup, in this case JetRIS, where they are used for experiments. For identification of these reaction products, a ToF-detector and a 16-strip silicon detector can be inserted at the end of SHIP. SHIP reduces the background intensity of the primary beam from the initial $5 \cdot 10^{12}\,\frac{\text{particles}}{\mathrm{s}}$ to roughly $1\,\frac{\text{particle}}{\mathrm{s}}$ [75].

3.2 JetRIS

The in-gas-**Jet** **R**esonance **I**onization **S**pectroscopy (JetRIS) is a setup for on-line laser spectroscopy experiments utilizing fusion-evaporation reactions and a hypersonic gas jet. It has been built by a former PhD student, Steven Nothhelfer [35] and conceptual papers have been published on this [76]. During the current work, the performance of the JetRIS has been characterized by LIF measurements on ^{164}Dy, summarized in Publication I. It has been utilized in on-line measurements on ^{254}No, summarized in Publication II and upgraded over the course of this thesis. It was inspired by the RADRIS technique, employed by our group at GSI [77, 78] and the IGLIS technique, developed by collaboration partners at KU Leuven [37]. A schematic drawing of JetRIS can be seen in Fig. 10.

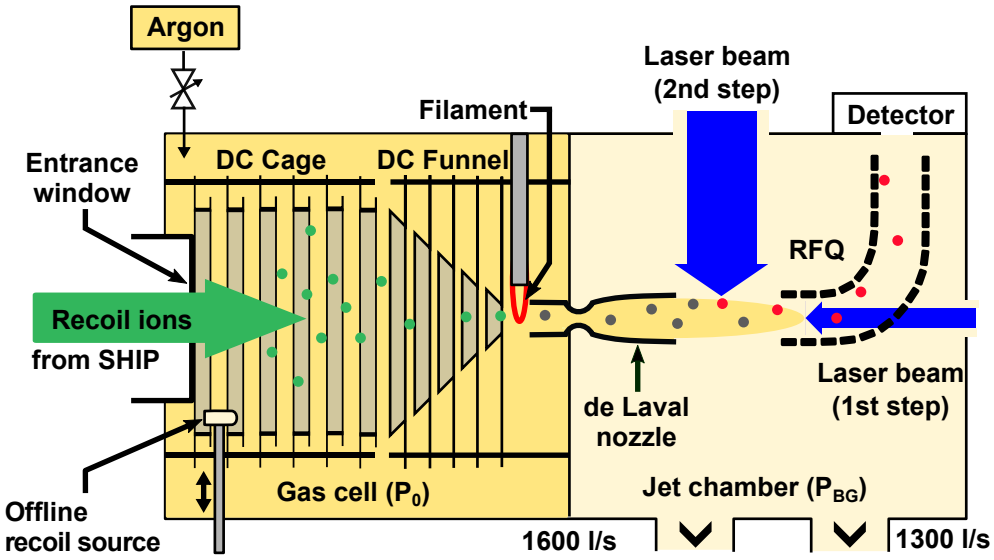

Figure 10: Schematic drawing of the JetRIS setup. Recoil ions (green points), incoming from SHIP, are stopped in the 80 mbar argon buffer gas in the gas cell. They are transported via static electric fields to the hot filament, where they are neutralized. The neutralized atoms (grey points) follow the gas flow through the de Laval nozzle into the Jet chamber, where they are ionized via two-step RIS (red points, blue arrows). The ions are transported via a 90° bend RFQ to an α-detector. Figure adapted from [79].

It consists of two central cells for varying pressure regimes, called the gas cell and the jet chamber. The gas cell is filled with a stagnation pressure of

$P_0 = 80\,\text{mbar}$ of argon gas. Both chambers are connected via a hole with a diameter of 1 mm on top of which a de-Laval type nozzle is mounted. The jet chamber is evacuated to a background pressure of $P = 7.0 \times 10^{-3}\,\text{mbar}$. With the pressure difference a gas flow from the gas cell to the jet chamber is achieved, which is formed into a collimated hypersonic gas jet by the nozzle. Inside the gas cell there are 6 cylindrical electrodes forming the DC cage, followed by 5 electrodes with successively decreasing diameter, being the DC funnel, followed by a thin tantalum metal wire, called the filament. Following the filament, there is the channel electrode. In on-line experiments there is a thin entrance window made of titanium at the first channel electrode which allows high-energy, high-charge recoil ions made from fusion evaporation reactions, separated by the **S**eperator for **H**eavy **I**on reaction **P**roducts (SHIP) to enter the gas cell. In the gas cell these ions are thermalized as singly charged ions due to collisions with the argon buffer gas. Electric potentials are applied to the electrodes, so that the filament is at the lowest potential, being the most attractive point for cations. This electric field gradient drags the ions in the gas cell towards the filament where they get neutralized and adsorbed via direct contact. The filament is resistively heated to a typical temperature between 1000 °C and 1400 °C, depending on the produced element. Due to this temperature, the now neutralized atoms of interest are released into the gas phase, where they are now guided by the gas-flow through the hole into the jet chamber. As this atom is now inside the hypersonic gas jet it experiences its low-temperature, low-pressure conditions. Inside this hypersonic gas jet two laser beams are overlapped spacially and temporally, for two-step RIS. The FES is introduced in an anti-collinear geometry to maximize power density and ensure efficient excitation. Since the SES is usually done non-resonantly due to a lack of available data on atomic states, it is introduced via a perpendicular geometry to avoid shining the high power laser onto the nozzle and damaging it in the process. A **R**adio **F**requency **Q**uadrupole (RFQ) structure is placed 6 cm after the end of the nozzle. This RFQ features a 90° bend to effectively guide the ions around a curve to separate them from the neutral charged atoms towards a silicon detector for α detection. Because of the continuous release process and the 6 cm gap between nozzle and RFQ used for the ionization process, a high repetition rate laser system is necessary for efficient ionization. Since the terminal velocity of a hypersonic argon gas jet with a stagnation temperature of $\approx 300\,\text{K}$ is $558\,\frac{\text{m}}{\text{s}}$ a laser repetition rate of at least 9.3 kHz is necessary to ensure that every atom has seen at least one laser pulse. This velocity

would be reached for an ideal gas jet, where all of the kinetic energy is directed through the nozzle. During the thermalization process every recoil ion produces millions of argon ions, which are also guided towards the nozzle by the electric field gradient, and persist in the form of Ar^+ and Ar_2^+. A portion of these ions will not be neutralized by the filament. The remaining ions can be transported through the nozzle and bender RFQ, reaching the detector and producing a large background signal, making direct ion detection not a viable option without a reliable method to discriminate signal ions from background ions. Due to this inherent background of stable ions, the JetRIS method has relied on measurements of α-decay detection, limiting the potential of this technique drastically. A reliable way for discrimination can be found in **T**ime-**o**f-**F**light **M**ass **S**pectrometry (ToF-MS). For this purpose, a **M**ultiple-**R**eflection **T**ime-**o**f-**F**light **M**ass **S**pectrometer (MR-ToF MS) was acquired and comissioned. With the implementation of discriminated direct ion detection nuclides which do not decay via an α-decay channel, including long-lived and stable nuclei, could be measured. The device itself will be explained in detail in sec. 3.5, while its results are part of Publication III.

3.3 Laser system

Two different types of laser systems have been used throughout this thesis. For the LIF measurements in Publication I a continuous-wave (CW) diode laser has been used. This laser used a 405 nm diode (Thorlabs L405P20) with an external cavity in Littrow configuration. This cavity has been built by a neighbouring group and was available through a collaboration. This laser featured a sub-MHz linewidth with a maximum power of 12 mW. For the two-step RIS measurements described in Publication II and Publication III, the laser system shown in Fig. 11 was used. For Publication II a frequency-tripled Nd:YAG was used for the SES instead of the Credo laser.

3.3.1 Narrowband Laser System (used for FES in Publication II and Publication III):

A narrowband laser setup was employed, consisting of a pulsed dye amplifier (PDA, Sirah Lasertechnik) pumped by a high-power, single-mode, pulsed, frequency-doubled Nd:YAG laser (PXn300-2-GFSLM, Edgewave). The PDA was seeded by a tunable, single-mode CW dye laser (Matisse, Sirah Lasertechnik), which itself was pumped by a CW, frequency-doubled Nd:YAG laser (Millenia, Spectra Physics). Frequency doubling of the PDA output was performed using a single-pass second-harmonic generation (SHG) unit with a β-barium borate (BBO) crystal. Single-mode operation of the pump laser was essential to suppress unwanted excitation from side modes [80]. The resulting narrowband output had a spectral linewidth of $\delta f_{\mathrm{nb}} = 139(13)$ MHz after SHG, measured using a Fabry-Pérot interferometer (FSR = 1 GHz, Toptica), and a pulse width of 5 ns (FWHM).

3.3.2 Broadband Laser System (used for SES in Publication III):

The broadband system consisted of a pulsed dye laser (Credo, Sirah Lasertechnik) pumped by a frequency-doubled Nd:YAG laser (InnoSlab IS400-2-L, Edgewave). According to manufacturer specifications, this system has a spectral linewidth of $\delta f_{\mathrm{bb}} = 1.8$ GHz. The measured pulse width was 8 ns (FWHM). Both pump lasers support repetition rates ranging from 10 kHz down to single-shot operation.

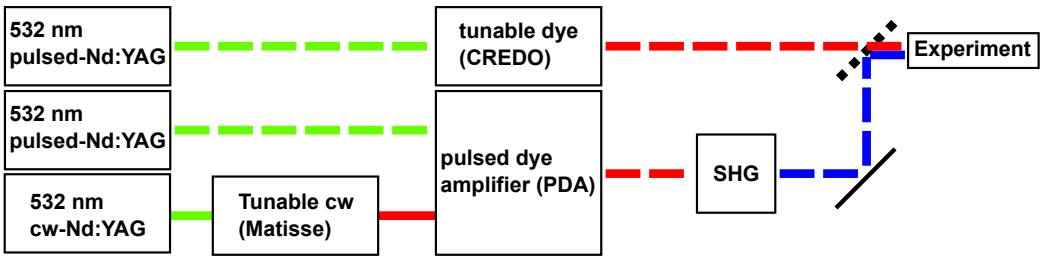

Figure 11: Schematic drawing of the laser system applied in Publication III. The FES was applied using a tunable CW dye laser, pumped by a frequency doubled CW-Nd:YAG laser that was used for seeding a pulsed dye amplifier, pumped by a pulsed, frequency doubled Nd:YAG. The output was frequency doubled and moved to the experiment. The SES was done by a tunable dye laser, pumped by a pulsed, frequency doubled Nd:YAG laser. For Publication II a frequency tripled Nd:YAG was used for the SES instead.

3.4 Laser ion source

For comissioning tests of the MR-ToF MS the planned cooler buncher was not yet available, making a coupling with JetRIS not expedient at the time. This lead to the necessity of the development of an ion source usable for ToF mass spectrometry. Over the course of this thesis two designs were iterated and used. The first one being a chopped continuous ion source, which was used in the early comissioning stages. This ion source was not used for the results in any of the publications present in this thesis. Its performance and design are described in detail in the masters thesis of Christian Helmel [81]. The other ion source built by the author, is a laser ion source, utilizing the JetRIS filament technique and relying on pulsed lasers for resonant ionization. Timing and beam properties were therefore mostly determined by the laser. This source was used for the ToF-assisted laser spectroscopy experiments and performance characterization of the MR-ToF MS shown in Publication III. A schematic drawing of it can be seen in Fig. 12. The laser ion source consists of 5 electrodes. At the beginning there is a

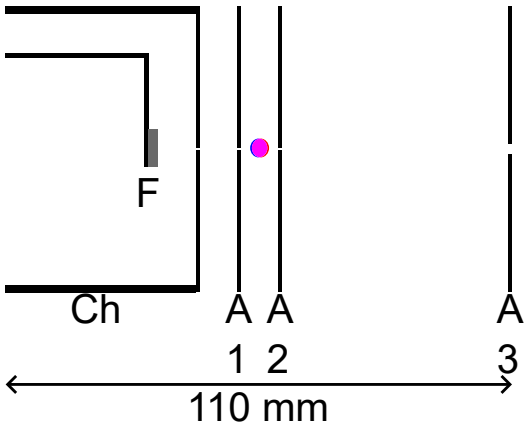

Figure 12: Schematic drawing of the self-built laser ion source. F is the filament, Ch the channel electrode, A1-3 the apertures used for acceleration. The coloured spot between A1 and A2 indicates the overlapped laser beams used for ionization.

filament (F) made out of a thin strip of tantalum metal foil that can be resistively heated and which is folded to contain a pocket in which a piece of the element to be studied can be inserted. In the case of the aforementioned publication this element was samarium with a natural isotope composition.

Around this filament, a cylindrical channel (Ch) is mounted with a central hole of 3 mm in the end cap acting as an aperture. Along the flight path there are three more apertures (A1-3). The first two have a central hole with 1 mm diameter and a distance of 1 cm to the aperture in front of it and the last one has a central hole with 3 mm diameter and a distance of 6 cm to A2. This design allows for a suppresion of cations and electrons coming from glow emission with electric fields. The laser ions are created by resonant laser ionization between A1 and A2 in a low electric field gradient (minimizing of ToF width and energy spread) and are accelerated to the final desired kinetic energy between A2 and A3. For the MR-ToF MS, an injection energy of approximately 3 keV is desirable. For the results in Publication III F was set to 25 V, Ch to 0 V, A1 to 3090 V, A2 to 3000 V and A3 to 0 V. In this configuration, the electron emission is deflected between F and Ch and the cation emission is deflected between Ch and A1, leaving only neutral atoms after A1. The gradient between A1 and A2 is 90 V/cm. This gradient was chosen as it was found to be the point of time focus on the detector leading to a minimal ToF width. ToF width and energy spread are correlated by the electric field gradient and the spacial and temporal overlap volume between both lasers between the electrodes. Due to a non-zero spacial volume, different ions start at different points in the electric field and therefore get accelerated to a different kinetic energy. Because of the temporal width of the SES laser pulse of 8 ns (FWHM), not all ions are created at the same time, leading to an initial ToF distribution. The energy spread scales linearly with the potential gradient and the radial area of the ionization volume. The ToF distribution is less straightforward. In principle, it is inversely correlated to the potential gradient and directly correlated to the radial area of the ionization volume and the temporal distribution of the ionizing step, assuming the FES and SES are not overlapping temporally. However, the ions starting closer to A1, which have a longer path and therefore a longer flight time, are also provided with higher kinetic energy. The resulting higher velocity leads to the behaviour that the ToF width is changing along the flight path with a temporal focus at a distance dependent on the potential gradient and the ionization area. When using this ion source at different energies or for different applications this needs to be considered making an optimization of A1 and A2 necessary. A typical achievable ToF spectrum with this laser ion source after optimization is shown in Fig. 13. The set potential values were the same as described above.

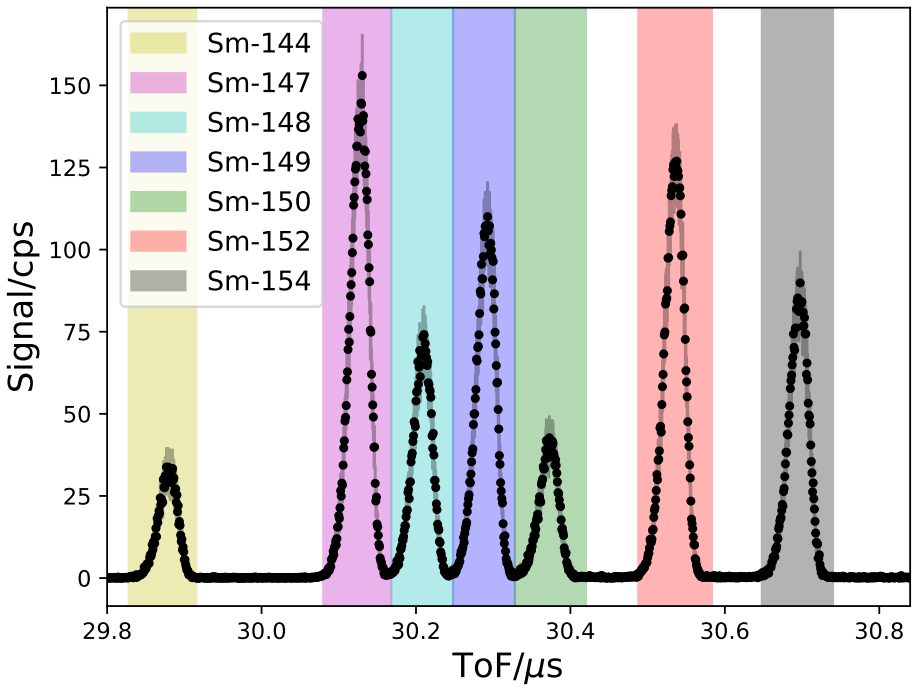

Figure 13: Typical ToF spectrum with the laser ion source using a sample of $^{\text{nat}}$Sm and scanning the FES laser using two step RIS, so that every isotope is visible. This figure was taken from Publication III.

3.5 MR-ToF MS

A **M**ultiple-**R**eflection **T**ime-**o**f-**F**light **M**ass **S**pectrometer (MR-ToF MS) is a device which is used for ToF mass spectrometry utilizing a close-fold trajectory. This is achieved via two stacks of cylindrical electrodes, called mirror electrodes which reflect ions between them using static electric potentials, that need to be tuned to the kinetic energy of the ions. In between the mirror electrodes is a field-free-drift region, in which the ToF separation between species with different mass-to-charge ratios happens. This principle can be seen in Fig. 14. A benefit of the close-fold trajectory is that the

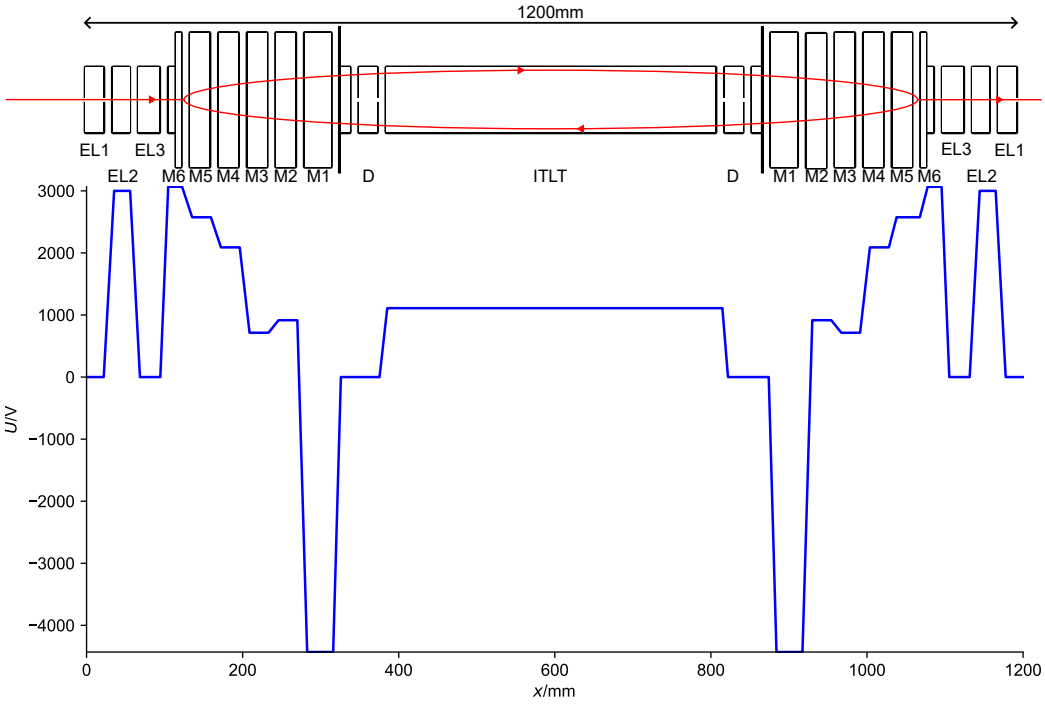

Figure 14: Schematic drawing of the MR-ToF MS and the ToF principle. It consists of an Einzel lens with steerers on both ends (EL1-3), two stacks of 6 mirror electrodes each (M1-6), two deflector electrodes (D) and an in-trap-lift tube (ITLT). A mixed bunch of two ionic species (cyan curve) gets injected from the left side and gets trapped for a number of revolutions. After ejection the species are separated in time of flight (blue and green curves).

system stays compact while the length of the flight path can be extended to multiple kilometers. Due to abberation effects and fluctuations in elec-

trode potentials, the mass resolving power scales linearly with the traveled distance only up to a certain point, reaching saturation eventually at typical values of $R = 100\,000$ to $500\,000$. A drawback of the close-fold trajectory is the potential of different m/q values lapping each other in the setup, leading to unwanted interferences for specific revolution numbers depending on the species to be separated. The design of the MR-ToF MS used in this thesis was a work of Moritz Schlaich and Frank Wienholtz from TU Darmstadt and was acquired in the prospect of Darmstadt's MR-ToF (DA's MR-ToF) collaboration [42]. A schematic drawing of this setup can be found in Fig. 14. This MR-ToF MS is axially symmetric to its center and consists of 4 types of parts: Einzel lenses on both sides, consisting of three electrodes each (EL1-3). EL1 has a cylindrical insert that is cut into four symmetrical pieces, to allow for steering of the ion beam. These einzel lenses are followed by the mirror electrode stack (M1-6). Going further inward, there are deflector electrodes on each side (D), which are cylindrical electrodes cut into four pieces, analog to the steerer in EL1. In the middle of the MR-ToF sits the in-trap lift tube (ITLT), which is a long, hollow, cylindrical electrode. The einzel lens with steerer inset is used to correct trajectory and focus of the incoming beam. The MR-ToF MS performance is heavily dependent on the starting conditions of the ions, which can be summarized by their longitudinal and transversal emittance. The largest emittance that an MR-ToF MS can reliably use is called its acceptance. Since the acceptance is a fixed parameter, that depends on the geometry of the MR-ToF MS and the specific potentials applied to its mirror electrodes, the emittance of the incoming beam has to be matched to the acceptance making bunching and shaping of a beam essential for optimal performance. For a full trajectory correction, meaning a correction of offset from the MR-ToF MS central axis, as well as the incoming angle, two sets of steerers are necessary. Since the MR-ToF MS design only provides one, a second set needs to be installed as a part of the finalized JetRIS system. The potential sets for the mirror electrodes are another important factor for successfully operating an MR-ToF MS. Only very specific potential sets for the mirror electrodes allow for ion trapping, making simulations mandatory for finding those potential sets and making tuning at the setup necessary for optimal performance albeit tedious. Ions that are to be captured need to have a kinetic energy low enough to not be able to surpass the potential barrier of the mirror electrodes, but still need to be able to get into the MR-ToF MS. This can be achieved via a switchable potential on the in-trap lift tube (ITLT). In this scenario ions can get injected

with a kinetic energy sufficient to overcome the potential barrier of the mirror electrodes. The ITLT is set to a positive potential, making it repulsive to incoming cations, slowing them down while entering it. Such an electrode is field-free inside its own volume, with the exception of some field penetration at the cylinder bases. After the incoming ions have been slowed down by the electric field while entering the ITLT its potential can be switched off, leading to a permanent reduction of their kinetic energy, making them unable to surpass the potential barriers provided by the mirror electrode stacks. Through this technique the mean energy of the ion beam can be tuned, making it a less critical parameter for optimization of the ion source. After the ions were trapped for the desired number of revolutions, this process can be applied in reverse to eject the ions out of the system for detection. The MR-ToF MS was characterized and used for ToF-assisted RIS in Publication III. There its future implementation into the JetRIS is outlined, as well as its performance characterized using a self-built laser ion source. The performance was compared to simulations using SIMION 8.1, including performance projections using simulations of a cooler buncher designed by Alexandre Brizard, a joint PhD student between GANIL, France and GSI, Darmstadt. With this work the MR-ToF MS stands now tested and ready for the final integration into the JetRIS setup utilizing the aforementioned cooler buncher.

4 Conclusion and Outlook

In this work laser spectroscopy results on ^{254}No using the JetRIS technique have been achieved in its first successful beamtime [79]. The $^1S_0 \rightarrow {}^1P_1$ transition of ^{254}No at the transition energy of $\nu = 29\,961.480(12)\,\mathrm{cm}^{-1}$ was measured with a resolution of $\Delta\nu = 770(300)\,\mathrm{MHz}$. This was possible by necessary advancements and characterization of the setup to gain a high spectral resolution and sufficient efficiency for on-line measurements. The on-line achieved spectral resolution of 770(300) MHz is a five-fold improvement compared to the previously used RADRIS technique [36]. This value is still limited by saturation broadening. Under offline conditions lower linewidths have been observed using JetRIS as stated below. There is some discrepancy in the determined centroids of the nobelium resonance between both methods which so far remains unsolved. Nonetheless, recently, the same resonance for the nuclear $K = 8^-$-Isomer of ^{254}No mentioned in Publication II has been successfully measured using the JetRIS technique, proving it to be a powerful and reliable method for on-line laser spectroscopy. This experiment would not have been possible with RADRIS due to the transport time of roughly 330 ms, the cyclic collection and measurent procedure [36], with the half-life of said isomer of $T_{\frac{1}{2}} = 265(2)\,\mathrm{ms}$ [82]. The average transport time with JetRIS was determined as 200 ms, making the detection of this short-lived isomer possible. As of now the data analysis for this transition is still ongoing.

The JetRIS setup has been rigorously tested and characterized in off-line experiments. The first part of this was to determine the best achievable spectral resolution, testing different stagnation pressures in the gas cell and background pressures in the jet chamber. This was done via LIF on ^{164}Dy using a $4f^{10}6s^2 \rightarrow 4f^{10}6s6p$ transition at $\lambda = 404.5\,\mathrm{nm}$ resulting in a minimum spectral linewidth of 212(30) MHz. The aforementioned resolution during on-line conditions, which is worse by a factor of 3 to 4, can be explained by the possibility of power broadening. The second part that has been characterized was a part of the efficiency. The total efficiency of JetRIS is put together by the stopping efficiency, the collection efficiency of stopped ions in the gas cell, that are collected on the filament, the laser ionization efficiency, the ion transport efficiency and the detection efficiency. A sum of the collection efficiency and the ion transport efficiency was determined by utilizing a ^{223}Ra recoil ion source, which had a known activity and recoil release rate. The efficiency was measured placing the source at different positions in the

gas cell, showing an efficiency between 1 % and 5 %, with a lower value for a longer travel distance of the ions. The change in measured efficiency is due to the collection efficiency being dependent on the ion starting position. This efficiency, while not optimal, was already sufficient for on-line measurements. The collection efficiency has since been improved by redesigning the filament channel and changing the position of the filament. The online efficiency evaluation can be derived from the dataset of the nobelium nuclear isomer and is done by F. Ivandikov and A. Brizard and beyond the scope of this thesis. The last critical value for the JetRIS performance was the transport time. Even with the recoil ion position at the furthest distance from the nozzle, a full transport time, meaning the time after which all ions, have been either transported or lost, of less than 200 ms was observed, which is an approximate 5-fold improvement over the RADRIS technique, showing the capabilities of JetRIS to access even shorter-lived nuclides of interest.
For future cases a further extension to the JetRIS setup, a MR-ToF MS, has been developed. For its characterization, a laser ion source was built which led to the characterization of its performance with a current mass resolving power of $R = 25000$ with a relative efficiency of 20 %, both acquired after 900 revolutions in the MR-ToF MS. Since the initial number of ions was not known, the countrate in transmission was taken as a reference, meaning 20 % of the ions able to be transported through the system could be trapped for up to 900 revolutions. These results were cross checked with simulations using SIMION 8.0. For coupling with the JetRIS setup well-defined ion bunches are necessary, which can be achieved with an implementation of a cooler buncher. This cooler buncher was designed by A. Brizard during his thesis and the results were used to make compelling predictions of the future performance of the MR-ToF MS. Here, a maximum of $R = 100000$ after 4000 revolutions with a relative efficiency of 80 % is predicted. This would improve the JetRIS measurement capabilities by exchanging an α-decay based detection with a direct ion detection while also maintaining or even gaining efficiency, due to the high detection efficiency of direct ion detection, in contrast to the 50 % for α-detection. With this improvement, the JetRIS setup will be suitable for measuring transitions in every nuclide which is stable or has a half-life of at least 200 ms. It will therefore also improve the analytical capabilities of JetRIS in terms of identification of other, potentially disturbing ionic species, to guide further improvements regarding the gas purity and the applied filament technique. When heating a new filament while using direct ion detection a time and temperature dependent background can be

observed. With the possibilities in ion identification via their mass-to-charge ratio, this can be analyzed, leading to a better understanding of the filament technique. During beamtime it was observed in RADRIS that the filament position, geometry and other not yet known factors exhibit a high influence on setup performance. The dependence on the position and geometry could also be shown in JetRIS by fluid-dynamics simulations done by F. Ivandikov. Gaining a better understanding of the filament technique will be a crucial step for improving both setups in terms of reliability and reproducibility.
With the new self-built laser ion source it was also possible to test the capabilities of ToF-assisted resonant ionization spectroscopy. It was possible to acquire spectra which showed no Lorentzian contribution with a gaussian linewidth of 175(5) MHz with a laser bandwith of 139(13) MHz. This resolution was therefore mainly limited by the laser bandwidth and showing that this source is suitable for measurements with negligible contributions from Doppler broadening, leading to the possibility of achieving natural linewidth for a wide range of transitions. The ToF-assisted spectroscopy was done via developing multiple laser excitation schemes in $^{\mathrm{nat}}$Sm, measuring the isotope shift for every naturally abundant isotope and determining the hyperfine parameter $\mathcal{A}$ for the $I \neq 0$ isotopes. With the input of mean-square nuclear charge radii from literature, the isotope shift could be deconvoluted into the mass shift and the field shift for every transition using a Kingplot analysis. These measurements lay the foundation for future on-line measurements of neutron-deficient samarium isotopes up until the drip line using JetRIS, utilizing fusion-evaporation reactions. For the samarium isotopes from $A = 129$, which is the last one before the dripline to and including $A = 137$, presently no information coming from laser spectroscopy is available [9]. All of these isotopes have a suitable half-life time for JetRIS. The half-life time of ^{130}Sm is still to this day not known reliably with overall information on this isotope being sparse and determined indirectly from the proton decay of ^{131}Eu [83].

5 Publications

5.1 Publication I

The following article 'Resolution Characterizations of JetRIS in Mainz Using ^{164}Dy' was published in *Atoms*, **2022**, *10*, 57. by D. Münzberg et al. This work characterized and compared the achievable spectroscopic resolution of the JetRIS using different nozzles and pressure regimes using LIF on ^{164}Dy utilizing a diode laser and a CMOS camera. This was done with the goal of a resolution of at least 400 MHz for the purpose of resolving hyperfine components in a known transition of ^{253}No. It was found that all three nozzles tested were able to perform within the targeted resolution, if used under the right conditions, with the low-stagnation-pressure nozzle showing the best performance for spectral resolution with a value of 212(35) MHz. With the acquired data the jets were characterized regarding their homogeneity and their mach number.

5.1.1 Author contributions

The author contributed to this work with setting up and executing the measurements as well as data analysis in a joint effort with the co-author J. Lantis. The author was directly involved in every step, including setup of experimental devices and data acquisition and iteratively improving the measurement setup until consistent, reproducible data could be collected. The author is the first author to this article, has written the draft and revised it with the input of the co-authors.

atoms

MDPI

Article

Resolution Characterizations of JetRIS in Mainz Using ^{164}Dy

Danny Münzberg [1,2,3,*], Michael Block [1,2,3], Arno Claessens [4], Rafael Ferrer [4], Mustapha Laatiaoui [3], Jeremy Lantis [3], Steven Nothhelfer [1,2,3], Sebastian Raeder [1,2] and Piet Van Duppen [4]

1 GSI Helmholtzzentrum für Schwerionenforschung GmbH, 64291 Darmstadt, Germany; m.block@gsi.de (M.B.); nothhelfer@uni-mainz.de (S.N.); s.raeder@gsi.de (S.R.)
2 Helmholtz-Institut Mainz, 55099 Mainz, Germany
3 Department Chemie, Johannes Gutenberg-Universität Mainz, 55099 Mainz, Germany; mlaatiao@uni-mainz.de (M.L.); jlantis@uni-mainz.de (J.L.)
4 KU Leuven, Instituut Voor Kern-en Stralingsfysica, B-3001 Leuven, Belgium; arno.claessens@kuleuven.be (A.C.); rafael.ferrer@kuleuven.be (R.F.); piet.vanduppen@kuleuven.be (P.V.D.)
* Correspondence: dmuenzbe@students.uni-mainz.de

Abstract: Laser spectroscopic studies of elements in the heavy actinide and transactinide region help understand the nuclear ground state properties of these heavy systems. Pioneering experiments at GSI, Darmstadt identified the first atomic transitions in the element nobelium. For the purpose of determining nuclear properties in nobelium isotopes with higher precision, a new apparatus for high-resolution laser spectroscopy in a gas-jet called JetRIS is under development. To determine the spectral resolution and the homogeneity of the gas-jet, the laser-induced fluorescence of ^{164}Dy atoms seeded in the jet was studied. Different hypersonic nozzles were investigated for their performance in spectral resolution and efficiency. Under optimal conditions, a spectral linewidth of about 200–250 MHz full width at half maximum and a Mach number of about 7 was achieved, which was evaluated in context of the density profile of the atoms in the gas-jet.

Keywords: JetRIS; fluorescence spectroscopy; gas-jet; de Laval nozzle; nobelium

Citation: Münzberg, D.; Block, M.; Claessens, A.; Ferrer, R.; Laatiaoui, M.; Lantis, J.; Nothhelfer, S.; Raeder, S.; Van Duppen, P. Resolution Characterizations of JetRIS in Mainz Using ^{164}Dy. *Atoms* **2022**, *10*, 57. https://doi.org/10.3390/atoms10020057

Academic Editor: Jean-Christophe Pain

Received: 29 April 2022
Accepted: 25 May 2022
Published: 28 May 2022

1. Introduction

The measurement of atomic transitions via laser spectroscopy is a versatile method for determining fundamental nuclear and atomic properties [1–4]. At the GSI Helmholtzzentrum für Schwerionenforschung, Darmstadt, Germany, laser spectroscopy is used at the Separator for Heavy Ion reaction Products (SHIP) [5,6] with a focus on the heavy actinide and transactinide region [4,7,8]. The low production rates and short half-lives of these nuclides pose difficult experimental challenges and require highly sensitive techniques. Recent laser spectroscopic measurements were conducted successfully at GSI on nobelium isotopes produced through fusion-evaporation reactions at SHIP using the Radiation Detected Resonance Ionization Spectroscopy (RADRIS) technique [7,9], where reaction products are thermalized in an argon filled gas cell and collected on a tantalum filament. The ions are neutralized by collection on a metallic filament, which is subsequently heated to produce an atomic vapor for resonance ionization spectroscopy (RIS). Due to the pressure and temperature conditions in the gas cell, the spectral resolution is limited to about 3 GHz. This is often insufficient to resolve all individual hyperfine components of the studied optical transition, as, e.g., in the case of ^{253}No [10]. Additionally, species with half-lives of less than approximately one second are inaccessible to the RADRIS technique due to decay losses during recoil ion collection. To overcome both of these limitations, JetRIS has been constructed for high-resolution resonance ionization spectroscopy in a hypersonic gas-jet [10]. JetRIS combines the high resolution of the in-gas-jet laser spectroscopy technique developed at KU Leuven [11–13] with the sensitivity of the ion collection and neutral desorption from a heated filament used in the RADRIS technique [14,15]. In the new approach presented here, after neutralization, the atoms are carried through a hypersonic nozzle to form a

low-temperature and low-density gas-jet, reducing the Doppler and collisional broadening effects and thus increasing the spectral resolution by an order of magnitude. The ability to transport neutral species makes it possible to run the system in a continuous mode instead of in cycles as is happening in RADRIS. The negative potential on the filament can be applied at all times in addition to heating, minimizing the before-mentioned decay losses. JetRIS is designed to achieve a spectral resolution of at least 400 MHz for the heaviest elements, allowing for a more precise determination of the nuclear moments. To understand the performance of different nozzles, we present here the characteristics of these in terms of Mach number, spectral resolution and homogeneity of the produced jet.

2. Experimental Procedure

2.1. A Technical Overview of JetRIS

JetRIS consists of a high-pressure gas cell (stagnation pressure P_0 of 80–125 mbar argon) used to stop and thermalize recoil ions from fusion-evaporation reactions after separation from the primary beam by SHIP and a lower pressure jet cell (background pressure P of 5×10^{-3} mbar–2×10^{-2} mbar), which is used for laser spectroscopy. Inside the gas cell, the thermalized ions are transported via an electric field created by a set of cylindrical electrodes toward a filament located at the front of the nozzle, as sketched in Figure 1. This filament, typically made of tantalum, is resistively heated, allowing for neutralization and desorption of atoms, which are subsequently transported by a gas flow into the jet cell through the de Laval nozzle, forming a well-collimated hypersonic gas-jet. This gas-jet features a low temperature and a low pressure, thus reducing the spectral linewidth while the collimation of the gas-jet is crucial to maintain the highest efficiency. Two laser beams are used in a cross-beam geometry to interact with the gas-jet, performing two-step resonance ionization spectroscopy. The laser for the first excitation step is propagating anticollinearly relative to the gas-jet, while the second step proceeds in a perpendicular configuration. While the perpendicular configuration reduces the power density of the laser light, it helps in avoiding ionization in the gas cell. The photo-ions are then guided around a 90° curve via a radio frequency quadrupole (RFQ) to a detector cell, where a channel electron multiplier (CEM) or silicon detector is located. A more detailed description of JetRIS can be found in [10]. In this technique, the nozzle determines the achievable resolution and the total efficiency from the collimation. Therefore, a thorough characterization is essential in understanding the performance of the setup. At KU Leuven, such nozzles are studied in detail using Laser Induced Fluorescence (LIF) in Cu I using pulsed laser radiation as well as the RIS of neutral Cu atoms [16,17].

In this study, we follow a different path by using LIF of neutral ^{164}Dy, which is illuminated by light from a cw-diode laser, propagating anticollinearly to the gas-jet as sketched in Figure 2. With this technique, three different de Laval type nozzles were investigated, and they were designed for different operation pressures and differences in their contour. All of them feature a throat diameter of 1 mm. The first nozzle is intended for usage at low stagnation pressures of P_0 = 80 mbar and a background pressure of $P = 2.5 \times 10^{-2}$ mbar. The diverging part of this nozzle has a length of about 1 cm as sketched in Figure 3. From fluid dynamic calculations, a jet of approximately Mach 8 was expected. The second nozzle is optimized for high stagnation pressures around P_0 = 300 mbar, and here, the diverging part has a length of about 3 cm. This nozzle is identical to the nozzles investigated recently at KU Leuven [16]. The third nozzle, referred to as the mid-range nozzle, has a conic contour. Here, the diverging part has a length of 2 cm. This nozzle was a prototype for operation in an intermediate pressure range while being simple to machine. No simulations were performed to optimize the design of this nozzle, and its optimal operating conditions were not previously known. To seed the atoms into the gas-jet for these tests, the tantalum filament in front of the nozzle was replaced by a tantalum strip that was previously loaded with a sample and resistively heated until a suitable fluorescence signal was observed, but the temperature of the filament was not

measured. It can only be approximated from its color when glowing, with an estimated temperature of 1200 °C.

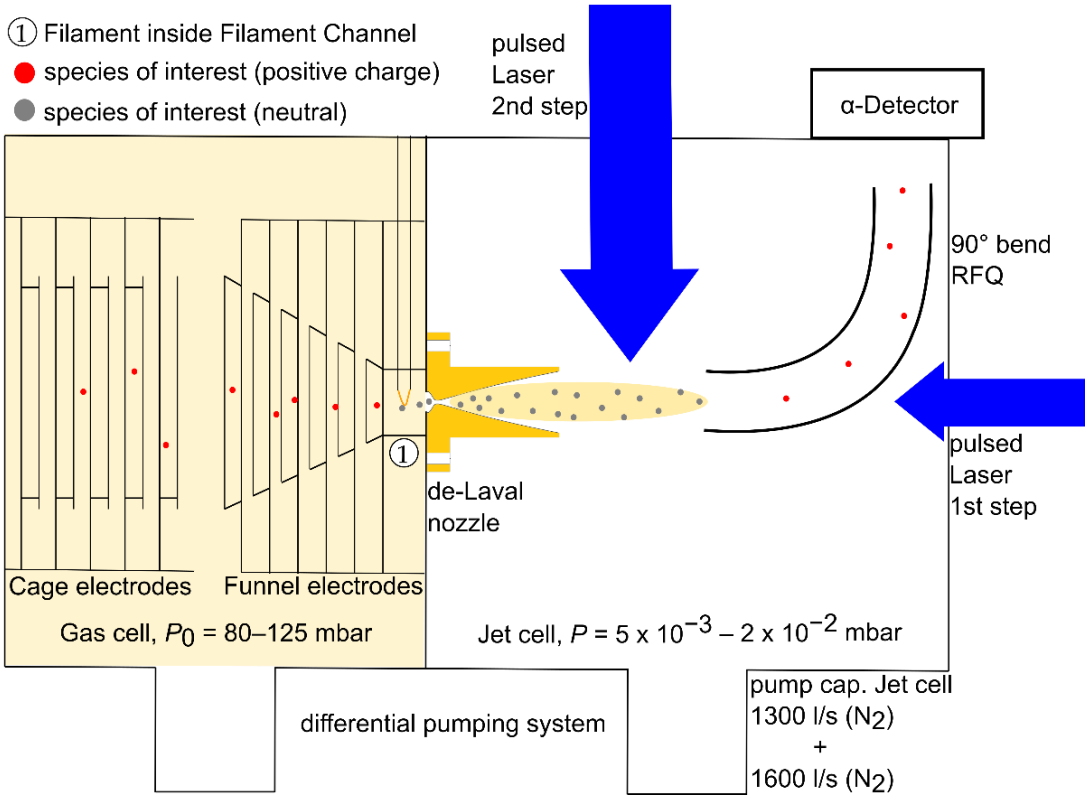

Figure 1. Schematic overview of JetRIS. On the left side are the cage and funnel electrodes. In front of the nozzle, there is a tantalum filament. After being evaporated from the filament, the atoms follow the flow of the buffer gas through the nozzle into the gas-jet. Here, two laser beams used in a cross-beam geometry resonantly ionizes the formerly neutralized species of interest. The ions are guided around a curve via a 90° bend RFQ and collected on an α-Detector.

2.2. Fluorescence Characterization

During the experiments presented in this work, we used one-step laser excitation in contrast to the two-step resonant ionization that will be used in online experiments. As no ions were produced, the RFQ structure was removed (*cf.* Figure 2) and the fluorescence of the seeded atoms provided a way to determine the density and homogeneity along the gas-jet. The atom source was installed next to the nozzle entrance in the gas cell, consisting of a folded piece of tantalum foil, which contained a piece of a few mg of ^{164}Dy with an isotopic purity of about 95%. The usage of an isotopically enriched sample ensured the investigation of a single atomic line as only minor contributions to the fluorescence signal from other isotopes are present and the even-even isotope features no hyperfine structure splitting. The foil was resistively heated with an electric power of 15 W to produce a dysprosium vapor, which was carried to the nozzle by the gas flow. A self-built laser with a 405 nm laser diode (Thorlabs L405P20) in an external cavity in Litrow configuration with approximately 12 mW of laser power and a sub-megahertz linewidth was used to excite the $4f^{10}6s^2 \rightarrow 4f^{10}6s6p$ transition in Dy I at a wavelength of 404.5 nm and with a transition strength of 1.92 $\times$ 10^8 s^{-1} [18]. The laser beam was expanded to form a circle of about 10 mm in diameter and was aligned to propagate anticollinear to the central axis of the gas-jet. A Complementary Metal-Oxide Semiconductor (CMOS) camera (Zelux® CS 165 MU) with a quantum efficiency of 50% was used to capture the fluorescence light originating from the atomic deexcitation. A bandpass filter featuring about 40% transmission at 405 nm

and a bandwith of 10 nm was installed in front of the camera. Pictures of the fluorescence, as shown in Figure 4, were taken as a function of gas pressure, wavelength and exposure time, which did not exceed 26 s due to limitations of the software for the camera.

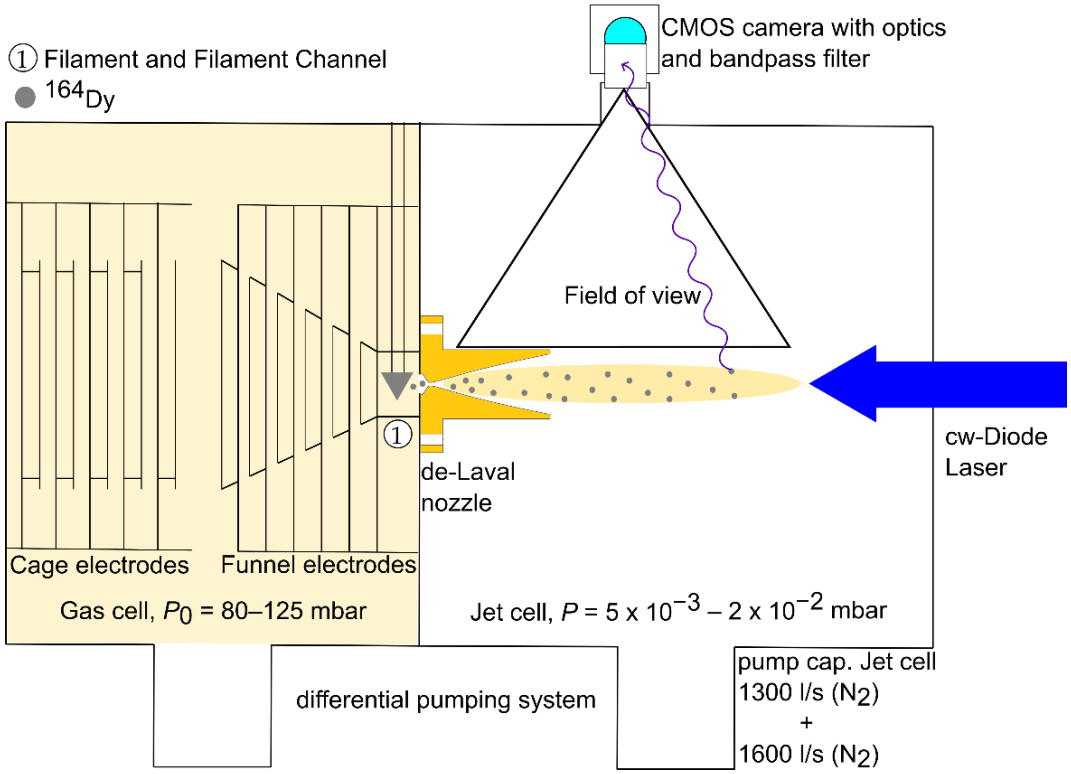

Figure 2. Schematic overview of JetRIS. On the left side are the cage and funnel electrodes, which are necessary for an online experiment but were not in use for the fluorescence measurements. In front of the nozzle, there is a tantalum filament that contains a piece of ^{164}Dy foil. After being evaporated from the filament, the atoms follow the flow of the buffer gas through the nozzle into the gas-jet. Here, a cw-diode laser beam at approximately 405 nm wavelength resonantly excites the dysprosium, and the resulting fluorescence is captured using a CMOS camera. The camera was mounted at a 45° angle relative to the field of view of this schematic.

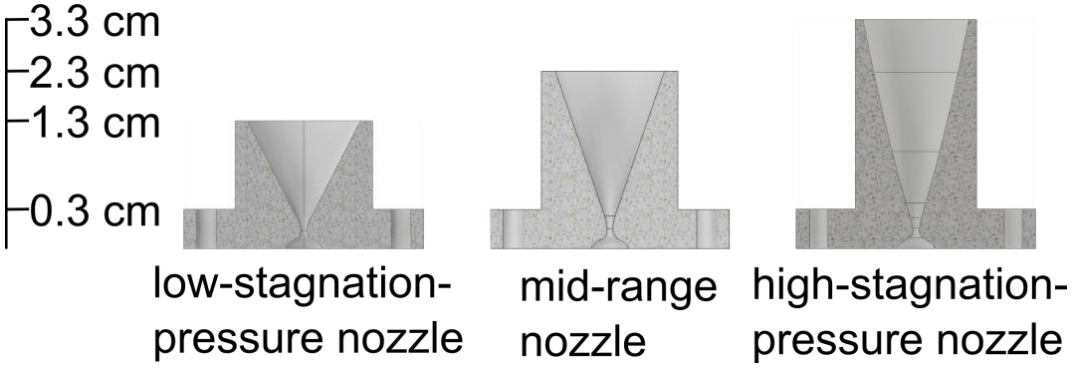

Figure 3. Cross sectional profiles of the characterized nozzles. The base and the diameter of the hole are identical for every nozzle.

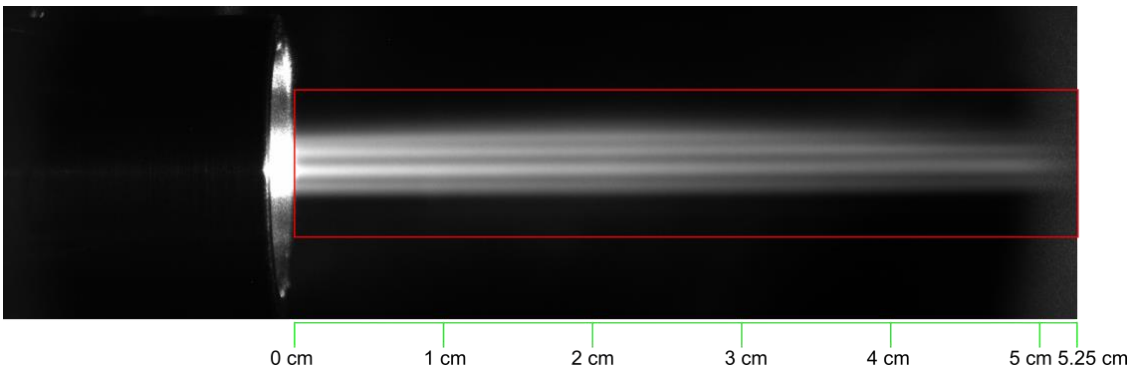

Figure 4. Example picture of the fluorescence acquired with the CMOS camera. Shown is the mid-range nozzle at the centroid frequency of the transition using a stagnation pressure of 100 mbar and a background pressure of 6.47×10^{-3} mbar. The visible stripes in the jet are a property of the laser diode used. The red box indicates the region that was considered in the analysis.

The fluorescence intensity was averaged in the radial plane, normal to the flow direction, in order to obtain information of the performance characteristics along the jet. Due to averaging, the stripes visible in Figure 4 did not disrupt the analysis.

2.3. Characterization of the Gas-Jet

The recorded fluorescence intensity was used to determine the density of atoms in the gas-jet, as well as to study the effective spectral broadening and, thus, the temperature of the jet, while exciting the atoms around the resonance frequency, i.e., performing spectroscopy. The intensity was evaluated pixelwise along the length of the gas-jet with the intensity averaged across the jet for each pixel in x direction. For each pixel, the normalized fluorescence intensity was plotted as a function of the laser frequency. A Gaussian fit to the data provided the centroid frequency and the spectral linewidth of the resonance. A number typically used to describe a gas-jet is the Mach number M, which is defined as the quotient of the stream velocity and the local speed of sound. It gives us an easy-to-compare variable that convolutes the speed of the jet and the temperature. The Mach number M is calculated with the following [11].

$$M = \sqrt{\frac{2}{\gamma - 1}\left(\frac{T_0}{T} - 1\right)}. \tag{1}$$

Here, γ is the ratio of the specific heat capacities of the gas, which is 5/3 for a monoatomic gas, T is the temperature of the jet and T_0 is the initial temperature of the gas before it reaches the nozzle.

The temperature T of the jet was determined from the measured linewidth by using the following relation.

$$\Delta\nu_{\mathrm{D}} = 2\sqrt{\ln(2)}\frac{\nu_{01}}{c}\sqrt{\frac{2kT}{m}}. \tag{2}$$

Here, $\Delta\nu_{\mathrm{D}}$ is the contribution to the full width at half maximum (FWHM) of the Doppler broadening, ν_{01} is the transition frequency, c is the speed of light, k is the Boltzmann constant and m is the mass of ^{164}Dy. As the measured resonance features a Voigt profile, the Doppler broadening can be determined by using the following approximate relation.

$$\Delta\nu = 0.5346\ \Delta\nu_{\mathrm{L}} + \sqrt{0.2166\ \Delta\nu_{\mathrm{L}}{}^2 + \Delta\nu_{\mathrm{D}}{}^2}. \tag{3}$$

Here, $\Delta\nu$ is the FWHM of the measured Voigt profile, and $\Delta\nu_{\mathrm{L}}$ describes the Lorentzian part of the overall resolution, which contains the natural linewidth and the pressure broadening. Any contribution from power broadening is neglected.

To obtain an estimate of the temperature T_0, the connection between T_0 and the stream velocity was used [11].

$$u = \sqrt{\frac{\gamma k T_0 M^2}{m(1 + \left(\frac{\gamma-1}{2}\right)M^2)}}. \quad (4)$$

where m is the mass of the buffer gas, and u is the stream velocity of the jet, which can be obtained from the recorded centroid using the optical Doppler shift from the literature value for the transition of ν_{01} = 24,708.97 cm^{-1} [19]. The stated reference did not mention the isotope of dysprosium for the recorded value. Therefore, the transition was measured with JetRIS by shining a laser beam perpendicular to the flow direction of the gas-jet, which yields a value free from Doppler shift. The measured value was in agreement with the literature value reported in [19].

Above Mach 5, the stream velocity reaches 95% of its maximum. Since the Mach number was expected to be around 5–8, the mean value of these (M = 6.5) was taken as an approximation for T_0. The deviation of the temperatures obtained with M = 5 and M = 8 from the value at M = 6.5 is around 3% and was considered when determining the uncertainty of the experimentally determined Mach number. A typical value of T_0 obtained from the fitting of the data is 380 K, indicating some heating of the gas from the hot filament, a fact that was already observed in previous investigations in Leuven [16].

To determine the quality of the gas-jet, a new metric was established and will be referred to as the homogeneity factor H. The photon density of the fluorescence light was used to evaluate the homogeneity of the sample atom density across the full length of the jet and was compared to a hypothetical, perfectly homogenous jet of constant light intensity. For this new factor, two different integrals have been calculated. A normalized integral of the hypothetical perfect jet $\int I_{\max}$, where the intensity should be constant over the entire length of the jet and the intensity integral over the experimental intensity values $\int I$, resulting in the following equation.

$$H = \frac{\int I}{\int I_{\max}}. \quad (5)$$

The boundaries of both integrals are the same and are determined by the length of the real jet. The homogeneity factor provides a simple value between 0 and 1, where 0 would mean no observed fluorescence, meaning no formation of a jet, and 1 would mean that we would observe a perfectly homogenous jet.

For an overall view on the performance of a nozzle, the spectral resolution and M were multiplied by the relative intensity, summed up and divided by the sum of the relative intensities, therefore making an intensity-weighted average. The uncertainty of these parameters was determined as the standard deviation of the individual numbers.

3. Results

3.1. Resolution

The low-stagnation-pressure nozzle is a de-Laval nozzle and was designed for a stagnation pressure of P_0 = 80 mbar and a background pressure of $P = 2.5 \times 10^{-2}$ mbar [20]. However, while investigating the resolution as a function of the background pressure, as shown in Figure 5a for the low stagnation pressure nozzle, a lower background pressure was found to provide the best resolution. This general trend that the resolution is improving as the background pressure drops was observed for all three nozzles. It has to be noted that the available pressure ranges are limited by the capacity of the JetRIS pumping system. At optimal parameters, the best achievable resolution was 212 $\pm$ 4 MHz for the low-stagnation-pressure nozzle, 239 $\pm$ 13 MHz for the mid-range nozzle and 311 $\pm$ 15 MHz for the high-stagnation-pressure nozzle. These values are all intensity-weighted averages of the individual values for each pixel slice along the gas-jet. It was verified whether analyzing the jet as a whole has an impact on the values relative to the pixel-by-pixel analysis, and

both methods are in agreement with one another. The optimal stagnation pressure of 300 mbar for the high-stagnation-pressure nozzle could not be reached, again limited by the pumping system [16]. Under the available conditions, the low-stagnation-pressure and mid-range nozzle outperformed the high-stagnation-pressure nozzle with regards to the obtained resolution. All of the obtained spectral linewidths are smaller than the stated goal of 400 MHz [10]. The individual parameters for the measurements are summarized in Table 1.

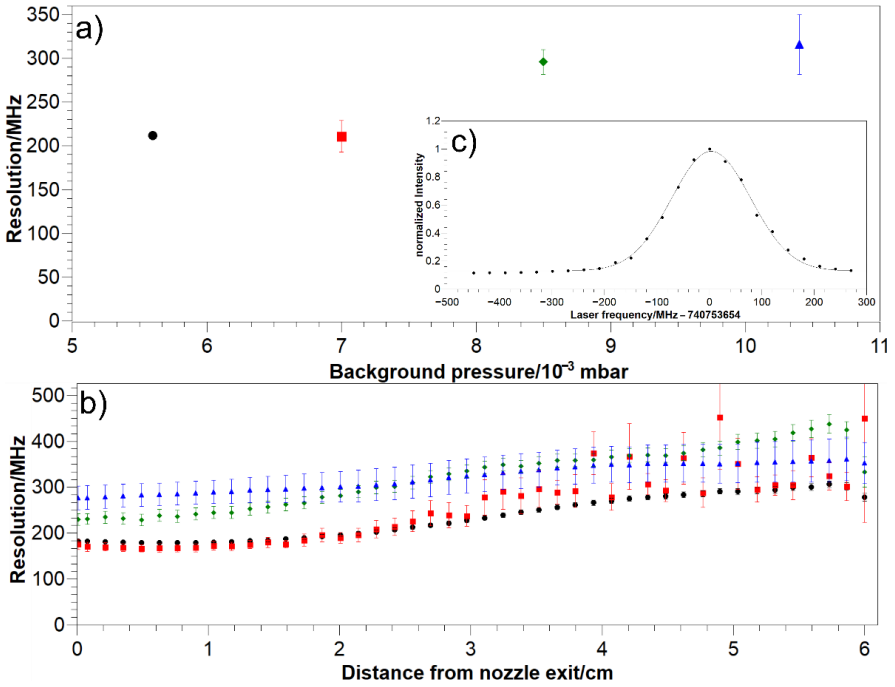

Figure 5. (**a**) Intensity-weighted averages of the resolution for the low-stagnation-pressure nozzle. The resolution generally improves as the background pressure is reduced. (**b**) Resolution along the jet for different parameters of the low-stagnation-pressure nozzle. (**c**) Example Gaussian fit of the intensity as a function of the laser frequency for the low-stagnation-pressure nozzle at P_0 = 80.6 mbar and $P = 5.6 \times 10^{-3}$ mbar. In both pictures, the parameters are as follows: black: P_0 = 80.6 mbar and $P = 5.6 \times 10^{-3}$ mbar; red: P_0 = 80.6 mbar and $P = 7.0 \times 10^{-3}$ mbar; green: P_0 = 80.0 mbar and $P = 8.5 \times 10^{-3}$ mbar; blue: P_0 = 82.2 mbar and $P = 10.4 \times 10^{-3}$ mbar.

Table 1. Intensity weighted averages of M, $\Delta\nu$ and H for the three different nozzles.

Nozzle	P_0/mbar	$P/10^{-3}$ mbar	M	$\Delta\nu$/MHz	H
Low-stagnation-pressure nozzle	80.6	5.6	7.2 ± 1.0	212 ± 30	0.40
	80.6	7.0	7.4 ± 1.0	211 ± 35	0.26
	80.0	8.5	5.0 ± 0.5	296 ± 33	0.43
	82.2	10.4	5.1 ± 0.7	316 ± 45	0.61
Mid-range nozzle	100	6.47	6.7 ± 0.9	250 ± 32	0.60
	125	7.35	7.2 ± 1.0	239 ± 33	0.67
	149	10.0	6.6 ± 0.9	259 ± 33	0.69
High-stagnation-pressure nozzle	125	9.3	4.2 ± 0.5	335 ± 31	0.84
	131	8.5	3.8 ± 0.3	352 ± 30	0.79
	154	12.2	4.6 ± 0.5	311 ± 34	0.78

3.2. Mach Number

The jet was evaluated for its Mach number as described in Section 2.3. For the determination of the gas-jet temperature from the linewidth, the spectral profiles were fitted with Gaussian profiles. The calculated linewidths were taken as the values for the overall resolution, since the fit was in good agreement with the data, as shown in Figure 5c. The natural linewidth can be calculated to be 30.5 MHz from the transition strength. The pressure broadening could not be determined; however, in the case of Cu I studied at Leuven, it was found to be approximately 3 MHz [16]. Power broadening has been neglected due to the low laser power used in the experiment. The two factors were added to a Lorentzian contribution to the linewidth of 33.5 MHz and the temperature-dependent part of the resolution was calculated according to Equation (3). With this, the Mach numbers were calculated as $M = 7.2 \pm 1.0$ for the low-stagnation-pressure nozzle, $M = 7.2 \pm 1.0$ for the mid-range nozzle and $M = 4.6 \pm 0.5$ for the high-stagnation-pressure nozzle in the best case, respectively. The Mach numbers of the high stagnation pressure nozzle are significantly lower than $M = 8$, expected from fluid-dynamics calculations and from observations at KU Leuven [16]. This was most likely due to the fact that the nozzle was used outside of its desired pressure range [21]. In this investigation, some small uncertainties in the evaluation remain, concerning the determination of the stagnation temperature T_0 and the frequency instability of the laser diode while measuring, which are expected to be reflected in the uncertainties. The presented values agree very well with the observations from previous studies at KU Leuven, albeit it has to be noted that the measurements were taken under different conditions. On one hand, the investigations in Leuven for the low-stagnation-pressure nozzle were performed using only the central 1 mm diameter of the gas-jet core with collinear illumination, while in this work the entire jet is illuminated anticollinearly, adding the jet boundary layer of the jet in the evaluation. Furthermore, the ^{164}Dy atoms used in this study are heavier than the ^{65}Cu atoms used in Leuven, which is a much lighter system that is closer to the carrier gas (^{40}Ar).

3.3. Homogeneity Factor

Finally, the homogeneity as defined in Equation (5) was evaluated, which shows a quite different behavior of the nozzles. With the best possible parameters, a value of $H = 0.33$ was achieved for the low-stagnation-pressure nozzle, compared to values of $H = 0.63$ for the mid-range nozzle and $H = 0.76$ for the high-stagnation-pressure nozzle. The corresponding intensity distributions along the jet for the three nozzles are shown in Figure 6.

Clearly, none of the investigated nozzles provide an ideal jet with a perfectly homogenous density profile and some losses from diffusion into the background gas are unavoidable. Furthermore, the intensity profile at the spectral maximum was compared with the intensity profile averaged over the spectral profile. The latter corresponds to the total density of the jet independent of the velocity distribution and shows a better homogeneity. Nevertheless, the profile at the maximum excitation frequency corresponds to the accessible fraction of the density and, thus, provides a better estimate on the expected efficiency. It shall be noted that the pulsed laser for the intended resonant ionization application features a significantly larger bandwidth of about 100 MHz compared to the sub-megahertz bandwidth of the cw diode laser used in this work [22]. This will enable addressing more atoms of the ensemble in the gas-jet and, thus, the effective homogeneity will be in between the two curves in the upper and lower panels of Figure 6, respectively.

The homogeneity factor provides a good impression about the achievable efficiency from the atom density along the gas-jet, but it does not yet provide conclusive information about the overall efficiency of JetRIS. Further measurements are planned, including the transport efficiency of atoms evaporated from the filament and transported through the nozzle to the detector at online-like conditions. For this, a radioactive recoil source will be used, since it releases ions at a known rate, allowing for a quantitative measurement, independent from ionization efficiency when using lasers.

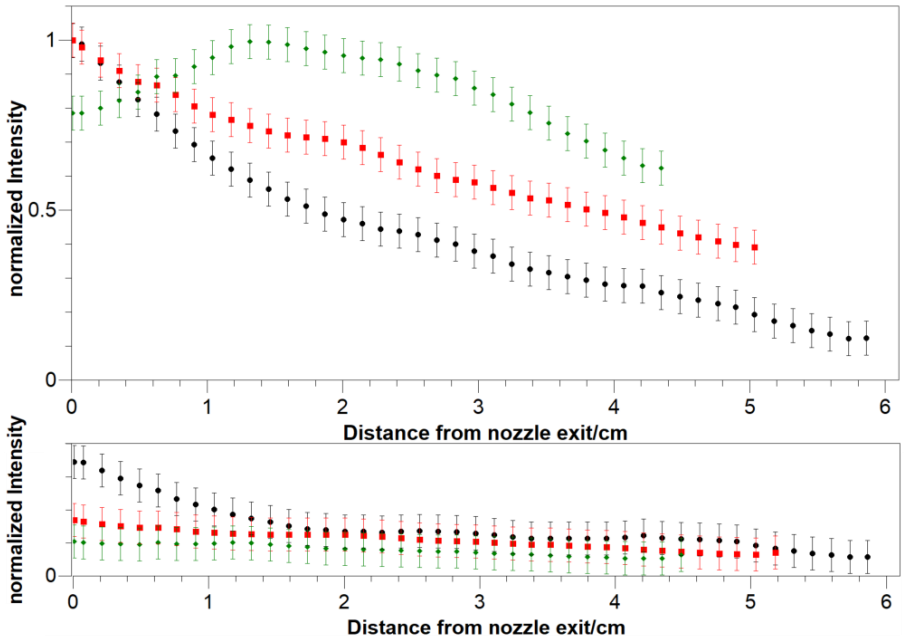

Figure 6. Intensity distribution at the centroid frequency (**upper**) and average over all frequencies (**lower**) for the best parameters of the low-stagnation-pressure nozzle (black, P_0 = 80.6 mbar, $P = 5.6 \times 10^{-3}$ mbar), mid-range nozzle (red, P_0 = 125 mbar, $P = 7.35 \times 10^{-3}$ mbar) and high-stagnation-pressure nozzle (green, P_0 = 125 mbar, $P = 9.3 \times 10^{-3}$ mbar).

4. Summary and Outlook

To enable high-resolution laser spectroscopy of the heaviest elements at GSI, Darmstadt JetRIS is under development. For an online experiment, efficiency is of paramount importance while maintaining a high spectral resolution. Therefore, fluorescence spectroscopy was performed to characterize three hypersonic nozzles in terms of spectral resolution, Mach number and homogeneity. These nozzles were designed for operation at different stagnation pressures. For each nozzle, gas pressures were identified resulting in a resolution sufficient for determining the hyperfine structure of ^{253}No, for example. The highest spectral resolution was found for the low-stagnation-pressure and the mid-range nozzle with linewidths of 211 MHz and 239 MHz, respectively, for the investigated ground-state transition at 404.5 nm in ^{164}Dy. In contrast, the high-stagnation pressure nozzle provided a linewidth of 335 MHz at the intended operation pressures of up to 125 mbar. The larger mass of ^{253}No compared to ^{164}Dy should allow achieving a higher resolution, but since the transition used for nobelium has a wavelength of 333 nm [7] compared to 405 nm for dysprosium, the resolution can be expected to be the similar in both cases. The low- and mid-range nozzle show a similar performance in terms of the Mach number as well. In terms of jet homogeneity, the high-stagnation-pressure nozzle showed the best performance. The mid-range nozzle seems to be the best overall choice, since its resolution and homogeneity are both close to the optimal values found for the other two nozzles. According to investigations at KU Leuven, the high-stagnation pressure nozzle would greatly benefit from operation at a higher stagnation pressure [16]. Nevertheless, our obtained resolution is already close to the value of 170 MHz projected in [16] for laser spectroscopy in the actinide region. Further studies will be performed offline with radioactive sources and resonance ionization spectroscopy to determine the efficiency of JetRIS before measuring online isotopes of nobelium at GSI, Darmstadt.

Author Contributions: R.F. and S.R. conceived the experiment. S.R., D.M., J.L. and S.N. set up the diode laser system. D.M., J.L. and S.N. conducted the measurements. D.M. and J.L. analyzed the data with the input from P.V.D., R.F., M.L., S.R., M.B. and A.C. The paper was written by D.M. with the input from P.V.D., M.B., A.C., R.F., J.L., M.L., S.N. and S.R. All authors have read and agreed to the published version of the manuscript.

Funding: M.L. acknowledges funding from the European Research Council (ERC) under the European Union's Horizon 2020 Research and Innovation Programme (Grant Agreement No. 819957).

Data Availability Statement: The data presented in this study are available upon request from the corresponding author.

Acknowledgments: The authors thankfully acknowledge the LARISSA group (Institut für Physik, Johannes Gutenberg-Universität Mainz) for the contribution of the laser diode cavity, as well as the target lab of GSI, Darmstadt, for the supply of enriched ^{164}Dy.

Conflicts of Interest: The authors declare no conflict of interest.

References

1. Kluge, H.-J.; Nörtershäuser, W. Lasers for nuclear physics. *Spectrochim. Acta B* **2003**, *58*, 1031–1045. [CrossRef]
2. Cheal, B.; Flanagan, K.T. Progress in laser spectroscopy at radioactive ion beam facilities. *J. Phys. G Nucl. Part. Phys.* **2010**, *37*, 113101. [CrossRef]
3. Campbell, P.; Moore, I.; Pearson, M. Laser spectroscopy for nuclear structure physics. *Prog. Part. Nucl. Phys.* **2016**, *86*, 127–180. [CrossRef]
4. Block, M.; Laatiaoui, M.; Raeder, S. Raeder. Recent progress in laser spectroscopy of the actinides. *Prog. Part. Nucl. Phys.* **2021**, *116*, 103834. [CrossRef]
5. Hofmann, S.; Münzenberg, G. The discovery of the heaviest elements. *Rev. Mod. Phys.* **2000**, *72*, 733–767. [CrossRef]
6. Münzenberg, G.; Faust, W.; Hofmann, S.; Armbruster, P.; Güttner, K.; Ewald, H. The velocity filter SHIP, a separator of unslowed heavy ion fusion products. *Nucl. Instrum. Methods* **1979**, *161*, 65–82. [CrossRef]
7. Laatiaoui, M.; Lauth, W.; Backe, W.L.H.; Block, M.; Ackermann, D.; Cheal, B.; Chhetri, P.; Düllmann, C.; Van Duppen, P.; Even, J.; et al. Atom-at-a-time laser resonance ionization spectroscopy of nobelium. *Nature* **2016**, *538*, 495–498. [CrossRef] [PubMed]
8. Backe, H.; Lauth, W.; Block, M.; Laatiaoui, M. Prospects for laser spectroscopy, ion chemistry and measurements of superheavy elements in buffer-gas traps. *Nucl. Phys. A* **2015**, *944*, 492–517. [CrossRef]
9. Lauth, W.; Backe, H.; Dahlinger, M.; Klaft, I.; Schwamb, P.; Schwickert, G.; Trautmann, N.; Othmer, U. Resonance Ionization spectroscopy in a buffer gas cell with radioactive decay detection, demonstrated using ^{208}Tl. *Phys. Rev. Lett.* **1992**, *68*, 1675–1678. [CrossRef] [PubMed]
10. Raeder, S.; Block, M.; Chhetri, P.; Ferrer, R.; Kraemer, S.; Kron, T.; Laatiaoui, M.; Nothhelfer, S.; Schneider, F.; Van Duppen, P.; et al. A gas-jet apparatus for high-resolution laser spectroscopy on the heaviest elements at SHIP. *Nucl. Instrum. Methods Phys. Res. Sect. B Beam Interact. Mater. At.* **2020**, *463*, 272–276. [CrossRef]
11. Kudryavtsev, Y.; Ferrer, R.; Huyse, M.; Bergh, P.V.D.; Van Duppen, P. The in-gas-jet laser ion source: Resonance ionization spectroscopy of radioactive atoms in supersonic gas jets. *Nucl. Instrum. Methods Phys. Res. Sect. B Beam Interact. Mater. B Beam Interact. Mater. At.* **2013**, *297*, 7–22. [CrossRef]
12. Raeder, S.; Bastin, B.; Block, M.; Creemers, P.; Delahaye, P.; Ferrer, R.; Fléchard, X.; Franchoo, S.; Ghys, L.; Gaffney, L.P.; et al. Developments towards in-gas-jet laser spectroscopy studies of actinium isotopes at LISOL. *Nucl. Instrum. Methods Phys. Res. Sect. B Beam Interact. Mater. At.* **2016**, *376*, 382–387. [CrossRef]
13. Ferrer, R.; Barzakh, A.; Bastin, B.; Beerwerth, R.; Block, M.; Creemers, P.; Grawe, H.; de Groote, R.; Delahaye, P.; Fléchard, X.; et al. Towards high- resolution laser ionization spectroscopy of the heaviest elements in supersonic gas jet expansion. *Nat. Commun.* **2017**, *8*, 14520. [CrossRef] [PubMed]
14. Laatiaoui, M.; Backe, H.; Block, M.; Chhetri, P.; Lautenschläger, F.; Lauth, W.; Walther, T. Perspectives for laser spectroscopy of the element nobelium. *Hyperfine Interact* **2013**, *227*, 69–75. [CrossRef]
15. Lautenschläger, F.; Chhetri, P.; Ackermann, D.; Backe, H.; Block, M.; Cheal, B.; Clark, A.; Droese, C.; Ferrer, R.; Giacoppo, F.; et al. Developments for resonance ionization laser spectroscopy of the heaviest elements at SHIP. *Nucl. Instrum. Methods Phys. Res. Sect. B Beam Interact. Mater. At.* **2016**, *383*, 115–122. [CrossRef]
16. Ferrer, R.; Verlinde, M.; Verstraelen, E.; Claessens, A.; Huyse, M.; Kraemer, S.; Kudryavtsev, Y.; Romans, J.; Bergh, P.V.D.; Van Duppen, P.; et al. Hypersonic nozzle for laser-spectroscopy studies at 17 K characterized by resonance-ionization-spectroscopy-based flow mapping. *Phys. Rev. Res.* **2021**, *3*, 043041. [CrossRef]
17. Zadvornaya, A.; Creemers, P.; Dockx, K.; Ferrer, R.; Gaffney, L.P.; Gins, W.; Granados, C.; Huyse, M.; Kudryavtsev, Y.; Laatiaoui, M.; et al. Characterization of Supersonic Gas Jets for High-Resolution Laser Ionization Spectroscopy of Heavy Elements. *Phys. Rev. X* **2018**, *8*, 041008. [CrossRef]

18. Wickliffe, M.; Lawler, J.; Nave, G. Atomic transition probabilities for Dy I and Dy II. *J. Quant. Spectrosc. Radiat. Transf.* **2000**, *66*, 363–404. [CrossRef]
19. Sansonetti, J.E.; Martin, W.C. Handbook of Basic Atomic Spectroscopic Data. *J. Phys. Chem. Ref. Data* **2005**, *34*, 1559–2259. [CrossRef]
20. Roelens, S. Characterization of a Hypersonic Nozzle for Laser Spectroscopy of Singly-Charged Thorium Ions. Master's Thesis, KU Leuven, Leuven, Belgium, 2021.
21. Verstraelen, E. Laser Spectroscopy of Actinides: Octupole Deformation and Gas-Jet Characterization. Ph.D. Thesis, Ku Leuven, Leuven, Belgium, 2021.
22. Verlinde, M.; Ferrer, R.; Claessens, A.; Granados, C.A.; Kraemer, S.; Kudryavtsev, Y.; Li, D.; Bergh, P.V.D.; Van Duppen, P.; Verstraelen, E. Single-longitudinal-mode pumped pulsed-dye amplifier for high-resolution laser spectroscopy. *Rev. Sci. Instrum.* **2020**, *91*, 103002. [CrossRef] [PubMed]

5.2 Publication II

The following article 'In-gas-jet laser spectroscopy of ^{254}No with JetRIS was published in *Physical Review Research*, **6**, 023318 (2024) by J. Lantis et al. It shows a measurement of a $^1S_0 \leftrightarrow ^1P_1$-transition in ^{254}No, which was directly produced via a fusion-evaporation reaction of ^{208}Pb(^{48}Ca, 2n). These results showcase the first successful on-line experiment using the JetRIS. The measured transition was a line previously measured in RADRIS but with an improved sub-GHz linewidth of 770(330) MHz. Unfortunately there are discrepancies between the centroid of this transition form JetRIS and RADRIS which are discussed in the publication to be on the order of 1.6σ, even with a rigorous investigation and analysis of statistical and systematic errors. This paper also highlights the efficiency of JetRIS comparing results from a ^{223}Ra recoil ion source and the on-line nobelium measurements. The efficiency with the ion source lies between 1 and 5% depending on its position inside the gas cell, showing a potential loss channel. The on-line efficiency was investigated as a combination of ionization-, transport- and detection efficiency and was found to be 0.010(3)%. The paper also showcases the transport time measurements for JetRIS using the same recoil ion source showing a collective transport time of less than 200 ms, making the JetRIS a viable technique for short-lived species such as the ^{254}No $K = 8^-$ nuclear isomer with a half-life of 265(2) ms [82].

5.2.1 Author contributions

The author contributed to this work by comissioning and improving the JetRIS in the months before the beamtime, taking part in the efficiency and transport time measurements using the recoil ion source, transport and setup of JetRIS and the laser system at GSI, taking measurements during the beamtime, as well as analyzing parts of the on-line data and conducting measurements for consistency and the evaluation of systematic errors for the wavemeters. All of this was done in tandem with J. Lantis and from beamtime to data evaluation with A. Claessens as well. J. Lantis has written the first draft of the paper, making him the corresponding author, while the first three authors mentioned, J. Lantis, A. Claessens and D. Münzberg are viewed as equally contributing shared main authors of this publication.

In-gas-jet laser spectroscopy of ^{254}No with JetRIS

Jeremy Lantis,[1,2,*] Arno Claessens,[3] Danny Münzberg,[1,2,4] Julian Auler,[1] Michael Block,[1,2,4] Premaditya Chhetri,[3] Christoph E. Düllmann,[1,2,4] Rafael Ferrer,[3] Francesca Giacoppo,[4] Manuel J. Gutiérrez,[2,4] Fedor Ivandikov,[3] Oliver Kaleja,[5] Tom Kieck,[2,4] EunKang Kim,[1] Mustapha Laatiaoui,[1,2,4] Nathalie Lecesne,[6] Vladimir Manea,[7] Steven Nothhelfer,[1,2,4] Sebastian Raeder,[2,4] Jekabs Romans,[3] Elisa Romero-Romero,[1,2] Antoine de Roubin,[3] Hervé Savajols,[6] Simon Sels,[3] Matou Stemmler,[1] Piet Van Duppen,[3] Thomas Walther,[8] Jessica Warbinek,[1,2,4] Klaus Wendt,[1] Alexander Yakushev,[4] and Alexandra Zadvornaya[9]

[1]*Johannes Gutenberg-Universität Mainz, 55099 Mainz, Germany*
[2]*Helmholtz-Institut Mainz, 55099 Mainz, Germany*
[3]*KU Leuven, Instituut voor Kern- en Stralingsfysica, 3001 Leuven, Belgium*
[4]*GSI Helmholtzzentrum für Schwerionenforschung GmbH, 64291 Darmstadt, Germany*
[5]*Universität Greifswald, 17489 Greifswald, Germany*
[6]*GANIL, CEA/DRF-CNRS/IN2P3, 55027 Caen, France*
[7]*Université Paris-Saclay, CNRS/IN2P3, IJCLab, 91405 Orsay, France*
[8]*Technische Universität Darmstadt, Schlossgartenstraße 7, 64291 Darmstadt, Germany*
[9]*II. Physikalisches Institut, Justus-Liebig-Universität Gießen, 35392 Gießen, Germany*

(Received 6 December 2023; accepted 6 May 2024; published 24 June 2024)

Here we report online results with the in-gas-Jet Resonance Ionization Spectroscopy (JetRIS) apparatus. The $^1S_0 \leftrightarrow {}^1P_1$ transition of ^{254}No was successfully measured with sub-GHz resolution, marking a fivefold improvement over previous measurements. Recent developments in laser spectroscopy have allowed access to more exotic nuclei, but measurements of the heavy actinide region have been limited by line broadening mechanisms, limiting the precision with which nuclear properties can be deduced from the hyperfine spectrum. JetRIS provides a method to measure the heavy actinide region with a high level of sensitivity and higher resolution than previous experiments. The offline and online characterizations of the system are reported, and future perspectives are presented.

DOI: 10.1103/PhysRevResearch.6.023318

I. INTRODUCTION

Laser-spectroscopic methods provide a tool to study the fundamental properties of the atom and its nucleus. Atomic transition energies and their strengths can be determined, providing information about the electronic structure, and accurate determination of ionization potentials is possible. Through the interaction between the atomic electrons and the nucleus, information about the spin, size, and deformation of the ground and isomeric nuclear states can be obtained. Independent of nuclear models, these measurements provide information that is essential to understand the structure of the nucleus. A variety of techniques have been developed to study exotic nuclides at a wide range of masses, and this research has been the topic of multiple reviews in recent years [1–5].

Obtaining atomic and nuclear information in the actinide region is crucial for understanding the fundamental principles of nuclear existence, but it is particularly challenging as these nuclides are located at the regions of the largest proton numbers Z. Among the heavy actinides, most nuclides can only be produced in fusion-evaporation reactions, typically at rates of one per second or lower. These low production rates limit vital information about the electronic structure that is generally determined with stable isotopes for lighter elements. Historically, in-gas-cell laser spectroscopy has been the technique of choice to study short-lived isotopes in this region. Pioneering work was performed on the fission isomers of ^{240,242}Am ($Z = 95$) [6] demonstrating the ability to measure species with rates as low as 10 s^{-1}, followed by the first determination of atomic levels in Fm ($Z = 100$) [7]. More recent examples include the measurement of the chain of $^{212-215}$Ac [8], which revealed the influence of the unpaired $\pi h_{9/2}$ proton on the nuclear structure of the region. Even with these developments, the *trans*-fermium region remained out of reach for existing in-gas-cell laser spectroscopy facilities until advances were made using the RAdioactive Decay detected Resonance Ionization Spectroscopy technique [9,10,12]. The RADRIS technique was used to determine the first atomic transition in No ($Z = 102$) [11], providing an avenue to probe relativistic effects in the atomic structure of this region.

*Present address: Physics Division, Argonne National Laboratory, Lemont, IL 60439, USA.

Further experiments provided the first precision measurement of the ionization potential of nobelium [14], and determination of the ground-state nuclear properties of a chain of nobelium isotopes [13].

Although highly sensitive, the RADRIS technique has limitations that restrict the elements and isotopes that can be studied. One limiting factor is the lifetime of the species of interest, as time-consuming steps between the collection and subsequent measurement reduce the overall efficiency of the technique for short-lived isotopes ($T_{1/2} < 1$ s). Recent work has been performed to minimize these delays, as described in Ref. [15]. The second limiting factor, and the focus of this work, is the achievable spectral resolution. As in-gas-cell laser spectroscopy is performed in a high-pressure environment at room temperature, pressure and Doppler broadening of the spectral lines lead to a spectral resolution of about 4 GHz, in turn limiting access to nuclear properties and the precision with which they can be extracted from hyperfine spectra.

Developments at the Leuven Isotope Separator On Line (LISOL) facility resulted in the first online experiment of laser spectroscopy in a supersonic gas jet [16–18]. The supersonic gas-jet was formed using a convergent-divergent (de Laval) nozzle, where the gas traveling through the nozzle progresses from subsonic velocities to supersonic as the gas expands in the downstream divergent section of the nozzle. The gas moves uniformly in the jet and can be characterized by the Mach number (M), defined as the ratio of the stream velocity (u) to the local speed of sound (a), which are dependent on the choice of buffer gas and the conditions in the gas cell, as can be seen in Eqs. (1) and (2) below,

$$a = \sqrt{\frac{\gamma k T}{m}}, \tag{1}$$

$$u = \sqrt{\frac{\gamma k T_0 M^2}{m\left(1 + \left[\frac{\gamma-1}{2}\right]M^2\right)}}, \tag{2}$$

where γ is the adiabatic index, or the ratio of the heat capacity at constant pressure to heat capacity at constant volume, of the buffer gas, and is equal to 5/3 for monatomic gases like argon. k is the Boltzmann constant, m is the mass of the buffer gas atom, T is the temperature in the gas jet, and T_0 is the stagnation temperature, or the temperature of the buffer gas in the cell before expansion. As the Mach number increases, it quickly and asymptotically approaches a maximum stream velocity, approximately 558 m/s in the case of argon, as the local speed of sound continues to drop. The temperature and density of the gas-jet are inversely related to the square of the Mach number, as can be seen in Eqs. (3) and (4),

$$T = \frac{T_0}{1 + \left[\frac{\gamma-1}{2}\right]M^2}, \tag{3}$$

$$P = P_0\left(1 + \frac{\gamma - 1}{2}M^2\right)^{\frac{-\gamma}{\gamma-1}}. \tag{4}$$

At $M = 7$, the temperature in the gas-jet is reduced to 17 K and the pressure and density reach 5% of the stagnation conditions. This large reduction allows for a large gain in the spectral resolution over the in-gas-cell laser spectroscopy method, where Doppler and pressure broadening effects dominate the spectral line shape. Critically the developments at the LISOL facility demonstrated that the in-gas-jet laser spectroscopy technique could maintain the total efficiency of the in-gas-cell method while achieving an order of magnitude improvement in the spectral resolution. This presents in-gas-jet laser spectroscopy as a powerful tool for studying rare nuclei with production rates that prevent their study by other techniques such as collinear laser spectroscopy.

The concept of the JetRIS apparatus was introduced in Ref. [19] as a method to study the heaviest elements with the in-gas-jet laser spectroscopy method. JetRIS combines the use of filament neutralization from RADRIS with the in-gas-jet ionization technique to achieve both a high efficiency and high spectral resolution. This article presents the status of the JetRIS apparatus, including offline studies for characterization, online results, and the outlook for future measurements. These comprise the design and characterization of a hypersonic nozzle by resonance ionization spectroscopy flow mapping of copper isotopes seeded in an argon gas jet, and by laser-induced fluorescence measurements of stable dysprosium samples [20]. Radioactive recoil-ion sources were also used to determine the overall efficiency of the system. These offline measurements resulted in improvements in performance that allowed successful laser spectroscopy measurements of ^{254}No.

II. EXPERIMENT

A. JetRIS apparatus

The concept of the JetRIS apparatus was presented in Ref. [19]. Here we briefly repeat its concept and main characteristics. The JetRIS apparatus consists of three sections, shown in schematic form in Fig. 1. First, an argon gas cell (80 mbar) is used to thermalize reaction products for online experiments, or as a cell for the production of atoms and ions from offline sources. In online experiments, the isotopes of interest are produced through fusion-evaporation reactions, with the separator for heavy ion products (SHIP) [21,22] used to separate the primary beam from the reaction products. Within the gas cell, a series of dc electrodes is used to guide ions to a thin tantalum filament that is biased to a negative potential. The ions are collected and neutralized on the filament. The ions first are transported through a cylindric electrode structure (dc cage with a field gradient of about 4.2 V/cm) leading to a second set of concentric electrodes with decreasing diameter (dc funnel with a field gradient of 18.5 V/cm) to efficiently guide the ions to the filament, which was held at a potential of −150 V. The filament is resistively heated, producing an atomic vapor that is carried by the laminar flow of the argon buffer gas through a de Laval nozzle into a lower pressure (7×10^{-3} mbar) jet chamber, where the expanding gas forms a collimated, low-temperature rarefied gas jet (see Sec. II B). After laser resonant ionization within the gas jet, the resulting photo ions enter a 90° bent radiofrequency quadrupole (RFQ) ion guide, where they are separated from the remaining atoms and transported through a differential pumping barrier to the detector. Detection can be performed with either a light-insensitive silicon detector for online measurements, as discussed later in Sec. II D, or a channel electron multiplier detector for ion detection of stable isotopes.

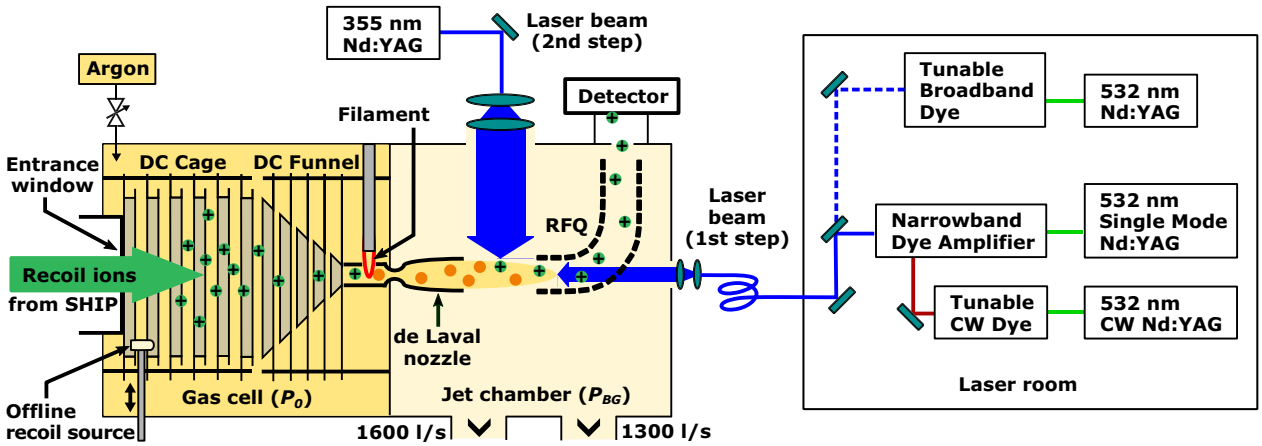

FIG. 1. Schematic layout of the JetRIS apparatus. An 80-mbar high-pressure gas cell is used to thermalize fusion-evaporation reaction products from SHIP, which are transported to and adsorbed onto a heated filament and neutralized for subsequent laser ionization spectroscopy measurements in a gas jet.

B. Hypersonic low-P_0 de Laval nozzle

The in-gas-jet laser ionization and spectroscopy technique relies on a convergent-divergent (de Laval) nozzle to deliver a gas jet with a high Mach number M (i.e., low temperature T) and high flow uniformity (i.e., jet collimation). These properties depend critically on the stagnation pressure P_0 inside the JetRIS gas cell and the background pressure P_{BG} of the environment where the jet forms, referred to henceforth as the jet chamber. A previous design operated at high stagnation pressures ($P_0 = 300$ mbar), suited for gas cells relying on only-gas-flow transportation, was reported in [23] and provided a cold (17 K), highly collimated, and uniform gas jet with a Mach number of 8.1 and a length of 62 mm. For this high-P_0 nozzle it was observed that below a stagnation pressure of 100 mbar the jet formation was inhibited due to a significant thickening of the boundary layer on the nozzle walls [24]. Following the same design prospects, a de Laval nozzle, operational at lower stagnation conditions ($P_0 \leqslant 100$ mbar) and suited for gas cell ion transport using dc fields, was developed for JetRIS.

Contour design and computational fluid dynamics (CFD) calculations of the low P_0 nozzle were performed at the Von Karman Institute for Fluid Dynamics (VKI), Sint-Genesius-Rode, Belgium. Starting from the same inviscid contour as the high-P_0 nozzle, a viscous correction based on the JetRIS operating conditions was applied leading to three significant adjustments. The throat diameter was slightly increased from 1.029 to 1.067 mm for a higher mass flow. The opening angle of the diverging nozzle part was increased from $\omega = 16.6^\circ$ to 28.2°, and the nozzle was shortened from 37.5 to 18.0 mm.

According to the numerical calculations, this design results in the formation of a 60-mm-long gas jet with a core diameter of about 5 mm (cf. Fig. 2), but the simulations also indicate that the hypersonic gas jet is highly sensitive to weak variations in the background pressure. Finally, two low-P_0 nozzles were CNC-machined out of brass (MS58) to within a contour error of less than 5 µm and a surface roughness of 0.1 µm. The nozzle as well as the contour deviation of the divergent nozzle part are shown in Fig. 3. The surface roughness was measured at three different positions by first casting a negative replica and then measuring with an optical profilometer (Sensofar Neox). For all three points, roughness is found to be between 90 and 110 nm. Initial characterization measurements to gauge the gas jet properties were performed at the IGLIS laboratory [16] at KU Leuven using

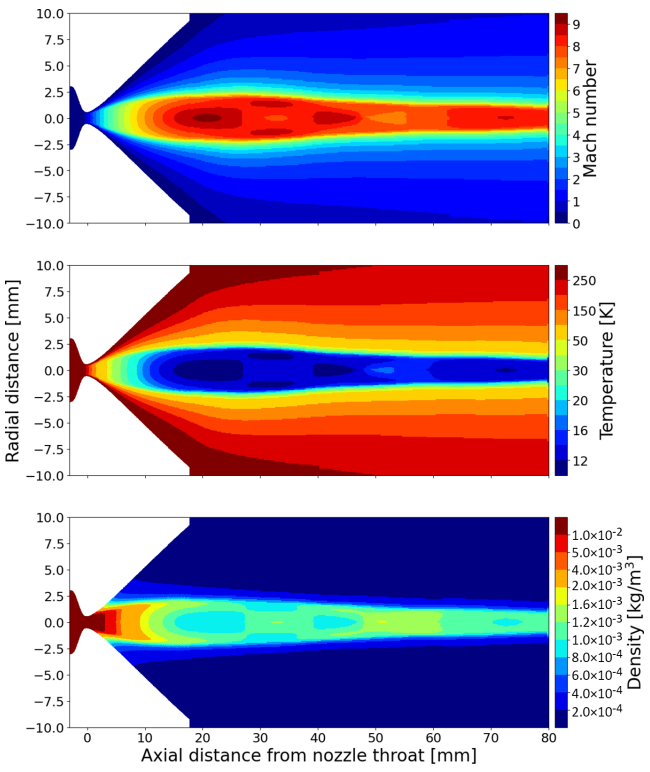

FIG. 2. 2D plot of the Mach number, temperature, and mass density distributions as calculated by the VKI HYPNOZE design code. The pumping capacity of JetRIS allows only for nozzle throat diameters of about 1 mm using stagnation conditions of $P_0 = 80$ mbar and $T_0 = 300$ K.

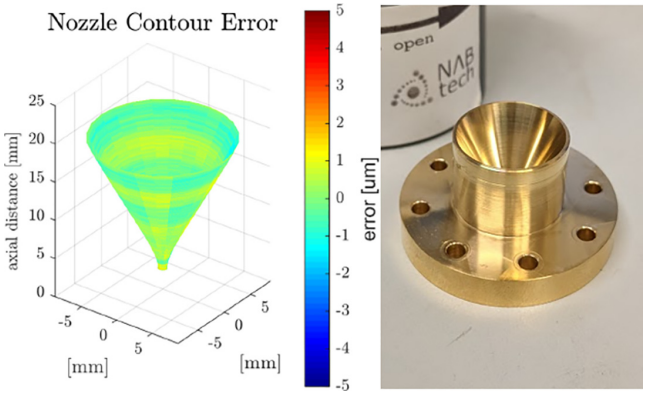

FIG. 3. Picture of the brass low-P_0 nozzle (right) with a 3D-visualization of the contour error (left). The error is the contour deviation between machined and calculated contour and is measured with a Werth HA 400 CMM machine in combination with a Fiber-Probe for more than 55 000 points.

planar laser-induced fluorescence (PLIF) measurements [25] on ^{63}Cu. Surprisingly, a poor flow uniformity was observed at the designed background pressure of 2.5×10^{-2} mbar. Lowering the background pressure hinted towards an improved uniformity, but this could not be ascertained by PLIF. These investigations were complemented by PLIF measurements of ^{164}Dy using the second contoured nozzle, for which the results are discussed in [20]. To address the uncertainty in the uniformity of the gas jet, additional characterization was performed using resonance ionization spectroscopy (RIS) flow mapping at the gas-jet core with ^{63}Cu, as described in [23]. RIS flow mapping is achieved by high-resolution laser spectroscopy where a narrowband scanning laser is aligned along the axis of the gas jet, and the ionization laser is aligned in a transverse manner, such that photoions are only produced in the well-defined region where the lasers overlap. The ionization laser was moved to across the gas jet, allowing regions to be investigated separately. A partial scan of the hyperfine structure (the low-energy doublet) of ^{63}Cu was then measured and the spectra were fitted using χ^2 minimization of a Voigt profile containing two peaks. The Doppler shift of the centroid and the Gaussian width at half-maximum of the peaks are extracted from the spectra, from which the stagnation temperature of the gas inside the gas cell T_0 and the local gas jet temperature T are determined. These measurements were conducted at four different background pressures starting from the designed conditions (2.5×10^{-2} mbar) to the lowest achievable pressure (5.9×10^{-3} mbar) in order to obtain the ideal flow match conditions. The resulting Mach numbers and densities are shown in Fig. 4.

A significant deviation is found between the calculated behavior of the Mach number and the RIS flow mapping results. A high-Mach-number core was observed in the gas jet with flow-matching conditions at much lower background pressures than initially anticipated, with a background pressure of 7×10^{-3} mbar, and subsequently the operational vacuum conditions for our measurements were fixed to this value.

The need for a lower background pressure to obtain a homogeneous gas jet with a high Mach number points to an

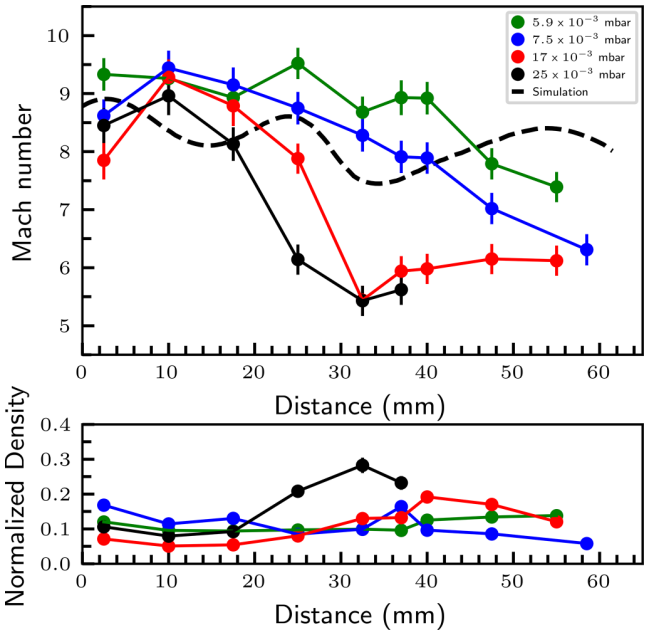

FIG. 4. The measured Mach number distribution (top) and density distribution (bottom) along the jet core for $P_0 = 80$ mbar and different background pressures. The calculated Mach number along the gas jet is shown as a dashed line.

overestimation of the static pressure (the pressure inside the jet) in the CFD calculations. A mismatch in static pressure at the exit plane (P_E) and background pressure leads to a radial velocity component after crossing the nozzle exit plane, resulting in expansion-contraction cycles in the gas jet that inhibit proper jet formation. The boundary layer between the nozzle and jet core is of critical importance in hypersonic flow, and disturbances here propagate through the entire core. Due to the large mean free path in rarefied gasses, it is possible that the boundary condition of $v = 0$ is no longer met. The resulting slip flow regime leads to higher average velocities in the boundary layer, reducing the exit static pressure (P_e). This deviation from the Navier-Stokes equation is not accounted for in the CFD calculations.

C. Online laser system

The in-gas-jet method requires a state-of-the-art laser system to provide high power and short (∼10 ns) pulses at a high-repetition rate to maximize the laser ionization efficiency, while also providing narrow-bandwidth light for high-resolution laser spectroscopy in the cold gas jet. A pulse repetition rate of 15 kHz is ideal to irradiate every atom at least once within the first 40 mm of the gas jet, as the flow velocity is about 550 ms^{-1} at $T_0 = 300$ K.

As a two-step ionization scheme was used, multiple lasers were used in this experiment. These can be grouped into a narrowband and a broadband system. A schematic drawing of the systems can be seen in Fig. 1. The narrowband laser system is comprised of a pulse dye amplifier system (PDA) seeded by a tunable, single-mode continuous-wave (CW) dye laser, which was used for the first excitation step, and the direct light from a high-power Nd:YAG laser provided

the nonresonant ionization step. To maximize ionization efficiency in these experiments, the scanning laser should have sufficient bandwidth to cover the full thermal distribution of nobelium atoms in the gas jet. For this particular nozzle, this would imply a bandwidth of 160 MHz ($T_0 = 330$ K). The two-stage PDA is seeded by a wavelength tunable CW dye laser (Matisse, Sirah Lasertechnik) and optically pumped by a state-of-the-art single longitudinal mode Nd:YAG laser (Edgewave, PXn300-2-GF-SLM). This laser can provide up to 60 W of 532 nm light in Fourier-limited pulses of about 8 ns at repetition rates of 15 kHz. Single-mode operation of the laser was used to avoid resonances caused by additional modes that are typically present in high-repetition-rate PDA pumped Nd:YAG lasers [26]. The resulting pulses from the PDA when equipped with the laser dye 4-Dicyanomethylene-2-methyl-6-p-dimethylaminostyryl-4H-pyran (DCM) in a mixture of dimethyl sulfoxide (DMSO) and ethanol (75% and 25%) give a pulse width of about 4.5 ns and a bandwidth of 95 MHz in fundamental light. By frequency doubling with a single-pass second-harmonic generation (SHG) unit using a β-barium borate (BBO) crystal, the pulses are shortened to about 3 ns resulting in a spectral bandwidth of 150 MHz. A detailed characterization of the narrowband PDA using a prototype Nd:YAG at repetition rates of 10 kHz is reported in Ref. [26].

In addition, a broadband laser system was used during preparatory online studies using ^{155}Yb to ensure gas jet formation and good operation of the JetRIS apparatus. The laser light for the first excitation step was produced with a pulsed dye laser (Sirah Lasertechnik, Credo) pumped by a multimode Nd:YAG laser (Edgewave, InnoSlab IS400-2-L) for which the repetition rate is limited to 10 kHz and the bandwidth is limited by the laser grating to approximately 1.8 GHz.

The ionization step of both laser schemes was realized with the third harmonic of a high-power Nd:YAG laser (Edgewave, InnoSlab IS400-2-L) operated at 10 or 15 kHz for ytterbium or nobelium ionization, providing up to 30 W of UV light.

D. Detector setup

In the online operation of the JetRIS setup, different radioactive isotopes are distinguished by measuring their specific α-decay energy. The decay was measured with a light-insensitive silicon (Mirion PIPS®) detector in an independently-pumped vacuum chamber, separated from the jet chamber by a 2.6-mm-diam pinhole to maintain ultrahigh vacuum. This allows the detector to be set on a potential of -2 kV relative to the nozzle. The acceleration of the ions causes them to be implanted a few nm into the protective layer of the detector and prevents volatile species from desorbing from the surface before decay.

A schematic of the electronics used for the detector is shown in Fig. 5. To maintain a low noise and high resolution α-energy measurement while on high voltage, the -2 kV potential was applied to the entire signal processing chain. The measurement system consists of the previously mentioned silicon detector with 600 mm^2 sensitive surface area, 40 V detector-bias power supply, a preamplifier, and a Red-Pitaya STEMlab 125-14 for digitization. The different supply voltages were generated by a self-designed small-form-factor toroidal transformer to protect the measurement electronics

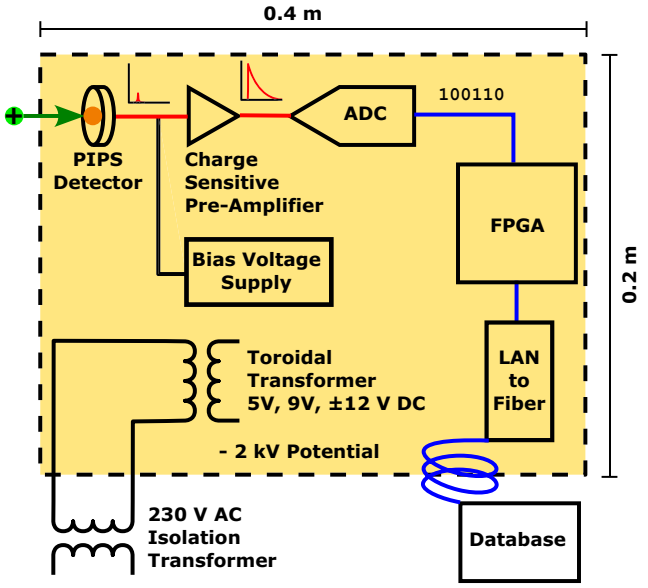

FIG. 5. Schematic of the detector setup to measure the characteristic α-decay of volatile recoil ions. The details are described in the text.

from high-frequency noise of switching power supplies. An isolating transformer was used to decouple the main voltage from the ground potential, and a LAN-to-fiber converter was used to write the single-event decay energy with an 8 ns precision time stamp to a database. Correlation of the measured decays to the laser wavelength was done with the time stamp.

The detector was used through the online experiment to identify various nuclei produced in the production and decay chains of ^{155}Yb, ^{254}No, as well as ^{219}Ra emitted from a recoil source of ^{223}Ra, with a resolution of approximately 80 keV; cf. Fig. 6.

III. OFFLINE CHARACTERIZATION

Characterization of the JetRIS apparatus in offline measurements was carried out to optimize its operation. Offline measurements were performed with radioactive ^{223}Ra recoil sources to characterize the transport of ions through JetRIS, similar to the studies for the cryogenic gas cell used at SHIPTRAP [27]. The overall transport efficiency and speed were measured using these methods.

A. Transport efficiency

The transport efficiency from the gas stopping cell to the detector was investigated as one component of the overall efficiency. A recoil ion source was mounted on a movable rod within the gas cell, and the transport efficiency was determined through the ratio of α-decays detected in the PIPS detector to the known rate of daughter nuclei emitted from the source. Two short-lived species can be observed in the ^{223}Ra decay chain, ^{219}Rn ($t_{\frac{1}{2}} = 3.94$ s) itself as well as ^{215}Po ($t_{\frac{1}{2}} = 1.78$ ms), and the overall transport efficiency was calculated from the observed decays of both species. Based on the geometry of the detector, it was assumed that the detection

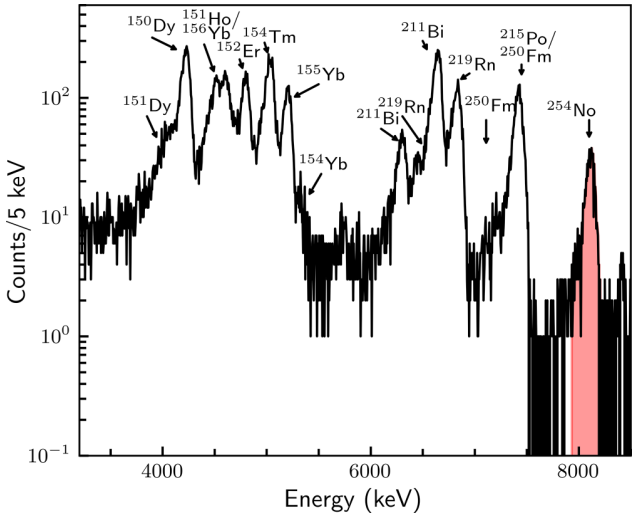

FIG. 6. Alpha spectrum of the nuclei observed during the online experiment using the silicon detector at high voltage as described in the text. The decay chains of ^{155}Yb, ^{254}No, and ^{223}Ra are shown. The red shading indicates the energy gate used for cutting the data on ^{254}No.

efficiency of the implanted recoil ions was 50% with a further 50% reduction in the detected ^{215}Po from recoiled ions leaving the surface of the detector. The rate of recoils from the source was determined by measuring the activity in vacuum with the source positioned at different distances from the detector. The transport efficiency of the ions as a function of distance from the nozzle is shown in Fig. 7.

The source was mounted to a thin tantalum disk used to shield the recoils from the grounded rear flange of the gas cell. The potential of the recoil source and the disk was matched to the potentials applied to the surrounding electrodes. A sharp

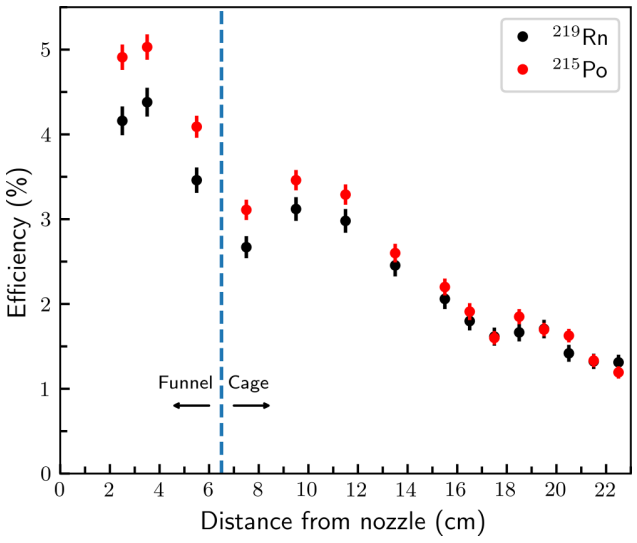

FIG. 7. Offline transport efficiency of the ^{219}Rn and ^{215}Po daughters of a ^{223}Ra recoil source as a function of source distance from the nozzle. The recoil source was mounted on an adjustable rod following the central axis of the JetRIS gas cell.

decrease in transport efficiency was observed when varying the applied voltage away from the local potential. The recoil source was moved along the central axis of the gas cell, providing a map of the transport efficiency for ions that were stopped in different regions of the gas cell. The transport efficiency fell as the recoil source was pulled farther from the de Laval nozzle, as shown in Fig. 7, indicating that significant losses occur in the transport through the cell.

The initial design of JetRIS featured a gas cell pressure of 30 mbar. Simulations of the distribution of heavy ions in the gas cell at 30 mbar were performed and described in [19]. The most probable stopping distance was located 21 cm from the nozzle. As the gas cell was operated at a higher pressure of 80 mbar during these measurements, it is assumed that the actual stopping distance was located further from the nozzle. Comparing the simulated most probable stopping distance to the measured transport efficiency along the central axis, a transport efficiency of approximately 1.5% can be expected for online measurements.

It should be noted that most transport losses occur within the gas cell, including the transport through the nozzle. The transport efficiencies through the bent RFQ and into the detector cell were investigated by measuring the current of photoions in an offline setting. Here, the investigated electrode was negatively biased by a battery box with 45 V, while the positive terminal was connected to a picoamperemeter (Keithley 6485). A natural ytterbium atom source was resistively heated next to the nozzle, producing a vapor. Two lasers propagating through the nozzle were used to resonantly ionize the atoms, which were carried into the gas jet and to the bent RFQ. Ions impinging on the RFQ rods, connected to the picoamperemeter, led to a measurable current of 20 pA. Afterwards the negative terminal was connected to both transport electrodes inside the detector cell and the measurement was repeated. In this configuration, a current of 15 pA was measured. As a result, a transport efficiency through the bent RFQ and the differential pumping barrier to the detector chamber of 75% was derived.

B. Transport time

Furthermore, the recoil ion source was used to investigate the transport time of ions through the JetRIS apparatus. Cyclic measurements were performed with a period of 500 ms. The floating potential used to prevent the recoil daughters from being attracted back to the source after thermalization and the RF frequency applied to the ion guide to transport ions from the jet to the detection region were pulsed for a short duration (50 ms) with a variable time delay, ΔT, between the pulses. Ions that did not travel from the source to the bent RFQ within this time delay would not be transported to the detector. The count rate as a function of the delay between the pulses of the floating potential and the RFQ was measured and fit to a Gaussian function to determine the mean transport time at different distances from the nozzle in the gas cell, as can be seen in Fig. 8.

Even at the furthest distance of 22.5 cm, a transport time of less than 200 ms was observed. This short time provides access to short-lived species that are currently out of reach for measurements with the RADRIS technique, which even

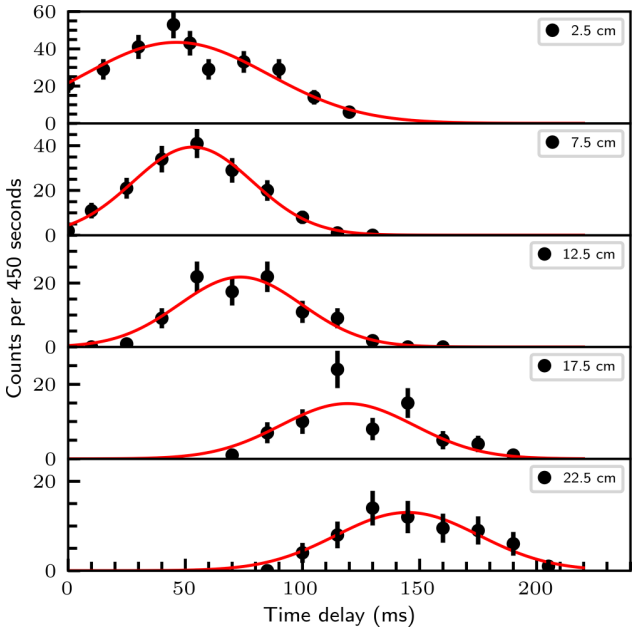

FIG. 8. Effective transport time of recoil ions from the JetRIS gas cell to the detector as a function of distance from the nozzle. The time delay shown is the difference in the rising edges of the potential pulses applied to the recoil source and the bent RFQ.

with recent advancements is limited to species with lifetimes greater than approximately 500 ms [15]. Additionally, a plateau in the transport time was observed as the recoil source approached the nozzle, towards a minimum of approximately 50 ms. Further work is being performed to understand this transport in order to improve the efficiency and to minimize decay losses during transport.

IV. ONLINE EXPERIMENT

The first online experiment using the JetRIS apparatus was performed at the GSI Helmholtzzentrum für Schwerionenforschung in Darmstadt, Germany, targeting ^{254}No and ^{155}Yb. ^{254}No ions were produced through the ^{208}Pb(^{48}Ca, 2n)^{254}No fusion-evaporation reaction, with a cross section of 2 μb [28] at a beam energy of approximately 217 MeV, and ^{155}Yb ions were produced through the ^{112}Sn(^{48}Ca, 2n)^{155}Yb reaction, with a cross section of 7.5 mb [12] at a beam energy of approximately 218 MeV. A beam of ^{48}Ca was accelerated using the UNILAC linear accelerator with average beam currents of up to 0.7 particle ·μA (4×10^{12} particles per second) and impacted on a thin target of approximately 440 μg/cm^2. The target wheel consisted of eight segments. Each segment consisted of about 95% ^{208}Pb and 5% ^{112}Sn, which enables the production of ^{155}Yb and ^{254}No with the same target wheel. ^{155}Yb has been previously used as a diagnostic and calibration measurement with the RADRIS technique, as the overall production rate was approximately 70 times greater than ^{254}No, although the production cross section is more than 1000 times greater [12]. The fusion-evaporation products were separated in flight from the primary beam using SHIP [21,22]. Approximately four ions of ^{254}No per second are available at the entrance of the gas cell with a primary beam intensity of 0.7 particle ·μA. Significant portions of the experiment were conducted in a parasitic mode of operation, where SHIP received a smaller portion of the available beam, approximately 10%. The reaction products entered the JetRIS apparatus through a 3.2 μm titanium foil. The highly charged fusion-evaporation products were stopped in the gas and converted to +1 ions through interactions with the argon buffer gas before being transported to the heated filament, where they were neutralized and carried through the de Laval nozzle for subsequent laser spectroscopy in the gas jet.

A two-step laser ionization scheme was used to produce photoions for transport to the silicon detector, with the laser pulses temporally overlapped. The first step was tuned to 333.761 nm to excite the ground state $^1S_0 \leftrightarrow {}^1P_1$ transition [12]. The light was transported to the JetRIS apparatus via optical fiber, and a spherical telescope was used to create a round beam spot with a diameter of approximately 10 mm, antipropagating with the gas jet. This laser was kept at 30 mW with a 15 kHz repetition rate, resulting in an average energy of 2 μJ per pulse. The second step was a nonresonant ionization step provided by the third harmonic of a 15 kHz repetition rate Nd:YAG laser at 355 nm. The second step laser power was kept at 30 W, resulting in an average energy of 2 mJ per pulse. A set of cylindrical telescopes was used to shape the beam into a stripe of 40 mm in width and 4 mm in height, which was injected in a transverse geometry to the jet. The dimensions of the ionization laser beam were chosen based on the repetition rate of the laser and the speed of the gas jet, so that each atom would be irradiated at least once. This specific geometric configuration was chosen to avoid shining the high-power ionization laser through the nozzle and into the gas cell. Heating of the nozzle could change its performance, and the light could potentially damage the thin entrance window separating the gas cell from SHIP. α decays were measured with the PIPS detector as a function of the first step wavelength, with a gate on the known energy of the ^{254}No α decay to avoid any increase in background from long-lived daughters of previously measured isotopes. In addition to the laser spectroscopic measurements, this also provided the first online results for the overall experimental and transport efficiencies, which could be compared to the previously discussed offline studies.

A. Experimental efficiencies

The overall experimental efficiency from the production target to the PIPS detector can be calculated based on the different measurements performed during the experiment. As the overall production and transmission of ^{254}No at SHIP is well known, the transport efficiency from the gas cell to the detector was calculated using "flushing" measurements, where no attracting potential was applied to the neutralizing filament, allowing ions to be transported through the nozzle, captured by the bent RFQ, and implanted on the PIPS detector where the characteristic α-decay was detected. The flushing count rate provides information about the efficiency of the transport of ions through the system, but cannot provide information about the processes in which losses occur, such as neutralization through collisions with the buffer gas, collection and evaporation of neutrals, or their transport through the exit

TABLE I. Experimental efficiencies of the JetRIS apparatus.

Type	Efficiency (%)
Ionization	8.4(2.8)
Transport	0.24(2)
Detection	50
Overall	0.010(3)

channel and the nozzle. The production of ^{254}No is linearly proportional to the primary beam intensity delivered by the UNILAC. Due to changes in the operation of the accelerator, this intensity fluctuated throughout the experiment and was constantly monitored. For a valid comparison of measurements performed at different times throughout the experiment, the count rate was normalized to the integrated primary beam intensity and is reported as a standard Coulomb counter (scc) which is proportional to the beam integral. The flushing measurements were performed intermittently throughout the experiment to monitor the operation of JetRIS. Flushing rates of 1045(25) and 98(20) ions/scc were observed for ^{155}Yb and ^{254}No, respectively. Previous experiments at SHIP have established approximately four ^{254}No ions per second entering the gas cell with a beam intensity of 0.7 particle ·μA, corresponding to a transport efficiency of 0.24(2)% for ^{254}No.

In addition to the flushing measurements, diagnostic laser spectroscopy measurements were performed with ^{155}Yb to check the operation of JetRIS and to determine the ionization efficiency, with the assumption that the behavior of ytterbium and nobelium would be similar as they are chemical homologues with similar atomic transition strengths [12,29]. The laser spectroscopy measurements of ^{155}Yb were performed with a broadband laser to excite the atoms, and only completed once during the online experiment.

The detected ion rate of the laser spectroscopy measurements was compared to the flushing ion rate and used to determine the experimental efficiency of the system. A flushing rate of 1045(25) ions/scc was observed, while the maximum count rate during laser spectroscopy was 45(16) ions/scc. Based on the ratio of the ions observed in the flushing mode of operation to photoions measured during laser spectroscopy, an ionization efficiency of 4(1)% was determined. A similar procedure can be applied to the flushing and maximum count rates from the nobelium measurement, albeit with a larger statistical error. Here the flushing rate of 98(20) ions/scc can be compared to a maximum of the spectrum of 8.4(2.8) ions/scc, resulting in an ionization efficiency of 8.5(3.0)%, agreeing well with the data of Yb and supporting the assumption that the two species have similar behaviors. In sum, the overall efficiency from the above values equates to a 0.010(3)% laser spectroscopy efficiency, shown in comparison with the corresponding contributions in Table I.

Although the experimental efficiency of JetRIS was two orders of magnitude lower than what is typically achieved with RADRIS, there is no inherent reason for the efficiency to be significantly small. New COMSOL simulations are guiding a redesign of the gas cell with the aim of improving the transport efficiency to the 5–10 % level. Initial results indicate that most ions are lost in the transfer from the funnel electrodes to the nozzle. Other work is ongoing to improve the reproducibility of the system, such as a new mounting system for the RFQ to prevent misalignment with the gas jet.

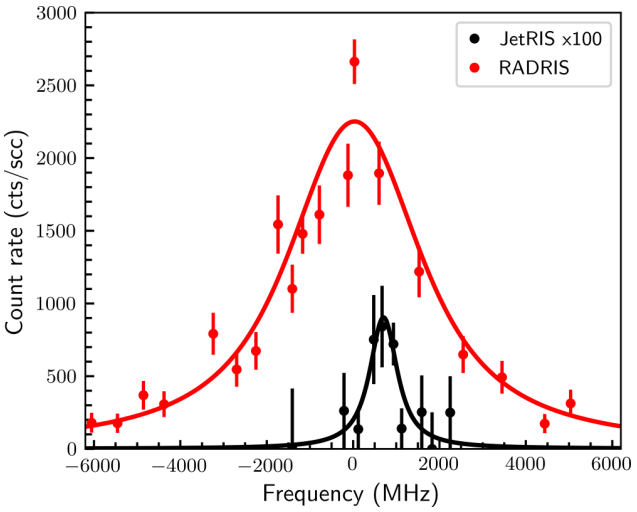

FIG. 9. Measured spectrum of ^{254}No in JetRIS with previous data from RADRIS [11]. The achievable resolution with JetRIS is improved fivefold compared to RADRIS.

B. ^{254}No laser spectroscopy

The main goal of the JetRIS beamtime was the measurement of the $^1S_0 \leftrightarrow {}^1P_1$ transition of the ^{254}No nuclear ground state as a proof of principle that JetRIS is capable of high-resolution measurements of very low production rate nuclides.

The targeted transition of ^{254}No was successfully measured, and is shown in comparison to a previous measurement from the RADRIS experiment [11] in Fig. 9. ^{254}No has nuclear spin $I = 0$, featuring no hyperfine splitting of the transition and thus only one peak was expected.

The spectrum was fit to the data shown in Fig. 9 using most likelihood estimation (MLE) due to the low statistics of the experiment. The fit was performed with raw counts before normalization, while the fit function was scaled per data point according to the relative beam intensity scaling. The fit was performed with an assumption of zero background, with the data gated on α decays within an energy range of 7.93–8.24 MeV. Surface ionization of species from the heated filament has been previously studied at RADRIS [30,31] and is known to be negligible. The centroid resonance frequency of the spectrum was determined to be 29 951.480(2)(10) cm^{-1}, with the statistical and systematic uncertainties shown, respectively. The statistical and systematic contributions to the uncertainty are given separately and will be described in more detail. It is noted that although the overall efficiency of JetRIS is significantly lower than that of RADRIS, the enhancement in precision allows for the extraction of the centroid with a similar statistical uncertainty. The fit resulted in a full width at half-maximum (FWHM) of 770 ± 300 MHz with a G-test score of 0.82. The previously reported measurement of ^{254}No from RADRIS featured a spectral resolution of approximately 3900 MHz [11], demonstrating a factor of 5 improvement in JetRIS.

TABLE II. Contributions to the uncertainty in the centroid frequency of the $^1S_0 \leftrightarrow {}^1P_1$ transition of ^{254}No with JetRIS and RADRIS.

Uncertainty	RADRIS (MHz)	JetRIS (MHz)
Fit	125	60
Wavemeter	150	60
Ne Lamp/HeNe calibration	150	150
Pressure shift	1025	
Doppler shift		150
Total	1350	370

Previous offline measurements of Dy [20] and Cu isotopes achieved a higher resolution, and based on the mass dependence of the Doppler broadening within the gas jet, we expect a spectral resolution of down to 200 MHz for ^{254}No. We believe that our measurement was significantly affected by power broadening. The saturation photon flux for this transition is 2.5×10^{12} photons pulse^{-1} cm^{-2} [11], whereas this measurement used 4.3×10^{12} photons pulse^{-1} cm^{-2}, almost twice the saturation flux. Additionally, previous measurements with Cu isotopes at KU Leuven have shown that saturation conditions in the gas jet are significantly different from those in the gas cell environment, with a tenfold reduction in the saturation flux in the gas jet [24]. Improvements in the overall efficiency of the system will allow lower laser power to be used for the first-step laser excitation, reducing the effect of this broadening.

C. Centroid discrepancy with RADRIS measurements

The centroid of the $^1S_0 \leftrightarrow {}^1P_1$ transition was determined to be 29 961.480(2)(12) cm^{-1}, with a shift of approximately +700 MHz in relation to the previously reported measurement in RADRIS [11]. However, the JetRIS measurement is red Doppler-shifted due to the antipropagating geometry of the first-step laser in relation to the hypersonic flow direction, contributing a shift of 1725(150) MHz. The stagnation temperature, T_0, was assumed to be room temperature as both simulations [19] and offline measurements have established that the stagnation temperature is consistent with room temperature. The uncertainty in the stagnation temperature was conservatively assigned using an upper limit on the temperature established in Ref. [20] using the JetRIS apparatus. In that measurement, a large resistively heated atom source was placed in the mouth of the nozzle, and it is assumed that it induces more heating of the surrounding gas than the thin filament used in the current measurements. After correcting for the Doppler shift, a discrepancy of 2400 MHz is found between the JetRIS and RADRIS data.

The uncertainties considered in this analysis can be seen in Table II. The most significant source of uncertainty results from the unknown pressure shift in the RADRIS data, which was conservatively estimated at −10 MHz/mbar based on previous measurements in thallium [9]. Recent systematic measurements with the wavemeters used in both experiments have revealed further systematic uncertainties. Two different wavemeters of the same model were used for the experiments, both WS7 (HighFinesse) wavemeters, although with separate calibration methods. The JetRIS experiment utilized a frequency-stabilized helium-neon (HeNe) laser for calibration. This HeNe laser features a 150 MHz uncertainty in its wavelength, while the wavemeter boasts a 30 MHz uncertainty in its accuracy. The RADRIS wavemeter relied on an internal neon lamp for calibration, with a 150 MHz uncertainty, although it is possible to calibrate it with an external HeNe laser. Both wavemeters were compared to search for a possible source of the discrepancy in the data by measuring the fundamental and doubled UV light of the pulsed dye amplifier described above. The laser light was coupled to a single-mode fiber with two outputs, allowing for simultaneous measurement of the laser light. The use of a single-mode fiber introduced an additional 30 MHz uncertainty in the measurement of the fundamental light, and subsequently a 60 MHz uncertainty for the doubled laser light. A small difference of 150 MHz was observed between the two wavemeters when using different calibration sources, but this was eliminated by calibration of both wavemeters with the same HeNe laser.

The overall uncertainty in the centroid for each measurement was determined summing in quadrature the statistical error of the fit and the systematic uncertainty introduced by the wavemeters and further summing the systematic uncertainties introduced by the Doppler and pressure shifts. The significance of the discrepancy between the JetRIS and RADRIS centroids rises to the 1.6 σ level. Future measurements are planned to improve our understanding of the systematic uncertainties of both the JetRIS and RADRIS experiments and to resolve this discrepancy. Although challenging in practice, a different geometrical configuration of the lasers, with both propagating transverse to the gas jet, could avoid the Doppler shift and reduce the possible sources of uncertainty in the measurement. It is worth noting that a centroid shift in the JetRIS data stemming from the slip effect, where the seeded heavy mass atoms in the gas jet have a lower velocity in comparison to that of the carrier gas, can be ruled out. Recent measurements were performed at KU Leuven with ^{232}Th atoms seeded in an argon flow to form a gas jet with an identical nozzle and very similar experimental conditions. The results show that ^{232}Th moves in the hypersonic jet at a similar speed to the argon carrier gas [32]. We believe that significant fluctuations in the room temperature of the laser room due to the weather conditions and operation of the laser systems could have introduced a systematic drift in the wavemeter calibration. Additionally, as the pressure shift in the RADRIS data is currently the largest source of the error, future measurements are planned at GSI to measure the ^{254}No spectrum at a range of pressures, allowing for experimental determination of the pressure shift.

V. OUTLOOK

These results are a promising first step towards high-resolution laser spectroscopy measurements of the heavy actinides, allowing for more precise determination of nuclear properties from hyperfine spectra. Current work is focused on improving the experimental efficiency. Additionally, a multireflection time-of-flight (MR-TOF) mass spectrometer is being commissioned for use with JetRIS. The incorporation of the MR-TOF will allow for detection methods beyond

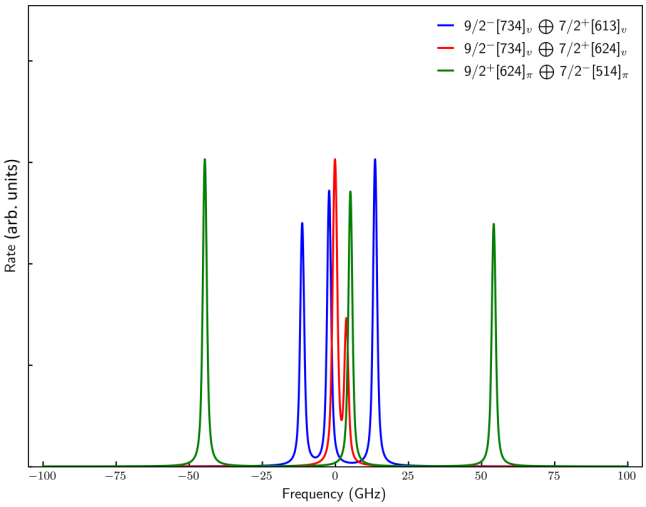

FIG. 10. Hyperfine splitting of the $K = 8^-$ isomer in ^{254}No compared to the nuclear ground state. Three possibilities of the nucleonic configuration are shown, calculated from g_k values provided in Ref. [37], and result in substantially different splittings. The resolution shown here is based on the demonstrated spectral resolution of 770 MHz.

alpha decay, providing access to isotopes or elements with unfavorable decay modes and/or longer half-lives.

With these upgrades, future measurements with the JetRIS apparatus are planned at GSI aiming at nuclides and isomers that feature hyperfine splitting, providing important information about the nuclear structure with higher precision than what is available with the RADRIS technique. Of particular interest is the $K = 8^-$ isomer of ^{254}No, which is populated in approximately 1/3 of the produced ^{254}No nuclei [33]. This high angular momentum isomer was observed in decay spectroscopy studies [33–36], however the configuration of the two-quasiparticle state on which the isomer is based could not be established unambiguously. This isomer has remained out of reach of RADRIS due to its short lifetime ($T_{1/2} \approx 250$ ms). Due to the short lifetime of the isomer in relation to the nuclear ground state, the α-decay energy cannot be used to distinguish the two. However, due to the nonzero nuclear spin, and as each of the possible configurations is predicted to have different g -factors, the hyperfine splitting of each configuration would be sufficiently different that high-resolution laser spectroscopy could both separate the isomer from the nuclear ground state and determine which of the possible configurations is correct. The predicted spectra of the three likely candidates for the configuration in the $K = 8^-$ isomer are shown in Fig. 10 with the demonstrated spectral resolution of JetRIS. The hyperfine spectra were calculated using g_k values predicted from Ref. [37]. It is noted that there is a possible overlap between the resonance of the $K = 8^-$ isomer and the nuclear ground state, meaning that a contribution by the $K = 8^-$ isomer to the spectral broadening and discrepancy in the centroid frequency discussed is possible. However, based on the production rate of the isomer and the transport time through the JetRIS apparatus, the contribution would be rather small. Additionally, the above calculations do not account for the isomer shift between the ground state and the $K = 8^-$ isomer, which, based on other isomers in heavy nuclei, could rise to the level of hundreds of MHz [38,39]. However, we cannot fully exclude the possibility of the presence of the isomer in our measurements, and future measurements will clarify the situation.

VI. CONCLUSION

An apparatus utilizing the in-gas-jet laser ionization spectroscopy technique was successfully characterized offline and commissioned for online studies of heavy actinides at GSI. This apparatus combines the efficient RADRIS technique of heated filament neutralization with the in-gas-jet resonant ionization spectroscopy technique to provide high sensitivity with high resolution. Offline characterization was performed with stable and radioactive sources to understand the capabilities of the system as well as the optimal operating parameters. An online experiment was performed at GSI, where a sub-GHz laser spectroscopic measurement of ^{254}No was performed, with a fivefold improvement in the resolution over existing measurements. This improvement in the spectral resolution opens the door for high-resolution measurements in the heavy actinide region, providing information on the nuclear structure with high precision, which is critical for benchmarking nuclear theory. New technical improvements are being incorporated to improve the performance of JetRIS, such as a multireflection time-of-flight mass spectrometer and changes in the design of the gas cell to improve the efficiency. This work will open opportunities to access new elements, isotopes, and isomers in the heavy actinide region.

ACKNOWLEDGMENTS

We would like to thank Dr. Dennis Renisch at the Johannes Gutenberg University of Mainz for providing the ^{223}Ra recoil source used for the commissioning work. The online measurements presented here were performed at the velocity filter SHIP at the GSI Helmholtzzentrum für Schwerionenforschung, Darmstadt (Germany) in the frame of FAIR Phase-0 (Experiment U321). We would also like to thank the GSI ion source and accelerator staff for providing intense ion beams. This project has received funding from the European Union's Horizon 2020 research and innovation programme under Grant Agreement No. 861198-LISA-H2020-MSCA-ITN-2019. M.L., E.K., and E.R.-R. acknowledge funding from the European Research Council (ERC) under the European Union's Horizon 2020 research and innovation programme (Grant Agreement No. 819957). P.C. acknowledges the European Union's Horizon 2020 research and innovation programme under the Marie Skłodowska-Curie Grant Agreement No. 101026762. This work has received funding from the German Bundesministerium für Bildung und Forschung (BMBF, Germany) under Project No. 05P21UMFN3 and the Research Foundation Flanders (FWO, Belgium) BOF KU Leuven (C14/22/104) and the FWO and F.R.S.-FNRS under the Excellence of Science (EOS) program (40007501). T.W. acknowledges funding from the Bundesministerium für Bildung und Forschung (BMBF, Germany) under Grants No. 05P15RDFN1 and No. 05P21RDFN1.

[1] B. Cheal and K. T. Flanagan, Progress in laser spectroscopy at radioactive ion beam facilities, J. Phys. G **37**, 113101 (2010).

[2] P. Campbell, I. Moore, and M. Pearson, Laser spectroscopy for nuclear structure physics, Prog. Part. Nucl. Phys. **86**, 127 (2016).

[3] W. Nörtershäuser, New developments in laser spectroscopy for ribs, Int. School Phys. Enrico Fermi **201**, 293 (2019).

[4] M. Block, M. Laatiaoui, and S. Raeder, Recent progress in laser spectroscopy of the actinides, Prog. Part. Nucl. Phys. **116**, 103834 (2021).

[5] X. Yang, S. Wang, S. Wilkins, and R. G. Ruiz, Laser spectroscopy for the study of exotic nuclei, Prog. Part. Nucl. Phys. **129**, 104005 (2023).

[6] H. Backe, M. Hies, H. Kunz, W. Lauth, O. Curtze, P. Schwamb, M. Sewtz, W. Theobald, R. Zahn, K. Eberhardt, N. Trautmann, D. Habs, R. Repnow, and B. Fricke, Isotope shift measurements for superdeformed fission isomeric states, Phys. Rev. Lett. **80**, 920 (1998).

[7] M. Sewtz, H. Backe, A. Dretzke, G. Kube, W. Lauth, P. Schwamb, K. Eberhardt, C. Grüning, P. Thörle, N. Trautmann, P. Kunz, J. Lassen, G. Passler, C. Z. Dong, S. Fritzsche, and R. G. Haire, First observation of atomic levels for the element fermium ($Z = 100$), Phys. Rev. Lett. **90**, 163002 (2003).

[8] C. Granados, P. Creemers, R. Ferrer, L. P. Gaffney, W. Gins, R. de Groote, M. Huyse, Y. Kudryavtsev, Y. Martínez, S. Raeder, S. Sels, C. Van Beveren, P. Van den Bergh, P. Van Duppen, K. Wrzosek-Lipska, A. Zadvornaya, A. E. Barzakh, B. Bastin, P. Delahaye, L. Hijazi *et al.*, In-gas laser ionization and spectroscopy of actinium isotopes near the $N = 126$ closed shell, Phys. Rev. C **96**, 054331 (2017).

[9] W. Lauth, H. Backe, M. Dahlinger, I. Klaft, P. Schwamb, G. Schwickert, N. Trautmann, and U. Othmer, Resonance ionization spectroscopy in a buffer gas cell with radioactive decay detection, demonstrated using ^{208}Tl, Phys. Rev. Lett. **68**, 1675 (1992).

[10] H. Backe, W. Lauth, M. Block, and M. Laatiaoui, Prospects for laser spectroscopy, ion chemistry and mobility measurements of superheavy elements in buffer-gas traps, Nucl. Phys. A **944**, 492 (2015).

[11] M. Laatiaoui, W. Lauth, H. Backe, M. Block, D. Ackermann, B. Cheal, P. Chhetri, Ch. E. Düllmann, P. Van Duppen, J. Even, R. Ferrer, F. Giacoppo, S. Götz, F. P. Heßberger, M. Huyse, O. Kaleja, J. Khuyagbaatar, P. Kunz, F. Lautenschläger, A. K. Mistry *et al.*, Atom-at-a-time laser resonance ionization spectroscopy of nobelium, Nature (London) **538**, 495 (2016).

[12] F. Lautenschläger, P. Chhetri, D. Ackermann, H. Backe, M. Block, B. Cheal, A. Clark, C. Droese, R. Ferrer, F. Giacoppo, S. Götz, F. Heßberger, O. Kaleja, J. Khuyagbaatar, P. Kunz, A. Mistry, M. Laatiaoui, W. Lauth, S. Raeder, T. Walther *et al.*, Developments for resonance ionization laser spectroscopy of the heaviest elements at SHIP, Nucl. Instrum. Methods Phys. Res. Sect. B **383**, 115 (2016).

[13] S. Raeder, D. Ackermann, H. Backe, R. Beerwerth, J. C. Berengut, M. Block, A. Borschevsky, B. Cheal, P. Chhetri, Ch. E. Düllmann, V. A. Dzuba, E. Eliav, J. Even, R. Ferrer, V. V. Flambaum, S. Fritzsche, F. Giacoppo, S. Götz, F. P. Heßberger, M. Huyse *et al.*, Probing sizes and shapes of nobelium isotopes by laser spectroscopy, Phys. Rev. Lett. **120**, 232503 (2018).

[14] P. Chhetri, D. Ackermann, H. Backe, M. Block, B. Cheal, C. Droese, Ch. E. Düllmann, J. Even, R. Ferrer, F. Giacoppo, S. Götz, F. P. Heßberger, M. Huyse, O. Kaleja, J. Khuyagbaatar, P. Kunz, M. Laatiaoui, F. Lautenschläger, W. Lauth, N. Lecesne *et al.*, Precision measurement of the first ionization potential of nobelium, Phys. Rev. Lett. **120**, 263003 (2018).

[15] J. Warbinek, B. Anđelić, M. Block, P. Chhetri, A. Claessens, R. Ferrer, F. Giacoppo, O. Kaleja, T. Kieck, E. Kim, M. Laatiaoui, J. Lantis, A. Mistry, D. Münzberg, S. Nothhelfer, S. Raeder, E. Rey-Herme, E. Rickert, J. Romans, E. Romero-Romero *et al.*, Advancing radiation-detected resonance ionization towards heavier elements and more exotic nuclides, Atoms **10**, 41 (2022).

[16] Y. Kudryavtsev, R. Ferrer, M. Huyse, P. Van den Bergh, and P. Van Duppen, The in-gas-jet laser ion source: Resonance ionization spectroscopy of radioactive atoms in supersonic gas jets, Nucl. Instrum. Methods Phys. Res. Sect. B **297**, 7 (2013).

[17] S. Raeder, B. Bastin, M. Block, P. Creemers, P. Delahaye, R. Ferrer, X. Fléchard, S. Franchoo, L. Ghys, L. Gaffney, C. Granados, R. Heinke, L. Hijazi, M. Huyse, T. Kron, Y. Kudryavtsev, M. Laatiaoui, N. Lecesne, F. Luton, I. Moore *et al.*, Developments towards in-gas-jet laser spectroscopy studies of actinium isotopes at LISOL, Nucl. Instrum. Methods Phys. Res. Sect. B **376**, 382 (2016).

[18] R. Ferrer, A. Barzakh, B. Bastin, R. Beerwerth, M. Block, P. Creemers, H. Grawe, R. de Groote, P. Delahaye, X. Fléchard, S. Franchoo, S. Fritzsche, L. P. Gaffney, L. Ghys, W. Gins, C. Granados, R. Heinke, L. Hijazi, M. Huyse, T. Kron *et al.*, Towards high-resolution laser ionization spectroscopy of the heaviest elements in supersonic gas jet expansion, Nat. Commun. **8**, 14520 (2017).

[19] S. Raeder, M. Block, P. Chhetri, R. Ferrer, S. Kraemer, T. Kron, M. Laatiaoui, S. Nothhelfer, F. Schneider, P. Van Duppen, M. Verlinde, E. Verstraelen, T. Walther, and A. Zadvornaya, A gas-jet apparatus for high-resolution laser spectroscopy on the heaviest elements at SHIP, Nucl. Instrum. Methods Phys. Res. Sect. B **463**, 272 (2020).

[20] D. Münzberg, M. Block, A. Claessens, R. Ferrer, M. Laatiaoui, J. Lantis, S. Nothhelfer, S. Raeder, and P. Van Duppen, Resolution characterizations of JetRIS in Mainz using ^{164}Dy, Atoms **10**, 57 (2022).

[21] G. Münzenberg, W. Faust, S. Hofmann, P. Armbruster, K. Güttner, and H. Ewald, The velocity filter SHIP, a separator of unslowed heavy ion fusion products, Nucl. Instrum. Methods **161**, 65 (1979).

[22] M. Block, F. Giacoppo, F.-P. Heßberger, and S. Raeder, Recent progress in experiments on the heaviest nuclides at SHIP, Riv. Nuovo Cimento **45**, 279 (2022).

[23] R. Ferrer, M. Verlinde, E. Verstraelen, A. Claessens, M. Huyse, S. Kraemer, Y. Kudryavtsev, J. Romans, P. Van den Bergh, P. Van Duppen, A. Zadvornaya, O. Chazot, G. Grossir, V. I. Kalikmanov, M. Nabuurs, and D. Reynaerts, Hypersonic nozzle for laser-spectroscopy studies at 17 K characterized by resonance-ionization-spectroscopy-based flow mapping, Phys. Rev. Res. **3**, 043041 (2021).

[24] E. Verstraelen, Laser Spectroscopy of Actinides: Octupole Deformation and Gas-Jet Characterization, Ph.D. thesis, KU Leuven (2021).

[25] A. Zadvornaya, P. Creemers, K. Dockx, R. Ferrer, L. P. Gaffney, W. Gins, C. Granados, M. Huyse, Y. Kudryavtsev, M. Laatiaoui, E. Mogilevskiy, S. Raeder, S. Sels, P. Van den Bergh, P. Van Duppen, M. Verlinde, E. Verstraelen, M. Nabuurs,

D. Reynaerts, and P. Papadakis, Characterization of supersonic gas jets for high-resolution laser ionization spectroscopy of heavy elements, Phys. Rev. X **8**, 041008 (2018).

[26] M. Verlinde, R. Ferrer, A. Claessens, C. A. Granados, S. Kraemer, Y. Kudryavtsev, D. Li, P. Van den Bergh, P. Van Duppen, and E. Verstraelen, Single-longitudinal-mode pumped pulsed-dye amplifier for high-resolution laser spectroscopy, Rev. Sci. Instrum. **91**, 103002 (2020).

[27] O. Kaleja, B. Anđelić, K. Blaum, M. Block, P. Chhetri, C. Droese, Ch. E. Düllmann, M. Eibach, S. Eliseev, J. Even, S. Götz, F. Giacoppo, N. Kalantar-Nayestanaki, M. Laatiaoui, E. M. Ramirez, A. Mistry, T. Murböck, S. Raeder, L. Schweikhard, and P. Thirolf, The performance of the cryogenic buffer-gas stopping cell of SHIPTRAP, Nucl. Instrum. Methods Phys. Res. Sect. B **463**, 280 (2020).

[28] Y. T. Oganessian, V. K. Utyonkov, Y. V. Lobanov, F. S. Abdullin, A. N. Polyakov, I. V. Shirokovsky, Y. S. Tsyganov, A. N. Mezentsev, S. Iliev, V. G. Subbotin, A. M. Sukhov, K. Subotic, O. V. Ivanov, A. N. Voinov, V. I. Zagrebaev, K. J. Moody, J. F. Wild, N. J. Stoyer, M. A. Stoyer, and R. W. Lougheed, Measurements of cross sections for the fusion-evaporation reactions ^{204,206,207,208}Pb + ^{48}Ca and ^{207}Pb + ^{34}S : decay properties of the even-even nuclides ^{238}Cf and ^{250}No, Phys. Rev. C **64**, 054606 (2001).

[29] W. F. Meggers, C. H. Corliss, and B. F. Scribner, Natl. Bur. Stand. (US), Monogr. **145**, 292 (1975).

[30] M. Laatiaoui, H. Backe, M. Block, F.-P. Heßberger, P. Kunz, F. Lautenschläger, W. Lauth, M. Sewtz, and T. Walther, On laser spectroscopy of the element nobelium (zÂ =Â 102), Eur. Phys. J. D **68**, 71 (2014).

[31] T. Murböck, S. Raeder, P. Chhetri, K. Diaz, M. Laatiaoui, F. Giacoppo, and M. Block, Filament studies for laser spectroscopy on lawrencium, Hyperfine Interact. **241**, 35 (2020).

[32] A. Claessens, Laser ionization spectroscopy of ^{254}No and ^{229}Th in hypersonic gas jets, Ph.D. thesis, KU Leuven (2024).

[33] F. P. Heßberger, S. Antalic, B. Sulignano, D. Ackermann, S. Heinz, S. Hofmann, B. Kindler, J. Khuyagbaatar, I. Kojouharov, P. Kuusiniemi, M. Leino, B. Lommel, R. Mann, K. Nishio, A. G. Popeko, Š. Šáro, B. Streicher, J. Uusitalo, M. Venhart, and A. V. Yeremin, Decay studies of *K* isomers in ^{254}No, Eur. Phys. J. A **43**, 55 (2010).

[34] A. Ghiorso, K. Eskola, P. Eskola, and M. Nurmia, Isomeric states in ^{250}Fm and ^{254}No, Phys. Rev. C **7**, 2032 (1973).

[35] S. K. Tandel, T. L. Khoo, D. Seweryniak, G. Mukherjee, I. Ahmad, B. Back, R. Blinstrup, M. P. Carpenter, J. Chapman, P. Chowdhury, C. N. Davids, A. A. Hecht, A. Heinz, P. Ikin, R. V. F. Janssens, F. G. Kondev, T. Lauritsen, C. J. Lister, E. F. Moore, D. Peterson *et al.*, K isomers in ^{254}No : Probing single-particle energies and pairing strengths in the heaviest nuclei, Phys. Rev. Lett. **97**, 082502 (2006).

[36] R. Clark, K. Gregorich, J. Berryman, M. Ali, J. Allmond, C. Beausang, M. Cromaz, M. Deleplanque, I. Dragojević, J. Dvorak, P. Ellison, P. Fallon, M. Garcia, J. Gates, S. Gros, H. Jeppesen, D. Kaji, I. Lee, A. Macchiavelli, K. Morimoto *et al.*, High-K multi-quasiparticle states in ^{254}No, Phys. Lett. B **690**, 19 (2010).

[37] R. D. Herzberg, P. T. Greenlees, P. A. Butler, G. D. Jones, I. G. Darby, S. Eeckhaudt, T. Grahn, C. Gray-Jones, F. P. Hessberger, and P. JonesIsomer spectroscopy of ^{254}No, Phys. Scr. **T125**, 73 (2006).

[38] K. M. Lynch, J. Billowes, M. L. Bissell, I. Budinčević, T. E. Cocolios, R. P. De Groote, S. De Schepper, V. N. Fedosseev, K. T. Flanagan, S. Franchoo, R. F. Garcia Ruiz, H. Heylen, B. A. Marsh, G. Neyens, T. J. Procter, R. E. Rossel, S. Rothe, I. Strashnov, H. H. Stroke, and K. D. A. Wendt, Decay-assisted laser spectroscopy of neutron-deficient francium, Phys. Rev. X **4**, 011055 (2014).

[39] J. G. Cubiss, A. E. Barzakh, M. D. Seliverstov, A. N. Andreyev, B. Andel, S. Antalic, P. Ascher, D. Atanasov, D. Beck, J. Biero, K. Blaum, C. Borgmann, M. Breitenfeldt, L. Capponi, T. E. Cocolios, T. Day Goodacre, X. Derkx, H. De Witte, J. Elseviers, D. V. Fedorov *et al.*, Charge radii and electromagnetic moments of $^{195-211}$at, Phys. Rev. C **97**, 054327 (2018).

5.3 Publication III

The following article 'Multiple-reflection time-of-flight mass spectrometer assisted laser spectroscopy of ^{nat}Sm' was published in *Nuclear Instruments and Methods in Physics Research Section B*, **569**, 165884 (2025) by D. Münzberg et al. It reports on ToF-assisted resonance ionization spectroscopy on ^{nat}Sm. Six different laser schemes were developed and characterized with all naturally occuring isotopes being measured. Here the isotope shifts were determined and through mean square nuclear charge radii-values from literature and Kingplots the individual mass shift and field shift contributions were calculated. In the cases of $I \neq 0$ hyperfine structure was observed and the hyperfine parameter $\mathcal{A}$ could be determined. In this publication the laser ions were also utilized for the characterization of the MR-ToF MS which is outlined as a future addition to the JetRIS to improve its capabilities for measuring stable and long-lived isotopes via direct ion detection. A mass-resolving power dependent on the number of revolutions with a maximum of 25000 for the experimental conditions using the laser ion source without a cooler buncher was determined. These results were cross checked via simulations using SIMION 8.0. These measurements showed a relative efficiency of 20%, meaning 80% of the ions were lost during the trapping within the MR-ToF MS. These results were compared with tandem simulations of ions from a cooler buncher designed by A. Brizard injected into the MR-ToF MS. These simulations showed that the cooler buncher ions have a greatly lowered transversal and slightly lowered longitudinal emittance which lead to a predicted improvement in relative efficiency to 80% with a maximum mass resolving power of 100000 after 4000 revolutions.

5.3.1 Author contributions

The author contributed to this work by assembly of the MR-ToF MS, conducting first comissioning experiments to get the system operational, designing the ion source for it, as well as the laser ion source, setting up the laser for spectroscopy, conducting the spectroscopy measurements, as well as data analysis, including the simulations of the laser ion source, the MR-ToF MS, as well as the tandem simulations using the ions from the cooler buncher simulations. The author is the main author of the publication and has written its draft and refined it with input from the co-authors.

Nuclear Instruments and Methods in Physics Research B 569 (2025) 165884

Contents lists available at ScienceDirect

Nuclear Inst. and Methods in Physics Research, B

journal homepage: www.elsevier.com/locate/nimb

Full length article

Multiple-reflection time-of-flight mass spectrometer assisted laser spectroscopy of ^{nat}Sm

Danny Münzberg [a,b,c,*], Alexandre Brizard [d], Tim van de Vendel [a,e], Jana Weyrich [a,b,c], Michael Block [a,b,c], Julia Even [e], Christian Helmel [f], Nathalie Lecesne [d], Sebastian Raeder [a,b], Daniel Rodríguez [g], Hervé Savajols [d], Klaus Wendt [c]

[a] GSI Helmholtzzentrum für Schwerionenforschung GmbH, Planckstraße 1, Darmstadt 64291, Germany
[b] Helmholtz Institut Mainz, Staudingerweg 18, Mainz 55128, Germany
[c] Johannes Gutenberg-Universität Mainz, Saarstraße 21, Mainz 55128, Germany
[d] GANIL, CEA/DRF-CNRS/IN2P3, Bd Henri Becquerel, Caen 14000, France
[e] University of Groningen, Broerstraat 5, Groningen 9712 CP, The Netherlands
[f] Technische Universität Darmstadt, Karolinenplatz 5, Darmstadt 64289, Germany
[g] Universidad de Granada, Granada 18071, Spain

ARTICLE INFO

Keywords:
RIS
Laser spectroscopy
JetRIS
MR-ToF MS

ABSTRACT

In this article we report laser Resonance Ionization Spectroscopy (RIS) experiments on ^{nat}Sm with the assistance of a ToF-gated ion detection. This detection scheme enabled measurements of a given atomic transition for each isotope simultaneously without the need for isotopically enriched samples. Using this approach, multiple different excitation schemes were developed and specific mass and field shifts and the hyperfine parameter $\mathcal{A}$ of the transitions were determined. Furthermore this setup was used to commission a MR-ToF MS, which shall be integrated in the in-gas-Jet Resonance Ionization Spectroscopy (JetRIS) setup at GSI to enhance its capabilities for on-line measurements. This upgrade will enable on-line laser spectroscopy experiments on neutron-deficient samarium isotopes and heavy nuclides independent of their decay mode with a suitable half-life time, that are inaccessible with present techniques, such as ^{254}Md.

1. Introduction

Laser spectroscopy is a tool for studying the structure of the electron shell of an atom and its nucleus. A particular interest arises in the region of the heaviest elements where the experimental knowledge of atomic and nuclear properties is scarce. The existence of these heavy nuclides is due to nuclear shell structure effects, stabilizing them against spontaneous fission [1–3]. Laser spectroscopy gives access to atomic levels, atomic state lifetimes and the ionization potential, for example. Such properties are affected by strong relativistic effects in the heaviest elements. Furthermore, electron correlations and quantum electrodynamics effects that are challenging theoretical calculations, play an important role. Also, laser spectroscopy enables determining nuclear properties such as spins and electromagnetic moments for probing the nuclear shell structure and the evolution of deformation. Isotopes of the heaviest elements can only be produced in minute quantities hampering experimental investigations. To enable detailed optical studies, the in-gas-**jet** **R**esonance **I**onization **S**pectroscopy (JetRIS) technique has been developed at GSI, Darmstadt, Germany [4]. Presently, JetRIS relies on radiation detection which enabled the measurement of an atomic transition of ^{254}No with improved spectral resolution [5] utilizing the α-decay detection of laser ions to achieve a low background measurement. In the future, such measurements are foreseen to be extended to additional heavy nuclei. For example the element mendelevium (Md, $Z = 101$), yet unstudied by laser spectroscopy, is of interest. It can be accessed producing the isotope ^{254}Md via the electron capture decay of ^{254}No. So far, no atomic levels of the element mendelevium have been reported and only theoretical predictions exist [6]. Laser spectroscopy can reveal these electronic levels [7]. This isotope, only decays via electron capture [8], complicating a decay-based detection. For this purpose, a **M**ultiple-**R**eflection **T**ime-**o**f-**F**light **M**ass **S**pectrometer (MR-ToF MS) [9] will be integrated in the JetRIS setup. This enables mass selected direct ion detection with high sensitivity making a low background measurement possible. Another advantage of the MR-ToF MS arises from additional beam purification during the measurement, utilizing in-trap deflector electrodes. Offline studies revealed that the heated filament in JetRIS despite the applied repulsive

* Corresponding author at: GSI Helmholtzzentrum für Schwerionenforschung GmbH, Planckstraße 1, Darmstadt 64291, Germany.
E-mail address: D.Muenzberg@gsi.de (D. Münzberg).

https://doi.org/10.1016/j.nimb.2025.165884
Received 7 July 2025; Received in revised form 27 August 2025; Accepted 29 September 2025
Available online 10 October 2025

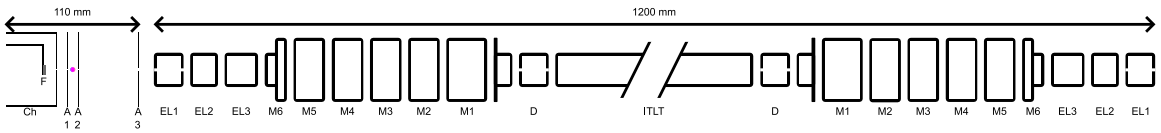

Fig. 1. Schematic of the MR-ToF MS with the laser ion source used in the experiment. The laser ion source consists of a filament (F), a filament channel (Ch) and three apertures (A1-3). The coloured circle shows the overlap region of the lasers. The MR-ToF MS is symmetrical with respect to its middle. Starting from the outside going inwards, there is an einzel lens (EL) consisting of three electrodes, followed by the stack of mirror electrodes (M) 1–6. Further inside there is a slitted deflector electrode (D) followed by an in-trap-lift-tube (ITLT).

potential can still yield ionic background affecting the identification of so far unknown species [10].

To investigate the potential of ToF-assisted laser spectroscopy and characterize the MR-ToF MS, two-step **R**esonant **I**onization **S**pectroscopy (RIS) on ^{nat}Sm has been performed. Atomic transitions to excited atomic states in the range between $29\,695 - 30\,801\,\mathrm{cm}^{-1}$ were investigated utilizing mass-selected ion detection, which will be discussed in Sec. 2.4. Isotope shifts for stable Sm isotopes were obtained and the hyperfine structure of the odd-mass stable isotopes was determined. Since no samarium isotope with a mass number below $A = 138$ has been measured via laser spectroscopy so far [11], the development of laser excitation schemes is a prerequisite for future online studies. The most neutron-deficient samarium isotope experimentally known is ^{129}Sm, even though the isotope with $A = 130$ has not been observed yet [8].

The samarium isotopes from $A = 129$ to $A = 137$ can be produced via fusion-evaporation reactions and feature lifetimes which are suitable for laser spectroscopy with JetRIS. Samarium isotopes of interest could be produced by a reaction of a sulphur beam on palladium [12]. For example, ^{132}Sm could be produced, using naturally occurring isotopes ^{32}S + ^{102}Pd in the 2 n evaporation channel. Samarium-isotopes until the drip line are expected to be accessible through the reaction of ^{40}Ca + ^{92}Mo, which offers the potential to produce all remaining samarium isotopes below $A = 138$ when utilizing the many naturally occurring stable calcium and molybdenum isotopes.

To expand measurements with JetRIS to be independent on the decay, the setup will be extended, with a cooler buncher, followed by a pulsed drift tube and the MR-ToF MS, with an ion detector at the end, as discussed in Section 3. The design of the cooler buncher has been finalized and the expected performance will be discussed in Section 3.1. As JetRIS was used during online beamtime at GSI, Darmstadt with the decay assisted detection, the MR-ToF MS was commissioned independently within this work. The measured performance of the MR-ToF MS was compared to ion trajectory simulations using SIMION 8.1 [13,14], for validation of their predictive power. These results will be discussed in Section 3.2 together with the expected performance of the MR-ToF MS in combination with the cooler buncher and the pulsed drift tube.

2. Experimental setup

In this work the MR-ToF MS has been tested in stand-alone mode with a dedicated laser ion source utilizing the filament technique of JetRIS. The schematic overview of this setup is shown in Fig. 1. It consists of the laser ion source, the MR-ToF MS and the detector setup with two metal grids in front where the one closer to the detector can be set on an electric potential to measure the longitudinal energy distribution of the ions. To detect the ions, a commercial ion detector (MagneToF mini, ETP ion detect) is used. The readout of the detector signal to acquire ToF spectra was done using a time-to-digital converter (MCS8 A, FASTComTech). The MagneToF mini produces an analog signal with a negative voltage and the threshold for the discriminator of the MCS8 A was set to −7 mV. For the timing pattern, a 9520 Pulse Delay Generator (Quantum Composers) was used. The pressure in the system was typically $p = 5 \cdot 10^{-8}$ mbar, leading to a mean free path of roughly 1.2 km.

2.1. MR-ToF MS

The MR-ToF MS used within this study was designed at the Technical University of Darmstadt in the frame of the 'DA's MR-ToF collaboration'. The design of the MR-ToF MS is described in detail in Ref. [9]. In the following, a brief overview of the setup will be given. The MR-ToF MS, as shown in Fig. 1, is axially symmetric with respect to its middle point and consists of four main parts. On both ends an einzel lens (EL) is placed, where the outer most electrode consists of four equal pieces to allow for steering of the ion beam. Next to the einzel lens is the mirror-electrode stack, consisting of 6 cylindrical electrodes (M1–M6) which can be biased individually. Going further inwards is the in-trap-deflector electrode, another cylindrical electrode cut into four equal pieces to be able to deflect ions while trapped for beam purification. In the middle of the setup is the in-trap-lift tube (ITLT) which allows adjusting the kinetic energy of the ions to trap and eject them without pulsing the mirror electrodes [15]. The voltages applied to the MR-ToF MS electrodes are given in Table 1. For measurements in which the ions were trapped, the in-trap lift tube was pulsed from the value in Table 1 down to 0 V for the trapping procedure and from this back to the original value for the ejection.

2.2. Laser ion source

A schematic drawing of the laser ion source setup is shown in Fig. 1. It consists of a 25 µm thick tantalum strip, called the filament (F), which can be resistively heated and biased to an electric potential. The strip was folded in a way that a quadratic piece of samarium foil could be inserted, which is passively heated by the tantalum strip due to the physical contact. The filament is placed inside a cylindrical channel (Ch) with a central hole of 3 mm diameter in the endcap. This is followed by three parallel circular metal plates with a central hole of 1 mm diameter for the first two plates and 3 mm diameter for the last one. These plates are used to define the electric field gradient and to cut parts of the beam to reduce angular spread, therefore calling them acceleration aperture (A) 1, 2, and 3 in order of their proximity to the filament. When the filament is heated, the samarium foil releases neutral samarium atoms, as well as Sm^+ and electrons due to surface ionization. The channel including its endcap and the last acceleration aperture are grounded, the filament and the first two acceleration apertures are biased. The applied potentials can be found in Table 1. In this configuration, the emitted electrons are deflected between channel and filament and the surface ionized samarium is deflected between the channel endcap and the first acceleration aperture, leaving only the samarium atoms after the first acceleration aperture. In the centre between the first and second acceleration aperture, two laser beams are overlapped for two-step RIS. Due to the setup only having windows on one axis, the lasers could not be overlapped in a cross-beam geometry but had to be overlapped collinearly in a shallow angle of 1.4° between both beam paths. This results in a cylindrical ionization volume perpendicular to the extraction direction, with a diameter of about 2 mm and a length of several centimetres, where samarium is ionized. The laser system is described in detail in Section 2.3.

Table 1
Voltages applied to the setup electrodes. The names in the electrode row refer to the names shown in Fig. 1.

electrode	Ch	F	A1	A2	A3	EL1	EL2	EL3	M1	M2	M3	M4	M5	M6	D	ITLT
U/V	0	25	3090	3000	0	0	3000	0	−4430	916	714	2090	2575	3066	0	1110

2.3. Laser system

For two-step RIS, two tunable lasers are required. For the first excitation step, which is used for spectroscopy, a narrowband laser is required, while a broadband laser was used for the second, ionizing transition. The narrowband laser system is comprised of a pulsed dye amplifier (PDA, Sirah Lasertechnik) pumped by a high-power single-mode, pulsed, frequency-doubled Nd:YAG laser (PXn300-2-GF-SLM, Edgewave). The PDA was seeded using a tunable, single-mode continuous-wave (cw) dye laser (Matisse, Sirah Lasertechnik) pumped by a cw, frequency-doubled Nd:YAG laser (Millenia, Spectra Physics). The light of the PDA was frequency-doubled using a single-pass second-harmonic generation (SHG) unit utilizing a β-barium borate (BBO) crystal. To obtain the laser light around 330 nm for the first excitation step of samarium, the lasers were operated with 4-Dicyanomethylene-2-methyl-6-p-dimethylaminostyryl-4H-pyran (DCM) in dimethyl sulfoxide (DMSO) for the PDA and DCM in a 1:1 mixture of phenoxyethanol (EPH) and ethylene glycol (EG) for the cw laser. The single-mode operation of the pump laser was required to avoid unwanted excitation caused by side modes [16]. The narrowband system achieved a spectral linewidth of $\delta f_{\mathrm{nb}} = 139(13)$ MHz after SHG, measured using a Fabry–Pérot interferometer (FSR 1 GHz, Toptica) and a pulse width of 5 ns at full-width half-maximum. The broadband laser system is comprised of a pulsed dye laser (Credo, Sirah Lasertechnik) pumped by a frequency-doubled Nd:YAG laser (InnoSlab IS400-2-L, Edgewave). The dye used for the Credo was DCM in Ethanol to produce laser light around 640 nm for the resonant ionization of samarium. The broadband laser system is specified with a linewidth of $\delta f_{\mathrm{bb}} = 1.8$ GHz according to the manual of the company. The pulse width was measured to be 8 ns at full-width half-maximum. A typical spot size for both lasers has a diameter of roughly 2 mm and a pulse energy of 8 µJ for the PDA after SHG and 1 mJ for the CREDO. The combination of laser ionization with a MR-ToF MS based detection without the use of a cooler buncher requires the laser to be synchronized with the MR-ToF MS cycle. The pump lasers can provide repetition rates from 10 kHz down to single shots. They were triggered and synchronized from the same delay generator that controls the MR-ToF and according to the number of revolutions in the MR-ToF MS, the repetition rate of both pulsed pump lasers could be freely adjusted. The wavelength of the lasers during the experiment was measured using a commercial wavemeter (WS7-30, HighFinesse) which was regularly calibrated using a frequency-stabilized helium-neon (HeNe, SIOS) laser.

2.4. RIS on ^{nat}Sm

Laser spectroscopy on $^{\mathrm{nat}}$Sm was performed to demonstrate the operation of ToF-assisted laser spectroscopy and to develop and characterize ionization schemes for application on exotic, short-lived isotopes. In total, six different first-step transitions $\tilde{\nu}_1$ were investigated as summarized in Fig. 2. All of these transitions start from thermally excited levels within the ground state fine structure. Due to the angular momentum being $J = 0$ for the ground state, these excited levels feature a higher population at the evaporation temperature of 1000 °C used during the experiment. The mass spectrum from laser ionized $^{\mathrm{nat}}$Sm is shown in Fig. 3, where the ion count rate as a function of the ToF relative to the laser trigger pulse is plotted. Here, seven different peaks can be clearly distinguished, each of which can be assigned unambiguously to a different isotope of samarium. The ToF spectrum is given in terms of the registered count rate as counts per second (cps) versus the time of flight. The multiscaler has 4096 individual channels with a time resolution of 800 ps. The mass numbers of the natural isotopes of samarium are $A = 144, 147, 148, 149, 150, 152$ and 154, all of which were studied in this work. All ions are extracted with the same electric potentials of a maximum of $U = 3090$ V. With the velocity being described by $v = \sqrt{\frac{2 \cdot q \cdot U}{m}}$, the lightest isotope, ^{144}Sm has the shortest flight time to the detector, and the peaks were assigned to the individual isotopes in ascending order of their mass number. This assignment is supported from the arrival times following the square root of the mass-to-charge ratio. The ToF spectrum does not, however, reflect the relative natural abundance of the isotopes, which is due to the fact that the odd A isotopes have a nuclear spin of $I = 7/2$ giving rise to hyperfine structure and due to fluctuation of the ion source. For laser spectroscopy, the counts in a time-of-flight interval corresponding to an individual Sm isotope, indicated by shaded areas in Fig. 3, were summed for a given wavenumber of the first excitation step. Preparing for laser spectroscopy, suitable autoionizing (AI) resonances were identified for each first excitation step to ensure efficient laser ionization. The width of the AI states was experimentally measured to range from 30 to 90 GHz. Plotting the summed counts against the laser excitation energy for a transition results in the spectra for different isotopes as shown in Fig. 4 exemplary for the transition of scheme 3 of Fig. 2. The achieved spectral resolution amounts to a FWHM of 175(5) MHz. The spectra were fitted by least-square minimization with the SATLAS package [17] in Python. The peaks were modelled as Voigt profiles. The Gaussian and Lorentzian contributions were treated as free parameters without constraints. With this approach, the Lorentzian contribution was found to be negligible, so that the FWHM is dominated by the Gaussian contribution. The main factor for the Gaussian contribution is the laser bandwidth with 139(13) MHz. The other contribution is due to Doppler broadening, arising from the thermal energy of the samarium with the spot size for the ionization. The Doppler broadening was determined to be 36(14) MHz. The nuclear spin I [18], the total angular momentum quantum number J [19–21] of ground and excited atomic states and the hyperfine parameters of the ground states $\mathcal{A}_{\mathrm{l}}$ and $\mathcal{B}_{\mathrm{l}}$, summarized in Table 2, were taken as fixed parameters from literature [22]. The odd mass isotopes have a nuclear spin of $I = 7/2$ and the even mass ones have $I = 0$. From this fitted hyperfine structure, the centroid of the transition and the hyperfine parameter of the upper state $\mathcal{A}_{\mathrm{u}}$ were determined as shown in Table 3. For both isotopes with $I \neq 0$, ^{147}Sm and ^{149}Sm, the ratios of the hyperfine parameters were determined as a consistency check. They are consistent with the ratio obtained from the literature values of the ground states. Slight deviations up to 0.6% can be attributed to hyperfine anomaly. Since not all hyperfine lines were resolved and the isotopes feature small nuclear deformations [23,24], the hyperfine parameter $\mathcal{B}_{\mathrm{u}}$ is expected to be small and could not be determined with the achieved resolution, but is in agreement with being neglectable. For the determination of the uncertainty of the hyperfine parameter $\mathcal{A}$, the response to a value comparable to the ground state contribution was also evaluated. Two excited levels at 30 823.44(2) cm^{-1} and at 31 185.11(1) cm^{-1} were investigated each with two different transitions and the results for their hyperfine parameters show an excellent agreement (c.f. Table 3).

From the centroids of the individual resonances of an isotope with atomic mass number A, the isotope shift was determined relative to the resonance of ^{154}Sm in the same transition by

$$\delta\nu^{154,\mathrm{A}} = \nu^{\mathrm{A}} - \nu^{154}. \tag{1}$$

Here again, a similar isotope shift for transitions to the same excited level is observed. This behaviour is expected, as the ground state fine

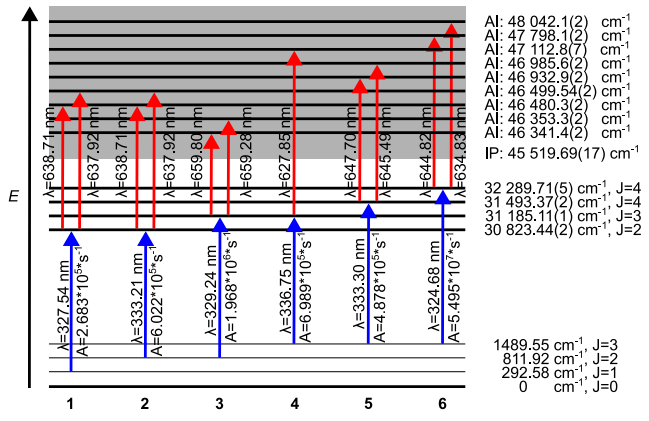

Fig. 2. Level scheme of the measured transitions in samarium. The value of the ionization potential (IP) was taken from [25]. The values of the thermally excited ground states were taken from [26] and the J-values of the levels from [19–21]. They correspond to the electronic configuration of $4f^6 6s^2$. The values of the excited states were determined for ^{154}Sm from adding the wavenumber of the first excitation step (FES) transition $\tilde{\nu}_1^{154}$ and the wavenumber of the second excitation step (SES) transition $\tilde{\nu}_2^{154}$ to the literature value of the ground state. The individual values were converted to a wavelength and are given as the wavelength λ of the transition.

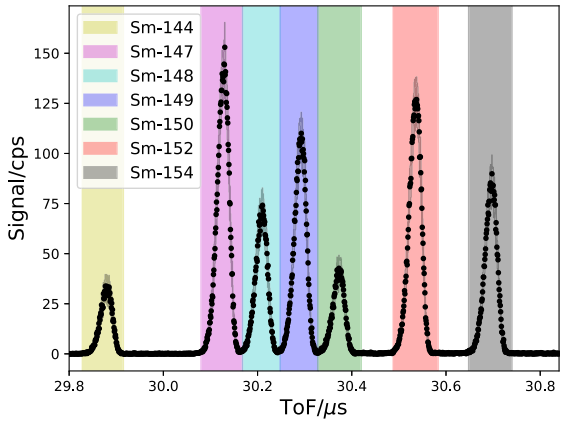

Fig. 3. Sum of all ToF spectra of the samarium isotopes from the measurements of the transition shown in Fig. 4. The shaded areas were used as gates for the respective isotope in the analysis of the laser spectroscopy. The individual peaks show a ToF width (FWHM) of 40 ns.

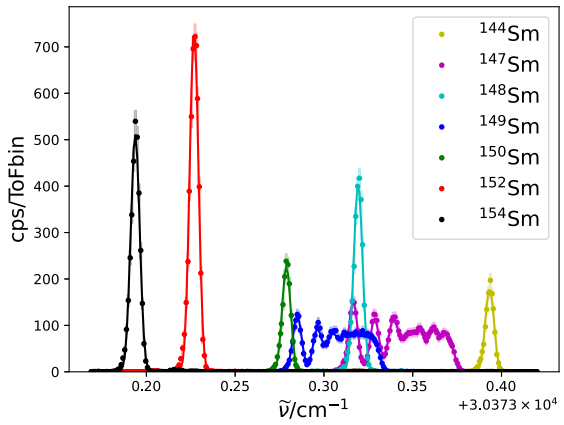

Fig. 4. Optical spectrum of the FES transition of scheme 3 in Fig. 2 for all naturally occurring samarium isotopes. The points show the measured data, while the lines are fits to the data using voigt peak shapes.

Table 2
J-values for the thermally excited ground state levels [19–21], as well as Hyperfine parameters of thermally excited atomic states used in the fit of the spectral data taken from literature [22]. The nuclear spin was taken as $I = 7/2$ for ^{147,149}Sm and as $I = 0$ for the other natural isotopes [18]. The weighted averages of the ratios are $\mathcal{A}_{l,147}/\mathcal{A}_{l,149} = 1.21305(2)$ and $\mathcal{B}_{l,147}/\mathcal{B}_{l,149} = -3.4601(6)$.

E/cm^{-1}	$\mathcal{A}_{l,147}$/MHz	$\mathcal{A}_{l,149}$/MHz	$\mathcal{B}_{l,147}$/MHz	$\mathcal{B}_{l,149}$/MHz	J
292.58	−33.493(2)	−27.610(1)	−58.688(6)	16.963(3)	1
811.92	−41.186(2)	−33.952(2)	−62.229(13)	17.990(13)	2
1489.55	−50.243(2)	−41.418(2)	−33.668(40)	9.746(40)	3

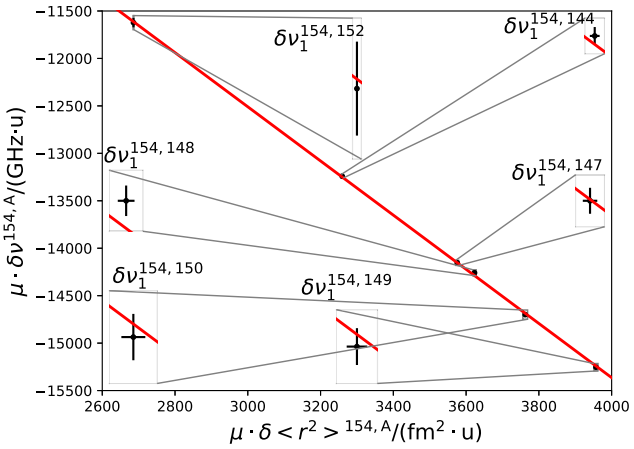

Fig. 5. Kingplot of the samarium isotopes relative to ^{154}Sm for the FES transition of scheme 3 with $\tilde{\nu} = 30\,373.194(1)\,\mathrm{cm}^{-1}$. Uncertainties on the charge radii only take the relative uncertainty given in Ref. [27], while the systematic uncertainty on the absolute charge radii is not included.

structure multiplet is built from the same electron orbitals resulting in a very similar change in electron density within the nucleus when exciting to the same upper level. With these isotope shifts and the relative mean-square charge radii $\delta < r^2 >^{A,A'}$ [27], taken from literature, a Kingplot analysis [28] was performed according to

$$\mu \cdot \delta\nu^{A,A'} = K + F_s \cdot \mu \cdot \delta < r^2 >^{A,A'}, \tag{2}$$

where μ is the reduced mass given by

$$\mu = \frac{M_A M_{A'}}{M_A - M_{A'}}. \tag{3}$$

With these relations, the mass shift K and the field shift F_s were determined for the respective transition. The results are summarized in Table 3. One exemplary Kingplot can be seen in Fig. 5. To determine changes in nuclear mean-square charge radii, excitation schemes 1 and 2 will be the most suitable since they provide the largest isotope shift, making them the most sensitive to changes in nuclear size. These schemes, leading to the same first excited level, feature also the largest HFS splitting and sensitivity to nuclear magnetic dipole moments. The spectral resolution was insufficient to be sensitive to small contributions related to a non-zero spectroscopic quadrupole moment Q_s. For simultaneous production of a wide range of isotopes, excitation scheme 5 can be used since it has the smallest isotope shift.

3. The JetRIS system and future extensions

The schematic layout of the JetRIS setup with the future integration of the MR-ToF MS is shown in Fig. 6. The nuclides of interest are produced in fusion-evaporation reactions and separated from the high intensity primary beam using the **S**eperator for **H**eavy **I**on reaction **P**roducts (SHIP) [29,30]. Recoil ions with different charge states enter the gas cell through a thin entrance window where they are stopped

Table 3
Results of the spectroscopy of ^{nat}Sm. The FES of schemes 1 and 2, as well as 3 and 4 result in the same atomic level, which gives them the same SES.

Scheme	$\tilde{\nu}_1^{154}$/cm^{-1}	$\delta\nu_1^{154,152}$/MHz	$\delta\nu_1^{154,150}$/MHz	$\delta\nu_1^{154,149}$/MHz	$\delta\nu_1^{154,148}$/MHz	$\delta\nu_1^{154,147}$/MHz	$\delta\nu_1^{154,144}$/MHz	$\mathcal{A}_{u,149}$/MHz	$\mathcal{A}_{u,147}$/MHz	$\mathcal{A}_{u,147}/\mathcal{A}_{u,149}$	K/(GHz·u)	F_s/(GHz/fm^2)	$\tilde{\nu}_2$/cm^{-1}
1	30 530.852(1)	1268(42)	3454(42)	4533(42)	5043(42)	5858(42)	7852(42)	−158.1(5)	−193.4(4)	1.223(3)	−2125(247)	−4.70(7)	15 676.10(1)
													15 656.84(8)
2	30 011.536(1)	1262(42)	3445(42)	4536(42)	5052(42)	5870(42)	7861(42)	−158.4(8)	−192.7(5)	1.217(4)	−1945(108)	−4.75(3)	
3	30 373.194(1)	995(42)	2551(42)	3331(42)	3762(42)	4386(42)	5984(42)	−78.7(2)	−96.1(2)	1.221(3)	−3946(65)	−2.85(2)	15 156.25(8)
													15 168.22(6)
4	29 695.557(1)	995(42)	2569(42)	3367(42)	3798(42)	4446(42)	6017(42)	−79.7(16)	−96.0(13)	1.20(2)	−3608(144)	−2.98(4)	15 927.7(7)
5	30 003.823(1)	651(42)	1559(42)	2003(42)	2302(42)	2689(42)	3750(42)	−107.4(2)	−130.1(2)	1.211(2)	−4234(111)	−1.25(3)	15 492.26(3)
													15 439.56(9)
6	30 800.159(1)	1100(42)	2908(42)	3810(42)	4293(42)	5001(42)	6793(42)	−114.9(4)	−140.3(3)	1.221(4)	−3193(168)	−3.61(5)	15 752.4(2)
													15 508.41(1)

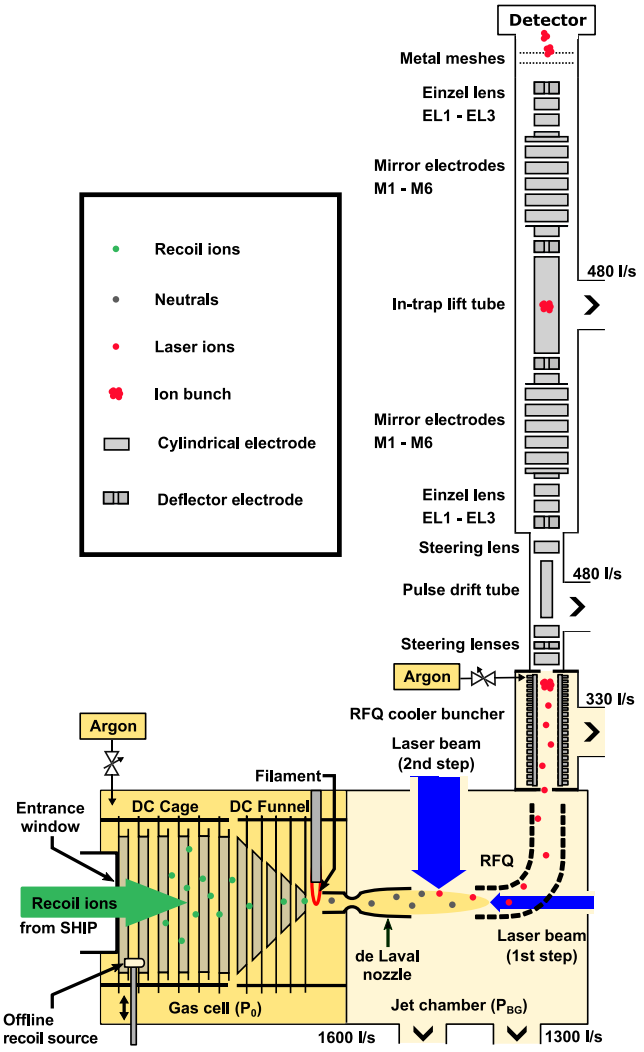

Fig. 6. Schematic overview of the envisioned full setup of JetRIS with the addition of the cooler buncher, pulsed drift tube and MR-ToF MS. The length of the setup along the JetRIS is 0.7 m, the side to the MR-ToF is 2.2 m.

and thermalized in argon buffer gas at 80 mbar of pressure. Most of the recoil ions remain in a singly charged state. Multiple electrodes surrounding this stopping volume guide the ions via an electric field towards a 125 µm thin tantalum wire, referred to as a filament, which is resistively heated to approximately 1200 °C, depending on the element under investigation [31]. The contact with the filament neutralizes and adsorbs the ions and the heat ensures desorption from the filament. After evaporation, the atoms are transported by gas flow through a de-Laval type nozzle towards the low pressure jet cell. This nozzle forms a low-pressure, low-temperature, hypersonic gas jet. The jet shape and the appropriate background pressures in the jet cell have been investigated in detail [32,33]. Within the gas jet region two laser beams are overlapped in cross-beam geometry, where the FES)' is anticollinear to the gas jet and the SES is in perpendicular configuration, performing two-step RIS. The conditions inside the gas jet feature a negligible pressure broadening and a low Doppler broadening enabling spectral linewidths of 211(35) MHz [33] under optimal conditions. Nevertheless, the velocity of the ions from the gas expansion is about 550 m/s [34]. With the interaction region being 60 mm long, a laser repetition rate of 10 kHz is required for efficient laser interaction. The produced laser ions are transported via a 90° bend radio frequency quadrupole (RFQ) structure into the next vacuum chamber. Presently, a silicon detector is used in high vacuum conditions for alpha-decay detection [5]. This configuration is suitable for α-decaying nuclides with half-lives of more than 0.2 s. Measurements of long half-lives in the range of hours are possible but time consuming.

3.1. Design characteristics of the JetRIS cooler buncher

For the integration of the MR-ToF MS into JetRIS, as seen in Fig. 6, a radio frequency cooler buncher is required to collect and bunch the laser ions. In addition, the buncher ensures well-defined initial conditions for longitudinal and transversal emittance of the ion beam, which is mandatory for a high mass resolving power, while maintaining high efficiency. The layout of the cooler buncher was inspired by the design used at GANIL for the S^3-LEB setup [35], along with a pulsed drift section to accelerate the ion bunches to the kinetic energy of 3 keV needed to enter the MR-ToF MS, and is schematically shown in Fig. 6. The cooler buncher consists of a linear, 345 mm long RFQ, in which 4 times 20 plate electrodes are inserted in between the RFQ rods in order to create a DC-potential well to trap the ions, forming 20 segments along the RFQ. The first 12 segments with a linear potential gradient of the cooling section are 19 mm long, while the remaining eight segments, forming the actual potential well are 9 mm long to achieve a well-defined location of the ion bunch at the second last electrode. The last four electrodes from the buncher can be switched in potential to eject the ions towards the MR-ToF MS. The following pulsed drift section will be in high vacuum by means of an orifice acting as pumping barrier. It is composed of an einzel lens, the drift tube and an electrode at ground potential at its exit. The middle electrode of the einzel lens is azimuthally 4-fold segmented, serving as a deflector, allowing for correction of the ion trajectories. As JetRIS is operated with argon buffer gas, the cooler buncher was investigated for operation with argon as well. Ion trajectory simulations with SIMION 8.1 have been conducted to estimate the performance and properties of the cooler buncher. The electrodes were modelled with a 0.2 mm grid size. The interaction with the argon buffer gas atoms in the bunching section were modelled as elastic hard sphere collisions using the collision_hs1 library of SIMION. To determine an optimal argon gas pressure, simulations were conducted from $5.0 \cdot 10^{-4}$ mbar to $4.0 \cdot 10^{-3}$ mbar, for 10 and 100 ms storage time. Both storage times show similar behaviour for the pressure dependence, while the longer storage time is slightly better in efficiency as shown in Fig. 7. The best transmission efficiency of $\epsilon = 0.79(5)$ was found at a pressure of $p = 1.0 \cdot 10^{-3}$ mbar for 100 ms storage time. Further analysis also

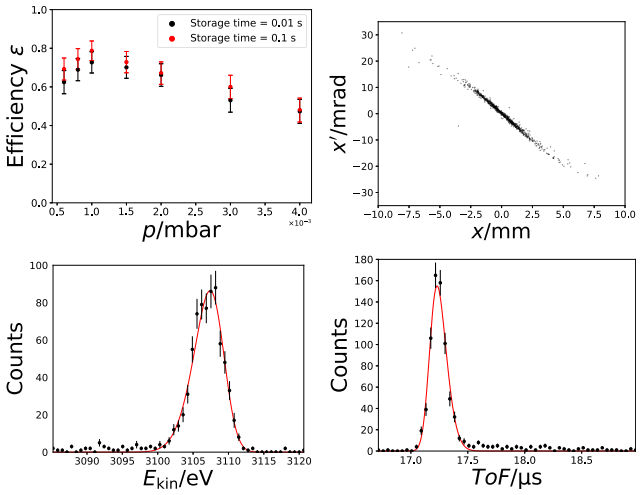

Fig. 7. Upper left: Simulated Transmission efficiency ϵ of the cooler buncher in bunching mode and the pulsed drift tube as a function of the residual gas pressure in the cooler buncher for two storage times of 10 ms (black) and 100 ms (red). Upper right: Simulated transversal emittance of the ions from the cooler buncher, after the pulsed drift tube. The emittance is the same in both axis due to the symmetry of the setup. Lower figures: Simulated distributions of kinetic energy (left) and ToF (right) after the pulsed drift tube for a pressure of $p = 1.0 \cdot 10^{-3}$ mbar and 100 ms storage time. The data points were fitted using skewed gaussian distributions (red line) [36].

highlights this value as optimal in terms of kinetic-energy and time-of-flight distributions which are shown in the lower panels of Fig. 7. Here, an energy spread of $\Delta E_{\mathrm{kin}} = 5.0(4)$ eV and a ToF width of $\Delta t = 172(14)$ ns were determined.

3.2. Ion-source characterization

Since the performance of the MR-ToF MS depends on the quality of the injected ion beam, it is also necessary to characterize the ion beam produced by the source and its ion-optical components. The mean longitudinal kinetic energy E_{kin}, the energy spread ΔE_{kin} and the ToF width were determined and optimized experimentally, while the transversal emittance was estimated from simulations using SIMION 8.1. During the optimization of the ion-source parameters, ions were only transmitted through the MR-ToF MS and not trapped. For the kinetic energy measurement, the potential applied to the metallic mesh in front of the detector was varied close to the kinetic energy of the ions acting as an energy filter. The mean energy of the ions was determined as $E_{\mathrm{kin}} = 3063.4(2)$ eV which is in agreement with the ionization region being located between A1(3000 V) and A2(3090 V). Assuming a Gaussian distribution of the kinetic energies an energy spread of $\Delta E_{\mathrm{kin}} = 25(1)$ eV was determined. In the simulations, the distribution was assumed to be evenly distributed inside the starting volume of the ions. Measured ToF spectra are shown in the top left panels of Fig. 8 (black data points), for an increasing number of revolutions. The left peak in the upper panel was fitted using a Gaussian giving a ToF distribution of 121(1) ns. The second peak can be attributed to ions generated from the same isotope, but with a slower extraction from the ionization volume due to their position on the outer edge of the volume. Simulations are also shown from which it becomes apparent that the existence of multiple ToF peaks is inherent to the design of this source. This is attributed to the large, cylindrical, ionization volume, in which ions further away from the central axis are transported slower towards the accelerating potential. The simulations were done with a 0.1 mm grid size and are based on a cylindrical starting volume of the ions with a diameter of 2 mm and a length of 5 mm orthogonal to the central axis of the setup. This resembles the conditions of the

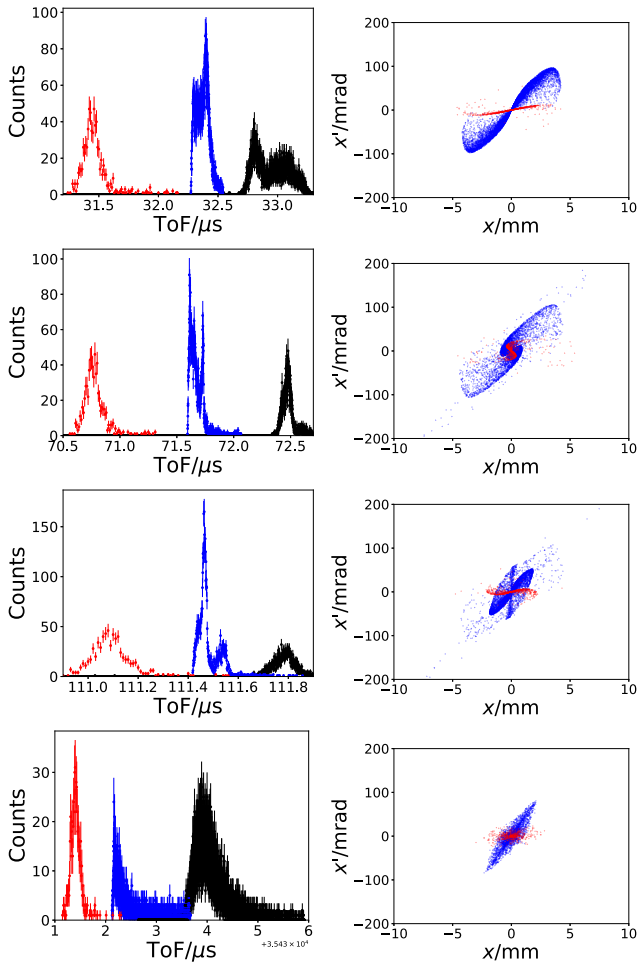

Fig. 8. Simulated and measured ToF spectra in transmission (first), after one revolution (second), two revolutions (third) and 900 revolutions (bottom) with a plot of the corresponding transversal emittance for the simulations. The black data points are from measured data, the blue from simulations with the laser ion source and the red from simulations using the cooler buncher ions. The data points of the simulations were taken at a position corresponding to the location of the detector in the measurements. The ion species simulated were singular positively charged ions with a mass of 154 u. For visibility purposes the simulated spectra were moved on the ToF axis.

experimental ionization volume resulting from the overlapping laser beams. The mass of the ions was set to be 154 u. The ions were given a starting kinetic energy of 190 meV, based on a temperature of 1200 °C, with a cone distribution in the direction of the MR-ToF MS with a half angle of 5°. Simulations for a point-like ionization volume never showed the behaviour of multiple peaks in the ToF spectrum. Fig. 8 shows in addition the transversal emittance for increasing number of turns in the MR-ToF. The time structure changes significantly, thus pointing towards the need for better defined emittance of the beam entering the MR-ToF. The experimental results shown in this article were acquired over a span of several months. The performance of the ion-source depends strongly on the laser beam positions and diameters. Changes in these may have led to the situation that a second peak from the same isotope in the ToF spectrum was not present in every experiment.

3.3. MR-ToF MS characterization

In addition to the time structure, the behaviour with respect to the relative efficiency ϵ and mass resolving power R was investigated. For

this purpose, the ions were trapped for different numbers of revolutions and the ToF signal after ejection was evaluated. For the efficiency determination, the number of ions reaching the detector is analysed as a function of the number of revolutions. The efficiency for every dataset is normalized to the respective efficiency in transmission mode. As can be seen in Fig. 9, the measured relative efficiency ϵ drops in all cases quite steeply in the first few revolutions and begins to settle after about 100 revolutions. The experimental results show the largest drop and settle at about 20%, while the simulations with the laser ion source settle to about 35%. The difference can be attributed to deviations of the ion beam from the central axis. This assumption is supported from the observation of some periodic staggering in the obtained efficiency for more than 200 revolutions indicating spatial oscillations of the ion trajectory within the MR-ToF MS. This staggering effect is known in the collaboration and arises from the path of the ions not being a perfectly closed trajectory inside the MR-ToF MS but it moving slowly over the number of revolutions originating different trajectories of ions while exiting the MR-ToF MS. When comparing the emittances in Fig. 8, the loss of efficiency visible in the top part of Fig. 9 can be generally explained by a too large transversal emittance of the injected ion beam. This was cross checked in another simulation for ions with a Gaussian ToF and energy distribution. This follows the measured distribution (c.f. Section 3.2), while transversal emittance was set to zero. This simulation was done up until 100 revolutions showing no ion loss. As seen in Fig. 8 the ToF spectrum with one revolution features multiple peaks. For an increasing number of revolutions the intensity ratio between the ToF peak with the highest intensity and the other ones shifts in favour of the former. This indicates that from the multiple existing ToF components there is one favoured due to it having the lowest transversal emittance. Since this is the only ToF components persisting, it can be assumed that most, if not all, of the losses can be attributed to these other higher-emittance ToF components.

The emittance figures in Fig. 8 were all taken at the same position, which is the location of the detector in the real setup. The emittance from the simulated laser ion source reveals multiple different patterns within itself over the course of the revolutions. After 900 revolutions there is only one pattern visible. The evolution of the emittance shows a change in shape for both the ions from the laser ion source (blue), as well as the ones from the cooler buncher (red). This shows that there are some changes in ion trajectory and therefore the path and angle at which they get ejected out of the MR-ToF MS over the course of multiple revolutions. For the red emittance, the overall volume remains nearly constant throughout its evolution, whereas the volume of the blue emittance shrinks significantly until the end. After 900 revolutions, which is already beyond the point of ion losses, both emittances look similar in shape, albeit being rotated with respect to one another.

From the ToF spectra, the mass resolving power R was determined as a function of the number of revolutions as shown in the lower part of Fig. 9. It is defined as $R = \frac{m}{\Delta m} = \frac{t}{2\Delta t}$. Due to the appearance of multiple peaks, the standard deviation σ_{ToF} of the obtained ToF was calculated. For the mass resolving power, $\Delta t = 2\sqrt{2 \cdot \ln 2} \cdot \sigma_{\mathrm{ToF}}$ was assumed. The highest experimentally achieved mass resolving power was approximately 25 000, which was limited due to a broadening of the peaks and an asymmetric peak shape, which was also observed in the simulations. The simulations with ions from the cooler buncher resulted in well-defined singular peaks visible in each ToF spectrum, corresponding to a mass resolving power of 100 000 with a maximum at 4000 revolutions For a species with a mass of 154 u, this would lead to a total ToF of 157.5 ms.

Fig. 10 illustrates the possibility of in-trap beam purification via the in-trap deflector electrodes. Here, the laser for the FES was set to 30 373.1280 cm^{-1} at which the isotopes ^{147}Sm, ^{148}Sm and ^{149}Sm have been ionized simultaneously. A mixed ion sample containing these isotopes was injected into the MR-ToF MS and trapped. The timing for the in-trap lift for the ejection was set so that ^{148}Sm was ejected

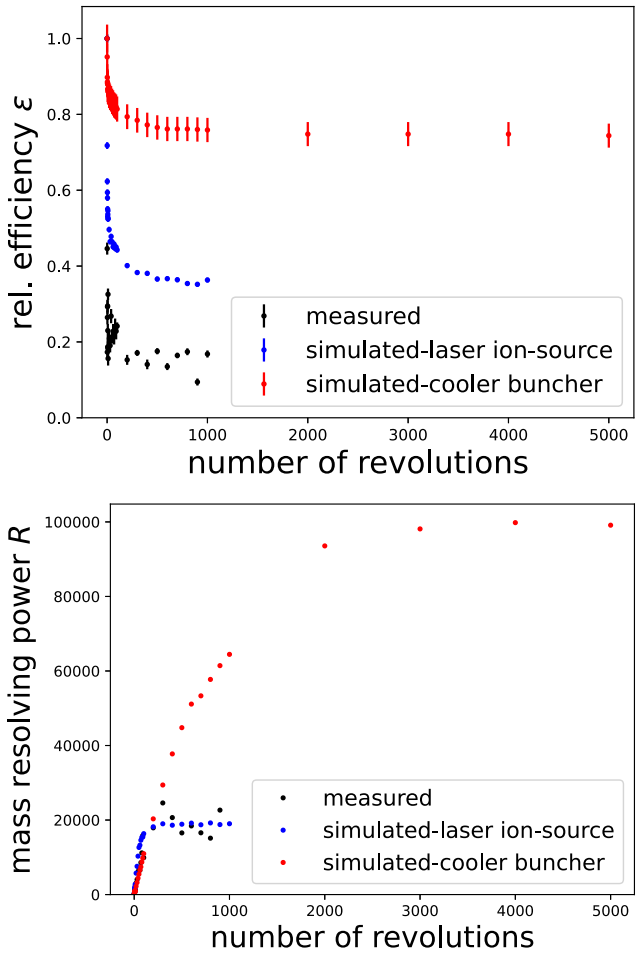

Fig. 9. Top: Efficiency ϵ relative to the number of transmitted ions without trapping of the MR-ToF MS for different number of revolutions. Bottom: Mass resolving power R of the MR-ToF MS against the number of revolutions. The experimental data (black) is compared to the simulated ion source (blue) and the expected behaviour with the cooler buncher (red). The given errorbars are statistical uncertainties from the measured counts or the number of investigated ions, respectively.

after 300 revolutions, which in turn led ^{147}Sm being ejected after 301 revolutions and ^{149}Sm after 299 revolutions, as shown in the left panel of Fig. 10 with all isotopes visible in the ToF window. After 57.833 µs in the MR-ToF, which is half of the full trapping time, ^{148}Sm finished an integer number of revolutions, while the other two isotopes finished half a revolution, leading to a maximum spacial separation between the even mass isotope and the odd mass ones. At this time, the top segment of deflector electrode at the side of the odd mass isotopes was pulsed from 0 V to 100 V for 1 µs. This leads to the result shown in the right panel of Fig. 10 where only the peak of ^{148}Sm is visible, while the other two peaks are removed.

4. Conclusion

Using ToF-assisted resonance ionization laser spectroscopy, multiple laser excitation schemes of samarium were developed and investigated. Here, the mass and field shift constants were determined as well as the hyperfine parameter $\mathcal{A}$ for the excited states in the odd mass numbered isotopes. This provides a basis for on-line laser spectroscopy experiments on neutron-deficient samarium isotopes using the JetRIS technique. Furthermore, first characterizations of an MR-ToF MS for JetRIS were done utilizing a pulsed laser ion source, showing the

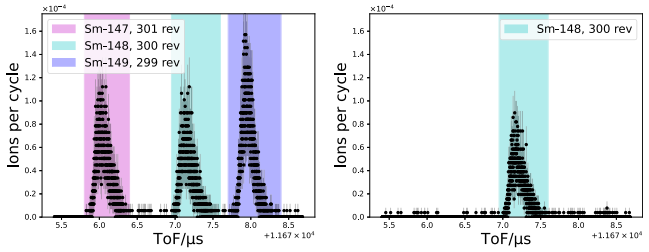

Fig. 10. Measured ToF spectra using the deflector electrodes for beam purification. The left figure shows three peaks which were attributed to ^{147}Sm, ^{148}Sm and ^{149}Sm from left to right. The right figure shows the same spectrum while ^{147}Sm and ^{149}Sm were deflected during the trapping time. The change in intensity of ^{148}Sm in both figures is attributed to a change in intensity of the ion source.

potential of combining these two techniques. While this combination still showed caveats in the performance regarding achieved efficiencies and ToF structure, and thus on the mass resolving power, a clear path towards the final integration of the MR-ToF into the JetRIS setup is given with the usage of a cooler buncher for which the design is reported in this work. This upgraded setup will extend the reach of on-line laser spectroscopy experiments to heavy nuclei independent of their decay mode and give access to long-lived nuclides. An interesting nuclide that will become accessible with this setup is ^{254}Md as well as the aforementioned neutron-deficient samarium isotopes.

CRediT authorship contribution statement

Danny Münzberg: Writing – review & editing, Writing – original draft, Visualization, Project administration, Investigation - Laser spectroscopy & Mass spectrometry, Data analysis - Laser spectroscopy & Mass spectrometry, Conceptualization. **Alexandre Brizard:** Writing – review & editing, Investigation - Cooler buncher, Data analysis - Cooler buncher. **Tim van de Vendel:** Writing – review & editing, Investigation - Cooler buncher, Data analysis - Cooler buncher. **Jana Weyrich:** Writing – review & editing, Investigation - Mass spectrometry, Data analysis - Laser spectroscopy & Mass spectrometry. **Michael Block:** Writing – review & editing, Supervision, Resources, Funding acquisition. **Julia Even:** Writing – review & editing, Resources. **Christian Helmel:** Writing – review & editing, Investigation - early stages mass spectrometry. **Nathalie Lecesne:** Writing – review & editing, Resources. **Sebastian Raeder:** Writing – review & editing, Data analysis. **Daniel Rodríguez:** Writing – review & editing, Investigation - early stages Mass spectrometry. **Hervé Savajols:** Writing – review & editing, Resources. **Klaus Wendt:** Writing – review & editing, Resources, Funding acquisition.

Declaration of competing interest

The authors declare that they have no known competing financial interests or personal relationships that could have appeared to influence the work reported in this paper.

Acknowledgements

We gratefully acknowledge the help of the mechanical workshop of the physics institute of the JGU Mainz. This work has been supported by the Bundesministerium für Bildung und Forschung (BMBF, Germany) under project numbers 05P18UMCIA and 05P21UMFN3. T.v.d.V. acknowledges support from the EU Erasmus+ programme, the GET_INvolved Programme of FAIR/GSI GmbH, Darmstadt, Germany and the Marco Polo fund of the University of Groningen, Netherlands and the Bundesministerium für Bildung und Forschung (BMBF, Germany) under grant number 05P21RDFN1. DR acknowledges financial support from the HIM Guest Scientist Program, Germany and from Grant No. PID2022-141496NB-I00 funded by MICIU/AEI/10.13039/501100011033, Germany and by ERDF/EU.

Data availability

Data will be made available on request.

References

[1] Witold Nazarewicz, The limits of nuclear mass and charge, Nat. Phys. (ISSN: 1745-2473) 14 (6) (2018) 537–541, http://dx.doi.org/10.1038/s41567-018-0163-3.

[2] S.A. Giuliani, Z. Matheson, W. Nazarewicz, E. Olsen, P.-G. Reinhard, J. Sadhukhan, B. Schuetrumpf, N. Schunck, P. Schwerdtfeger, Colloquium : Superheavy elements: Oganesson and beyond, Rev. Modern Phys. (ISSN: 0034-6861) 91 (1) (2019) 011001, http://dx.doi.org/10.1103/RevModPhys.91.011001.

[3] Odile R. Smits, Christoph E. Düllmann, Paul Indelicato, Witold Nazarewicz, Peter Schwerdtfeger, The quest for superheavy elements and the limit of the periodic table, Nat. Rev. Phys. 6 (2) (2024) 86–98, http://dx.doi.org/10.1038/s42254-023-00668-y.

[4] S. Raeder, M. Block, P. Chhetri, R. Ferrer, S. Kraemer, T. Kron, M. Laatiaoui, S. Nothhelfer, F. Schneider, P. van Duppen, M. Verlinde, E. Verstraelen, Th. Walther, A. Zadvornaya, A gas-jet apparatus for high-resolution laser spectroscopy on the heaviest elements at SHIP, Nucl. Instrum. Methods Phys. Res. Sect. B: Beam Interactions Mater. Atoms (ISSN: 0168583X) 463 (2020) 272–276, http://dx.doi.org/10.1016/j.nimb.2019.05.016.

[5] Jeremy Lantis, Arno Claessens, Danny Münzberg, Julian Auler, Michael Block, Premaditya Chhetri, Christoph E. Düllmann, Rafael Ferrer, Francesca Giacoppo, Manuel J. Gutiérrez, Fedor Ivandikov, Oliver Kaleja, Tom Kieck, EunKang Kim, Mustapha Laatiaoui, Nathalie Lecesne, Vladimir Manea, Steven Nothhelfer, Sebastian Raeder, Jekabs Romans, Elisa Romero-Romero, Antoine de Roubin, Hervé Savajols, Simon Sels, Matou Stemmler, Piet van Duppen, Thomas Walther, Jessica Warbinek, Klaus Wendt, Alexander Yakushev, Alexandra Zadvornaya, In-gas-jet laser spectroscopy of No254 with JetRIS, Phys. Rev. Res. 6 (2) (2024) 023318, http://dx.doi.org/10.1103/PhysRevResearch.6.023318.

[6] Jiguang Li, Vladimir Dzuba, Theoretical study of the spectroscopic properties of mendelevium (z=101), J. Quant. Spectrosc. Radiat. Transfer (ISSN: 00224073) 247 (2020) 106943, http://dx.doi.org/10.1016/j.jqsrt.2020.106943.

[7] Mustapha Laatiaoui, Sebastian Raeder, Laser spectroscopy of the heaviest elements: One atom at a time, Nucl. Phys. News (ISSN: 1061-9127) 29 (1) (2019) 21–25, http://dx.doi.org/10.1080/10619127.2019.1571804.

[8] J. Magill, R. Dreher, Zs. Sóti, Karlsruher nuklidkarte, 11. Auflage, Nucleonica GmbH and Marktdienste Haberbeck GmbH, Karlsruhe and Lage, ISBN: 978-3-00-069180-5, 2022.

[9] M. Schlaich, J. Fischer, P. Fischer, C. Klink, A. Obertelli, A. Schmidt, L. Schweikhard, F. Wienholtz, A multi-reflection time-of-flight mass spectrometer for the offline ion source of the PUMA experiment, Int. J. Mass Spectrom. (ISSN: 13873806) 495 (2024) 117166, http://dx.doi.org/10.1016/j.ijms.2023.117166.

[10] Steven Nothhelfer, Advances in laser spectroscopy of superheavy elements: Resonance ionization spectroscopy on 253,254,255Es and a new gas-jet based high-resolution spectroscopy setup (Ph.D. thesis), Johannes Gutenberg-Universität Mainz, 2022, http://dx.doi.org/10.25358/openscience-6958.

[11] X.F. Yang, S.J. Wang, S.G. Wilkins, R. GarciaF. Ruiz, Laser spectroscopy for the study of exotic nuclei, Prog. Part. Nucl. Phys. (ISSN: 01466410) 129 (2023) 104005, http://dx.doi.org/10.1016/j.ppnp.2022.104005.

[12] R. Pengo, D. Evers, K.E.G. Löbner, U. Quade, K. Rudolph, S.J. Skorka, I. Weidl, Nuclear structure effects in sub-barrier fusion cross sections, Nucl. Phys. A (ISSN: 03759474) 411 (2) (1983) 255–274, http://dx.doi.org/10.1016/0375-9474(83)90392-5.

[13] David A. Dahl, Simion for the personal computer in reflection, Int. J. Mass Spectrom. (ISSN: 13873806) 200 (1–3) (2000) 3–25, http://dx.doi.org/10.1016/S1387-3806(00)00305-5.

[14] Palmer, SIMION 8, 2020, URL https://simion.com.

[15] F. Wienholtz, S. Kreim, M. Rosenbusch, L. Schweikhard, R.N. Wolf, Mass-selective ion ejection from multi-reflection time-of-flight devices via a pulsed in-trap lift, Int. J. Mass Spectrom. (ISSN: 13873806) 421 (2017) 285–293, http://dx.doi.org/10.1016/j.ijms.2017.07.016.

[16] M. Verlinde, R. Ferrer, A. Claessens, C.A. Granados, S. Kraemer, Yu Kudryavtsev, D. Li, P. van den Bergh, P. van Duppen, E. Verstraelen, Single-longitudinal-mode pumped pulsed-dye amplifier for high-resolution laser spectroscopy, Rev. Sci. Instruments 91 (10) (2020) 103002, http://dx.doi.org/10.1063/5.0017985.

[17] W. Gins, R.P. de Groote, M.L. Bissell, C. Granados Buitrago, R. Ferrer, K.M. Lynch, G. Neyens, S. Sels, Analysis of counting data: Development of the SATLAS python package, Comput. Phys. Comm. (ISSN: 00104655) 222 (2018) 286–294, http://dx.doi.org/10.1016/j.cpc.2017.09.012.

[18] G. Audi, O. Bersillon, J. Blachot, A.H. Wapstra, The nubase evaluation of nuclear and decay properties, Nucl. Phys. A (ISSN: 03759474) 729 (1) (2003) 3–128, http://dx.doi.org/10.1016/j.nuclphysa.2003.11.001.

[19] Walter Albertson, The arc spectrum of samarium and gadolinium. Normal electron configurations of the rare earths, Phys. Rev. (ISSN: 0031-899X) 47 (5) (1935) 370–376, http://dx.doi.org/10.1103/PhysRev.47.370.

[20] William Meggers, Charles Corliss, Bourdon Scribner, second ed., Tables of Spectral-Line Intensities Part I - Arranged by Elements, vol. 1, U.S. Department of commerce, National Bureau of Standards, 1975, URL https://digital.library.unt.edu/ark:/67531/metadc13183/m2/1/high_res_d/NBS%20Monograph%20145%20Part1.pdf.

[21] H. ehкh, B.A. Komapobcкй, C[icy][lcy]Oc[tscy][icy][lcy][lcy][yacy]topob c[Pi]ektpa[lcy]ьh[ьix][lcy][icy]h[icy]й [icy] bpemeha [zhcy][icy]зh[icy]boзБy[zhcy][dcy]ehhьix cocToЯh[icy]й atomob pe[dcy]Koзeme[lcy]ьhьix [ecy][lcy]emehtob c [dcy]octpa[icy]ba[YUcy]щейcЯ 4f-oБo[lcy]oкKoй, J. Quant. Spectrosc. Radiat. Transfer (ISSN: 00224073) 16 (3) (1976) 217–252, http://dx.doi.org/10.1016/0022-4073(76)90066-2.

[22] W.J. Childs, L.S. Goodman, Reanalysis of the hyperfine structure of the 4f66s2F7 multiplet in Sm147,149 , including measurements for the F67 state, Phys. Rev. A (ISSN: 0556-2791) 6 (6) (1972) 2011–2021, http://dx.doi.org/10.1103/PhysRevA.6.2011.

[23] Ninel Nica, Balraj Singh, Nuclear data sheets for A=147, Nucl. Data Sheets (ISSN: 00903752) 181 (2022) 1–474, http://dx.doi.org/10.1016/j.nds.2022.03.001.

[24] Balraj Singh, Jun Chen, Nuclear structure and decay data for A=149 isobars, Nucl. Data Sheets (ISSN: 00903752) 185 (2022) 2–559, http://dx.doi.org/10.1016/j.nds.2022.10.001.

[25] X.U. Zhao-jin, Zhang Xiao-hu, Zhang Wen-na, Huang Chao-hong, Shen Li, Shift of the first ionization threshold of sm atom in electric field, Chin. Opt. (ISSN: 2095-1531) 13 (6) (2020) 1385–1400, http://dx.doi.org/10.37188/CO.2020-0071.

[26] W.C. Martin, Romuald Zalubas, Lucy Hagan, Atomic Energy Levels - the Rare-Earth Elements, National Bureau of Standards, Gaithersburg, MD, 1978, http://dx.doi.org/10.6028/NBS.NSRDS.60.

[27] H. Brand, B. Seibert, A. Steudel, Laser-atomic-beam spectroscopy in sm: Isotope shifts and changes in mean-square nuclear charge radii, Z. Phys. Atoms Nucl. (ISSN: 0340-2193) 296 (4) (1980) 281–286, http://dx.doi.org/10.1007/BF01438521.

[28] Wilfried Nörtershäuser, Christopher Geppert, Nuclear charge radii of light elements and recent developments in collinear laser spectroscopy, in: Christoph Scheidenberger, Marek Pfützner (Eds.), The Euroschool on Exotic Beams, Vol. IV, in: Lecture Notes in Physics, vol. 879, Springer Berlin Heidelberg, Berlin, Heidelberg, ISBN: 978-3-642-45140-9, 2014, pp. 233–292, http://dx.doi.org/10.1007/978-3-642-45141-6{_}6.

[29] G. Münzenberg, W. Faust, S. Hofmann, P. Armbruster, K. Güttner, H. Ewald, The velocity filter ship, a separator of unslowed heavy ion fusion products, Nucl. Instrum. Methods (ISSN: 0029554X) 161 (1) (1979) 65–82, http://dx.doi.org/10.1016/0029-554X(79)90362-8.

[30] Michael Block, Francesca Giacoppo, Fritz-Peter Heßberger, Sebastian Raeder, Recent progress in experiments on the heaviest nuclides at SHIP, La Riv. Del Nuovo Cimento (ISSN: 0393-697X) 45 (4) (2022) 279–323, http://dx.doi.org/10.1007/s40766-022-00030-5.

[31] H. Backe, P. Kunz, W. Lauth, A. Dretzke, R. Horn, T. Kolb, M. Laatiaoui, M. Sewtz, D. Ackermann, M. Block, F. Herfurth, F.P. Heßberger, S. Hofmann, R. Mann, Towards optical spectroscopy of the element nobelium (z= 102) in a buffer gas cell, Eur. Phys. J. D (ISSN: 1434-6060) 45 (1) (2007) 99–106, http://dx.doi.org/10.1140/epjd/e2007-00198-1.

[32] R. Ferrer, M. Verlinde, E. Verstraelen, A. Claessens, M. Huyse, S. Kraemer, Yu. Kudryavtsev, J. Romans, P. van den Bergh, P. van Duppen, A. Zadvornaya, O. Chazot, G. Grossir, V.I. Kalikmanov, M. Nabuurs, D. Reynaerts, Hypersonic nozzle for laser-spectroscopy studies at 17 K characterized by resonance-ionization-spectroscopy-based flow mapping, Phys. Rev. Res. 3 (4) (2021) 043041, http://dx.doi.org/10.1103/PhysRevResearch.3.043041.

[33] Danny Münzberg, Michael Block, Arno Claessens, Rafael Ferrer, Mustapha Laatiaoui, Jeremy Lantis, Steven Nothhelfer, Sebastian Raeder, Piet van Duppen, Resolution characterizations of JetRIS in mainz using 164Dy, Atoms 10 (2) (2022) 57, http://dx.doi.org/10.3390/atoms10020057.

[34] Yu. Kudryavtsev, P. Creemers, R. Ferrer, C. Granados, L.P. Gaffney, M. Huyse, E. Mogilevskiy, S. Raeder, S. Sels, P. van den Bergh, P. van Duppen, A. Zadvornaya, A new in-gas-laser ionization and spectroscopy laboratory for off-line studies at KU leuven, Nucl. Instrum Methods Phys. Res. Sect. B: Beam Interactions Mater. Atoms (ISSN: 0168583X) 376 (2016) 345–352, http://dx.doi.org/10.1016/j.nimb.2016.02.040.

[35] Anjali Ajayakumar, Jekabs Romans, Martial Authier, Yazeed Balasmeh, Alexandre Brizard, Frederic Boumard, Lucia Caceres, Jean-Francois Cam, Arno Claessens, Samuel Damoy, Pierre Delahaye, Philippe Desrues, Wenling Dong, Antoine Drouart, Patricia Duchesne, Rafael Ferrer, Xavier Fléchard, Serge Franchoo, Patrice Gangnant, Sarina Geldhof, Ruben P. de Groote, Fedor Ivandikov, Nathalie Lecesne, Renan Leroy, Julien Lory, Franck Lutton, Vladimir Manea, Yvan Merrer, Iain Moore, Alejandro Ortiz-Cortes, Benoit Osmond, Julien Piot, Olivier Pochon, Sebastian Raeder, Antoine de Roubin, Hervé Savajols, Dominik Studer, Emil Traykov, Juha Uusitalo, Christophe Vandamme, Paul van den Bergh, Piet van Duppen, Klaus Wendt, In-gas-jet laser spectroscopy with S 3 -LEB, Nucl. Instrum. Methods Phys. Res. Sect. B: Beam Interactions Mater. Atoms (ISSN: 0168583X) 539 (2023) 102–107, http://dx.doi.org/10.1016/j.nimb.2023.03.020.

[36] A. O'Hagan, T.O.M. Leonard, Bayes estimation subject to uncertainty about parameter constraints, Biometrika (ISSN: 0006-3444) 63 (1) (1976) 201–203, http://dx.doi.org/10.1093/biomet/63.1.201.

6 Appendix

References

[1] R. Broda et al. "N=40 neutron subshell closure in the ^{68}Ni nucleus". In: *Physical review letters* 74.6 (1995), pp. 868–871. DOI: 10.1103/PhysRevLett.74.868.

[2] D. J. Hartley et al. "Masses and β-Decay Spectroscopy of Neutron-Rich Odd-Odd ^{160,162}Eu Nuclei: Evidence for a Subshell Gap with Large Deformation at N=98". In: *Physical review letters* 120.18 (2018), p. 182502. DOI: 10.1103/PhysRevLett.120.182502.

[3] D. J. Hartley et al. "$\nu i_{13/2}$ structures in ^{155}Sm and ^{159}Gd : Supporting evidence of a Z=60 deformed subshell gap". In: *Physical Review C* 105.1 (2022). ISSN: 0556-2813. DOI: 10.1103/PhysRevC.105.014301.

[4] E. Minaya Ramirez et al. "Direct mapping of nuclear shell effects in the heaviest elements". In: *Science (New York, N.Y.)* 337.6099 (2012), pp. 1207–1210. DOI: 10.1126/science.1225636.

[5] Jessica Warbinek. "Probing the nuclear structure of fermium by laser spectroscopy". PhD thesis. Johannes Gutenberg-Universität Mainz, 2024. DOI: 10.25358/OPENSCIENCE-9705.

[6] S. Cwiok, P-H Heenen, and W. Nazarewicz. "Shape coexistence and triaxiality in the superheavy nuclei". In: *Nature* 433.7027 (2005), pp. 705–709. ISSN: 0028-0836. DOI: 10.1038/nature03336.

[7] R-D Herzberg et al. "Isomer spectroscopy in 254 No". In: *Physica Scripta* T125 (2006), pp. 73–77. ISSN: 0031-8949. DOI: 10.1088/0031-8949/2006/T125/016.

[8] S. G. Wahid et al. "Isomers and hindrances in No254 : A touchstone for theories of superheavy nuclei". In: *Physical Review C* 111.3 (2025). ISSN: 0556-2813. DOI: 10.1103/PhysRevC.111.034320.

[9] X. F. Yang et al. "Laser spectroscopy for the study of exotic nuclei". In: *Progress in Particle and Nuclear Physics* 129 (2023), p. 104005. ISSN: 01466410. DOI: 10.1016/j.ppnp.2022.104005.

[10] C. F. v. Weizsäcker. "Zur Theorie der Kernmassen". In: *Zeitschrift für Physik* 96.7-8 (1935), pp. 431–458. ISSN: 1434-6001. DOI: 10.1007/BF01337700.

[11] Jens–Volker Kratz. *Nuclear and Radiochemistry*. Wiley, 2021. ISBN: 9783527349050. DOI: 10.1002/9783527831944.

[12] Maria Goeppert-Mayer. "On Closed Shells in Nuclei. II". In: *Physical Review* 75.12 (1949), pp. 1969–1970. ISSN: 0031-899X. DOI: 10.1103/PhysRev.75.1969.

[13] J. H. D. Jensen and J. M. Luttinger. "Angular Momentum Distributions in the Thomas-Fermi Model". In: *Physical Review* 86.6 (1952), pp. 907–910. ISSN: 0031-899X. DOI: 10.1103/PhysRev.86.907.

[14] William D. Myers and Wladyslaw J. Swiatecki. "Nuclear masses and deformations". In: *Nuclear Physics* 81.1 (1966), pp. 1–60. ISSN: 00295582. DOI: 10.1016/0029-5582(66)90639-0.

[15] V. M. Strutinsky. "Shell effects in nuclear masses and deformation energies". In: *Nuclear Physics A* 95.2 (1967), pp. 420–442. ISSN: 03759474. DOI: 10.1016/0375-9474(67)90510-6.

[16] Peter Möller. "The limits of the nuclear chart set by fission and alpha decay". In: *EPJ Web of Conferences* 131 (2016), p. 03002. DOI: 10.1051/epjconf/201613103002.

[17] Rolf-Dietmar Herzberg. "Nuclear Structure of Superheavy Elements". In: *The Chemistry of Superheavy Elements*. Ed. by Matthias Schädel and Dawn Shaughnessy. Berlin, Heidelberg: Springer Berlin Heidelberg, 2014, pp. 83–133. ISBN: 978-3-642-37465-4. DOI: https://doi.org/10.1007/978-3-642-37466-1_2.

[18] Yu. Ts. Oganessian et al. "Synthesis of the isotopes of elements 118 and 116 in the ^{249}Cf and ^{245}Cm + ^{48}Ca fusion reactions". In: *Physical Review C* 74.4 (2006). ISSN: 0556-2813. DOI: 10.1103/PhysRevC.74.044602.

[19] Michael Block, Mustapha Laatiaoui, and Sebastian Raeder. "Recent progress in laser spectroscopy of the actinides". In: *Progress in Particle and Nuclear Physics* 116 (2021), p. 103834. ISSN: 01466410. DOI: 10.1016/j.ppnp.2020.103834.

[20] Sven Gösta Nilsson. *Binding states of individual nucleons in strongly deformed nuclei*. Tech. rep. 16. 1955. URL: https://cds.cern.ch/record/212345.

[21] Chin Fu Tsang and Sven Gösta Nilsson. "Shape isomeric states in heavy nuclei". In: *Nuclear Physics A* 140.2 (1970), pp. 275–288. ISSN: 03759474. DOI: 10.1016/0375-9474(70)90326-X.

[22] *Karlsruher Nuklidkarte*. 11. Auflage. Karlsruhe and Lage: Nucleonica GmbH and Marktdienste Haberbeck GmbH, 2022. ISBN: 978-3-00-069180-5.

[23] Wolfgang Demtröder. *Laserspektroskopie*. Berlin, Heidelberg: Springer Berlin Heidelberg, 2000. ISBN: 978-3-662-08267-6. DOI: 10.1007/978-3-662-08266-9.

[24] R. V. Ambartzumian and V. S. Letokhov. "Selective Two-Step (STS) Photoionization of Atoms and Photodissociation of Molecules by Laser Radiation". In: *Applied optics* 11.2 (1972), pp. 354–358. ISSN: 1559-128X. DOI: 10.1364/AO.11.000354.

[25] G. S. Hurst et al. "Resonance ionization spectroscopy and one-atom detection". In: *Reviews of Modern Physics* 51.4 (1979), pp. 767–819. ISSN: 0034-6861. DOI: 10.1103/RevModPhys.51.767.

[26] Wilfried Nörtershäuser and Christopher Geppert. "Nuclear Charge Radii of Light Elements and Recent Developments in Collinear Laser Spectroscopy". In: *The Euroschool on Exotic Beams, Vol. IV*. Ed. by Christoph Scheidenberger and Marek Pfützner. Vol. 879. Lecture Notes in Physics. Berlin, Heidelberg: Springer Berlin Heidelberg, 2014, pp. 233–292. ISBN: 978-3-642-45140-9. DOI: 10.1007/978-3-642-45141-6{\textunderscore}6.

[27] K. Kreim et al. "Nuclear charge radii of potassium isotopes beyond N=28". In: *Physics Letters B* 731 (2014), pp. 97–102. ISSN: 03702693. DOI: 10.1016/j.physletb.2014.02.012.

[28] C. Gorges et al. "Laser Spectroscopy of Neutron-Rich Tin Isotopes: A Discontinuity in Charge Radii across the N=82 Shell Closure". In: *Physical review letters* 122.19 (2019), p. 192502. DOI: 10.1103/PhysRevLett.122.192502.

[29] T. Day Goodacre et al. "Charge radii, moments, and masses of mercury isotopes across the N=126 shell closure". In: *Physical Review C* 104.5 (2021). ISSN: 0556-2813. DOI: 10.1103/PhysRevC.104.054322.

[30] M. Reponen et al. "Evidence of a sudden increase in the nuclear size of proton-rich silver-96". In: *Nature communications* 12.1 (2021), p. 4596. DOI: 10.1038/s41467-021-24888-x.

[31] Wolfgang Demtröder. *Laserspektroskopie 2*. Berlin, Heidelberg: Springer Berlin Heidelberg, 2013. ISBN: 978-3-642-21446-2. DOI: 10.1007/978-3-642-21447-9.

[32] P. Campbell, I. D. Moore, and M. R. Pearson. "Laser spectroscopy for nuclear structure physics". In: *Progress in Particle and Nuclear Physics* 86 (2016), pp. 127–180. ISSN: 01466410. DOI: 10.1016/j.ppnp.2015.09.003.

[33] Jim Al-Khalili and Ernst Roeckl. *The Euroschool Lectures on Physics with Exotic Beams, Vol. II*. Vol. 700. Springer Berlin Heidelberg, 2006. ISBN: 978-3-540-33786-7. DOI: 10.1007/b11743651.

[34] Wolfgang Demtröder. *Experimentalphysik 3*. Berlin, Heidelberg: Springer Berlin Heidelberg, 2016. ISBN: 978-3-662-49093-8. DOI: 10.1007/978-3-662-49094-5.

[35] Steven Nothhelfer. "Advances in laser spectroscopy of superheavy elements: Resonance ionization spectroscopy on 253,254,255Es and a new gas-jet based high-resolution spectroscopy setup". PhD thesis. Johannes Gutenberg-Universität Mainz, 2022. DOI: 10.25358/openscience-6958.

[36] Jessica Warbinek et al. "Advancing Radiation-Detected Resonance Ionization towards Heavier Elements and More Exotic Nuclides". In: *Atoms* 10.2 (2022), p. 41. DOI: 10.3390/atoms10020041.

[37] Yu. Kudryavtsev et al. "The in-gas-jet laser ion source: Resonance ionization spectroscopy of radioactive atoms in supersonic gas jets". In: *Nuclear Instruments and Methods in Physics Research Section B: Beam Interactions with Materials and Atoms* 297 (2013), pp. 7–22. ISSN: 0168583X. DOI: 10.1016/j.nimb.2012.12.008.

[38] Yu. Ts. Oganessian et al. "Measurements of cross sections for the fusion-evaporation reactions ^{204,206,207,208}Pb + ^{48}Ca and ^{207}Pb + ^{34}S: Decay properties of the even-even nuclides ^{238}Cf and ^{250}No". In: *Physical Review C* 64.5 (2001). ISSN: 0556-2813. DOI: 10.1103/PhysRevC.64.054606.

[39] G. Münzenberg et al. "The velocity filter ship, a separator of unslowed heavy ion fusion products". In: *Nuclear Instruments and Methods* 161.1 (1979), pp. 65–82. ISSN: 0029554X. DOI: 10.1016/0029-554X(79)90362-8.

[40] Michael Block et al. "Recent progress in experiments on the heaviest nuclides at SHIP". In: *La Rivista del Nuovo Cimento* 45.4 (2022), pp. 279–323. ISSN: 0393-697X. DOI: 10.1007/s40766-022-00030-5.

[41] H. Wollnik and M. Przewloka. "Time-of-flight mass spectrometers with multiply reflected ion trajectories". In: *International Journal of Mass Spectrometry and Ion Processes* 96.3 (1990), pp. 267–274. ISSN: 01681176. DOI: 10.1016/0168-1176(90)85127-N.

[42] M. Schlaich et al. "A multi-reflection time-of-flight mass spectrometer for the offline ion source of the PUMA experiment". In: *International Journal of Mass Spectrometry* 495 (2024), p. 117166. ISSN: 13873806. DOI: 10.1016/j.ijms.2023.117166.

[43] A Einstein. "Strahlungs-Emission und -Absorption nach der Quantentheorie". In: *Verhandlungen der Deutschen Physikalischen Gesellschaft* 18 (1916), p. 318. URL: https://cds.cern.ch/record/632330.

[44] R Gordon Gould et al. "The LASER, light amplification by stimulated emission of radiation". In: *The Ann Arbor conference on optical pumping, the University of Michigan*. Vol. 15. 128. 1959, p. 92.

[45] T. H. MAIMAN. "Stimulated Optical Radiation in Ruby". In: *Nature* 187.4736 (1960), pp. 493–494. ISSN: 0028-0836. DOI: 10.1038/187493a0.

[46] "XXX. On the change of refrangibility of light". In: *Philosophical Transactions of the Royal Society of London* 142 (1852), pp. 463–562. ISSN: 0261-0523. DOI: 10.1098/rstl.1852.0022.

[47] Joseph R. Lakowicz. *Principles of Fluorescence Spectroscopy*. Boston, MA: Springer US, 2006. ISBN: 978-0-387-31278-1. DOI: 10.1007/978-0-387-46312-4.

[48] Vladilen S. Letochov. *Laser photoionization spectroscopy*. Orlando, Fla.: Acad. Pr, 1987. ISBN: 0124443206.

[49] H.-J. Kluge et al. "Resonance ionization spectroscopy for trace analysis and fundamental research". In: *Fresenius' Journal of Analytical Chemistry* 350.4-5 (1994), pp. 323–329. ISSN: 0937-0633. DOI: 10.1007/bf00322490.

[50] Klaus D. A. Wendt et al. "Laser Based Techniques for Ultra Trace Isotope Production, Spectroscopy and Detection". In: *Hyperfine Interactions* 162.1-4 (2006), pp. 147–157. ISSN: 0304-3843. DOI: 10.1007/s10751-005-9219-8.

[51] S. Raeder et al. "Performance of Dye and Ti:sapphire laser systems for laser ionization and spectroscopy studies at S^3". In: *Nuclear Instruments and Methods in Physics Research Section B: Beam Interactions with Materials and Atoms* 463 (2020), pp. 86–95. ISSN: 0168583X. DOI: 10.1016/j.nimb.2019.11.024.

[52] W. Heisenberg. "Über den anschaulichen Inhalt der quantentheoretischen Kinematik und Mechanik". In: *Zeitschrift fr Physik* 43.3-4 (1927), pp. 172–198. ISSN: 1434-6001. DOI: 10.1007/BF01397280.

[53] Ludwig Boltzmann. "Studien über das Gleichgewicht der lebendigen Kraft zwischen bewegten materiellen Punkten". In: 58 (1868), pp. 517–560. DOI: 10.1017/CBO9781139381420.006.

[54] Ludwig Boltzmann. "Über die Beziehung zwischen dem zweiten Hauptsatze der Mechanischen Wärmetheorie und der Wahrscheinlichkeitsrechnung, respective den Sätzen über das Wärmegleichgewicht," in: *Wiener Berichte* 76 (1877), pp. 373–435.

[55] Christian Doppler. "Über das farbige Licht der Doppelsterne und einiger anderer Gestirne des Himmels. Versuch einer das Bradley'schen Aberrations-Theorem als integrirenden Theil in sich schliessenden allgemeineren Theorie." In: *Abhandlungen der königlichen böhmischen Gesellschaft der Wissenschaften* 5.2 (1842).

[56] Woldemar Voigt. *Über das Gesetz der Intensitätsverteilung innerhalb der Linien eines Gasspektrums*. Vol. 1912,25. Sitzungsberichte. München, 1912. URL: https://publikationen.badw.de/de/003395768.

[57] E. C. SELTZER. "K X-Ray Isotope Shifts". In: *Physical Review* 188.4 (1969), pp. 1916–1919. ISSN: 0031-899X. DOI: 10.1103/physrev.188.1916.

[58] Klaus Blaum, Jens Dilling, and Wilfried Nörtershäuser. "Precision atomic physics techniques for nuclear physics with radioactive beams". In: *Physica Scripta* T152 (2013), p. 014017. ISSN: 0031-8949. DOI: 10.1088/0031-8949/2013/T152/014017.

[59] William H. King and W. H. King. *Isotope shifts in atomic spectra*. Physics of atoms and molecules. New York: Plenum Press, 1984. ISBN: 0306415623.

[60] S. Raeder et al. "Probing Sizes and Shapes of Nobelium Isotopes by Laser Spectroscopy". In: *Physical review letters* 120.23 (2018), p. 232503. DOI: 10.1103/PhysRevLett.120.232503.

[61] Jessica Warbinek et al. "Smooth trends in fermium charge radii and the impact of shell effects". In: *Nature* 634.8036 (2024), pp. 1075–1079. ISSN: 0028-0836. DOI: 10.1038/s41586-024-08062-z.

[62] S. Nothhelfer. "Nuclear Structure Investigations on Es-253-255 by Laser Resonance Ionization Spectroscopy (RIS)". Poster done by S. Nothhelfer for internal use.

[63] Peter W. Atkins, Julio de Paula, and James J. Keeler. *Atkins' physical chemistry*. Eleventh edition. Oxford and New York: Oxford University Press, 2018. ISBN: 978-0198769866.

[64] Yu. Kudryavtsev et al. "A new in-gas-laser ionization and spectroscopy laboratory for off-line studies at KU Leuven". In: *Nuclear Instruments and Methods in Physics Research Section B: Beam Interactions with Materials and Atoms* 376 (2016), pp. 345–352. ISSN: 0168583X. DOI: 10.1016/j.nimb.2016.02.040.

[65] Jürgen H. Gross. *Mass Spectrometry*. Cham: Springer International Publishing, 2017. ISBN: 978-3-319-54397-0. DOI: 10.1007/978-3-319-54398-7.

[66] A. E. Cameron and D. F. Eggers. "An Ion "Velocitron"". In: *Review of Scientific Instruments* 19.9 (1948), pp. 605–607. ISSN: 0034-6748. DOI: 10.1063/1.1741336.

[67] Simon Maher, Fred P. M. Jjunju, and Stephen Taylor. "Colloquium : 100 years of mass spectrometry: Perspectives and future trends". In: *Reviews of Modern Physics* 87.1 (2015), pp. 113–135. ISSN: 0034-6861. DOI: 10.1103/RevModPhys.87.113.

[68] Robert Wolf. "First on-line applications of a multi-reflection time-of-flight mass separator at ISOLTRAP and the mass measurement of ^{82}Zn". en. PhD thesis. Mathematisch-Naturwissenschaftliche Fakultät, Ernst-Moritz-Arndt-Universität Greifswald, 2013.

[69] M. Rosenbusch et al. "The new MRTOF mass spectrograph following the ZeroDegree spectrometer at RIKEN's RIBF facility". In: *Nuclear Instruments and Methods in Physics Research Section A: Accelerators, Spectrometers, Detectors and Associated Equipment* 1047 (2023), p. 167824. ISSN: 01689002. DOI: 10.1016/j.nima.2022.167824.

[70] S. Hofmann. "Synthesis of superheavy elements by cold fusion". In: *Russian Chemical Reviews* 78.12 (2009), pp. 1123–1138. ISSN: 0036-021X. DOI: 10.1070/rc2009v078n12abeh004076.

[71] M. G. Itkis et al. "Fusion and fission of heavy and superheavy nuclei (experiment)". In: *Nuclear Physics A* 944 (2015), pp. 204–237. ISSN: 03759474. DOI: 10.1016/j.nuclphysa.2015.09.007.

[72] H. Backe et al. "Prospects for laser spectroscopy, ion chemistry and mobility measurements of superheavy elements in buffer-gas traps". In: *Nuclear Physics A* 944 (2015), pp. 492–517. ISSN: 03759474. DOI: 10.1016/j.nuclphysa.2015.07.002.

[73] Mustapha Laatiaoui et al. "Atom-at-a-time laser resonance ionization spectroscopy of nobelium". In: *Nature* 538.7626 (2016), pp. 495–498. ISSN: 0028-0836. DOI: 10.1038/nature19345.

[74] Willy Wien. "Untersuchungen über die electrische Entladung in verdünnten Gasen". In: *Annalen der Physik* 301.6 (1898), pp. 440–452. ISSN: 0003-3804. DOI: 10.1002/andp.18983010618.

[75] S. Hofmann and G. Münzenberg. "The discovery of the heaviest elements". In: *Reviews of Modern Physics* 72.3 (2000), pp. 733–767. ISSN: 0034-6861. DOI: 10.1103/RevModPhys.72.733.

[76] S. Raeder et al. "A gas-jet apparatus for high-resolution laser spectroscopy on the heaviest elements at SHIP". In: *Nuclear Instruments and Methods in Physics Research Section B: Beam Interactions with Materials and Atoms* 463 (2020), pp. 272–276. ISSN: 0168583X. DOI: 10.1016/j.nimb.2019.05.016.

[77] H. Backe et al. "Towards optical spectroscopy of the element nobelium ($Z = 102$) in a buffer gas cell". In: *The European Physical Journal D* 45.1 (2007), pp. 99–106. ISSN: 1434-6060. DOI: 10.1140/epjd/e2007-00198-1.

[78] F. Lautenschläger et al. "Developments for resonance ionization laser spectroscopy of the heaviest elements at SHIP". In: *Nuclear Instruments and Methods in Physics Research Section B: Beam Interactions with Materials and Atoms* 383 (2016), pp. 115–122. ISSN: 0168583X. DOI: 10.1016/j.nimb.2016.06.001.

[79] Jeremy Lantis et al. "In-gas-jet laser spectroscopy of ^{254}No with JetRIS". In: *Physical Review Research* 6.2 (2024). DOI: 10.1103/PhysRevResearch.6.023318.

[80] M. Verlinde et al. "Single-longitudinal-mode pumped pulsed-dye amplifier for high-resolution laser spectroscopy". In: *The Review of scientific instruments* 91.10 (2020), p. 103002. DOI: 10.1063/5.0017985.

[81] Christian Helmel. "Characterization of a Multi-Reflection Time-of-Flight Mass Spectrometer (MR-ToF MS)". Master Thesis. Johannes Gutenberg Universität Mainz, 2024.

[82] BALRAJ SINGH. "Nuclear Data Sheets for $A = 254$". In: *Nuclear Data Sheets* 156 (2019), pp. 1–69. ISSN: 00903752. DOI: 10.1016/j.nds.2019.02.003.

[83] BALRAJ SINGH. "Nuclear Data Sheets for $A = 130$". In: *Nuclear Data Sheets* 93.1 (2001), pp. 33–242. ISSN: 00903752. DOI: 10.1006/ndsh.2001.0012.

List of Figures

Table 1: Declaration of the use of AI tools in this work.

AI tool	Used for	Reason	When/where
ChatGPT 4.0	Rewriting of self-written and formatted tex	Improving readability	Sec. 3.3
ChatGPT 4.0	Generating a basic Python script for visualization	Visualization of nuclear shapes	Right subfigure of Fig. 4
ChatGPT 4.0	Finding links to already known, old original literature for citation	Good scientific practice	Sources [43], [46], [52], [53], [54], [55] and [56]